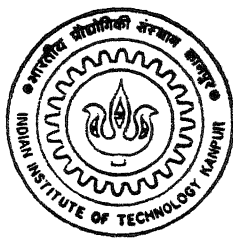


FAST ALGORITHMS FOR JOSEPHSON JUNCTION ARRAYS AND THEIR APPLICATIONS

by
SUJAY DATTA



PHY
1996
D
DAT
FAS

TH
PHY/1996/D
D262F

DEPARTMENT OF PHYSICS
INDIAN INSTITUTE OF TECHNOLOGY KANPUR
March, 1996

FAST ALGORITHMS FOR JOSEPHSON JUNCTION ARRAYS AND THEIR APPLICATIONS

A Thesis Submitted
in Partial Fulfillment of the Requirements
for the Degree of
Doctor of Philosophy

by
Sujay Datta

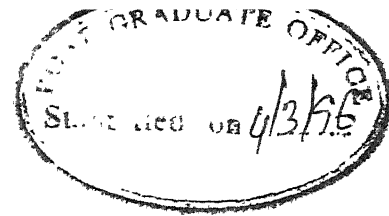
to the
DEPARTMENT OF PHYSICS
INDIAN INSTITUTE OF TECHNOLOGY KANPUR
MARCH 1996

5 AUG 1997
CENTRAL LIBRARY
I. I. T., KANPUR

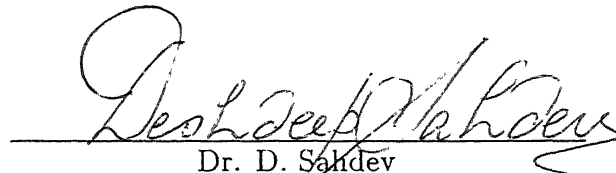
Acc. No. A 123638

To
Jolly
And
Madhusudan Datta

CERTIFICATE



It is certified that the work contained in this thesis entitled *Fast Algorithms For Josephson Junction Arrays And Their Applications* by *Sujay Datta* has been carried out under my supervision and that this work has not been submitted elsewhere for a degree.

A handwritten signature in cursive script, which appears to read "Dr. D. Sankar".

Dr. D. Sankar
Associate Professor
Department of Physics
Indian Institute of Technology
Kanpur

March 1996

Synopsis

Josephson Junction Arrays (JJAs) have been the focus of growing interest among the scientific community. This is in part due to a development in the standard submicron technology which have made the manufacture of arrays with controlled variation of the junction parameters feasible. Theoretically, they act as laboratory representatives of the much studied 2-D XY Model, which undergoes a Kosterlitz–Thouless phase transition. Recently the dynamics of such arrays have been studied both numerically and experimentally. The purpose of this thesis is to explore the dynamics of JJAs in detail.

The relevant model used to numerically simulate the dynamics of JJAs is called the Resistively and Capacitively Shunted Josephson (RCSJ) model. In this model, the total current flowing through a junction is divided into capacitive, resistive, superconducting and noise terms. Using total current conservation at each node of a $N_x \times N_y (\equiv N)$ 2D array and neglecting magnetic shielding effects, this leads to the evolution equation of the phases (θ) which, for overdamped junctions (zero capacitance), can be conveniently written in matrix notation as

$$G_0^{-1} [\dot{\theta}] = [d]$$

Here G_0^{-1} is the $N \times N$ connectivity matrix relevant to the system and $[d]$ is the divergence vector.

The thesis is divided into six chapters. In Chapter 1, we review the existing literature and place our work in its context. We develop a range of fast algorithms with realistic boundary conditions applicable to experimentally considered geometries

in Chapter 2. A general procedure consists of determining the eigenvalues and eigenfunctions of the corresponding Green's function satisfying the boundary conditions which arise out of finiteness of the array or a specific choice of the gauge (as in electrostatics). We deal with four cases and show that the complexity in the integration at each time step using RCSJ Model is reduced from $\mathcal{O}(N^2)$ to $\mathcal{O}(N \ln N)$ for an array with size $N_x \times N_y \equiv N$. Finally, we show that even with in the presence of defects, caused by bond-removal, the complexity increases marginally.

The extension of the above procedure for the case of triangular arrays is done in Chapter 3. We note the equivalence of the Josephson array with a lattice formed by sampling data at a finite number points on a 2D plane as in Digital Signal Processing. An extension of this idea reveals that triangular JJAs can possess two types of periodicity viz., hexagonal and rectangular. We, accordingly develop fast procedures for both in addition to that of the finite case.

Chapter 4 deals with our numerical studies on defects in square arrays using the fast algorithms. For a linear bond disordered defect we show that vortex pinning enhances the system's stability. A similar behaviour is observed for the case of bond diluted linear defects in a long narrow array. However, the defect size is much smaller than earlier estimates due to finite size effects which we accordingly investigate. The energy of the system in the time independent regime is conveniently divided into various sectors, with each sector being characterised by the number of pinned vortices present in the array. Kink discontinuities are seen at the edges of each sector. The pinned vortices also cause hysteresis in the array which we examine in detail. In the time dependent periodic regime, waves are seen to propel these vortices forward. An investigation into the behaviour of distributed defects reveals that streamlined defects have a higher stability as in hydrodynamics.

We examine the case of ballistic vortex motion predicted for to occur in capacitive arrays in Chapter 5. Vortices, in this case, are created from a linear defect. We show that in contrast to a single vortex, a "vortex-street" can move through a field depleted region. We account for the vortex-vortex interactions including the infinite

array of images present across the finite array and show that the depinning current of a vortex is the same as in the infinite array limit. The inclusion of this term into the phenomenological equation of motion correctly provides the displacement of a single vortex as a function of time. The vortices are seen to be massless for Stewart-McCumber parameter $\lesssim 30$. Chapter 6 contains our results and discussions.

Acknowledgments

To acknowledge the help and affection of all the people who have made the stay at IITK pleasurable would be impossible, nor would it be in any way a measure of my gratitude for them. However as a duty it is sacred.

I am rightly indebted to my guide Dr. D. Sahdev, who stood by me in the most trying of situations and guided me ever upwards. But for his sheer perseverance and kind attentions, neither me nor this thesis would be in this present state.

In the same vein, I would like to acknowledge the help extended during long periods of stay in Delhi to Dr. R. Mehrotra. Had it not been for the use the facilities at NPL and more importantly the collaboration it led to, this thesis would be far from complete. A word of thanks is due for Dr. S. R. Shenoy with whom I had the opportunity to collaborate. Amongst the faculty members of IITK, I would like to acknowledge the help of Dr. J. K. Bhattacharya, Dr. A. Singh and Dr. A. K. Mazumdar who took keen interest in the work. Dr. M. K. Verma was always there as a friend to boost up spirits when things went awry.

It would be unfair not to acknowledge the B-Top gang. They have been much more than friends – Samiran with his ebullience, Debnath with his down-to-earth attitude, Dinu whose Sunday night cookings were like the pie on the cream, Tapan with his innate sense of cracking the best joke and Shanti with his stoicness and sense of responsibility. Besides being a co-worker, Shanti has been a worthy teammate on innumerable occasions. The association of Bhabani, Prasen, Sudhansu and Prabal also proved to be of immense value.

There have been others friends too who have been special. Shreesh has always been a inspiration in more than one way. Without the Indu, Moorthy and Kapil, the stay in the capital would have been bland. Sudhir, Vinay, Maggu, Ranjan, GK, Kak, Himangshu, Swapan, Sayan, Alok, Tarak and Abir have made many an evening a memorable one while Tapan da, Boudi, Mamon and Mamphi have made the stay homely. I am rightly indebted to Nandini for being the Red Oleander.

Finally, I would like to thank my parents and brother who have with their love and patience have constantly been a source of inspiration.

S. Datta

Contents

Synopsis	iv
Acknowledgments	vii
1 Introduction	1
1.1 Properties	2
1.2 Arrays In Thermal Equilibrium	4
1.3 Imposition of Magnetic Field	7
1.4 Capacitive Arrays	9
1.5 Dynamics of Arrays	10
1.5.1 Disordered Arrays	12
1.5.2 Shapiro Steps	13
1.6 Overview Of Current Research	14
1.7 Outline Of The Thesis	15
Appendix.1.A	17
2 Fast Algorithms for Square Arrays	18
2.1 Introduction	18
2.2 The Eikmans–Himbergen algorithm	21
2.2.1 Preliminaries	21
2.2.2 The $\mathcal{O}(N \ln N)$ procedure	23
2.2.3 The Imposition of Boundaries	25

2.3	Inclusion of Bus-bars	28
2.3.1	Arrays with a Single Bus-bar	30
2.3.2	The Case of a Double Bus-bar	33
2.4	Defects	35
2.5	Summary And Discussion	37
	Appendix 2.A	39
3	Fast Algorithms For Triangular Arrays	42
3.1	Introduction	42
3.2	Notation	43
3.3	Periodic Triangular Lattice : Sampling Strategies	46
3.3.1	Fast Algorithms for Rectangularly Periodic Lattice	49
3.3.2	Fast Algorithms for Hexagonally Periodic Lattice	51
3.4	Finite Triangular Lattice	53
3.5	Summary and Discussion	60
4	Defects	63
4.1	Introduction	63
4.2	Linear Defects	65
4.2.1	Graded Defects	65
4.2.2	Broken Bonds	70
4.2.3	Energy Of the System and Hysteresis	75
4.2.4	The Periodic Regime	78
4.3	Extended Defects	81
4.4	Summary and Conclusions	85
5	Ballistic Vortices	86
5.1	System Configuration	88
5.2	Numerical Simulation	90
5.3	Vortex Vortex Interactions	92
5.4	Equation Of Motion Of Vortex	97

5.5	Discussion and Conclusion	100
6	Results and Discussions	102
6.1	Results	102
6.2	Discussion and Scope For Further Study	106

List of Tables

1.1	Overview of the important array parameters.	17
-----	---	----

List of Figures

1.1	A square lattice with the light shaded regions depicting the superconductors and the dark shaded ones the insulator. r indicates the sites while R represents the dual sites.	3
1.2	The figure shows how the phases in the left plaquette have to rotate by a finite amount so that the vortex (represented by $+$) can move to the right plaquette.	10
2.1	The general flowchart of the $\mathcal{O}(N \ln N)$ method. Given $d(x, y)$, one performs a 2-D forward transform and multiplies the resulting $d(k_x, k_y)$ with $G_0(k_x, k_y)$ before taking a 2-D inverse transform to get $\theta(x, y)$	26
2.2	An finite $L_x \times L_y$ array with current being injected at the left edge and extracted from the right edge	27
2.3	An array with a single busbar at $x_L = x_0 + L_x - 1$. The injection edge x_0 can be driven by any current profile.	29
2.4	An array with a double busbars	30
2.5	The general flowchart of the procedure described in Sec.2.3.1. Given $d_{x,y}$, one performs a 1-D forward transform to get d_{x,k_y} , calculates the higher order divergences (d_{x,k_y}^p) and uses tridiagonalisation to get $\dot{\theta}_{x,k_y}$. Finally, a 1-D inverse transform provides $\dot{\theta}_{x,y}$	34
3.1	A sampling strategy for triangular arrays producing tiles	48
3.2	A triangular lattice with $L_1 = L_2 = 3$ showing rectangular periodicity. Equivalent points on the edges are marked with same labels.	50

3.3	A triangular lattice with $L = 3$ showing hexagonal periodicity. Equivalent points on the edges are marked with same labels.	51
3.4	The flow diagram for the case of a $L = 2$ hexagonal FFT. One of the 3-point “butterflies” in (a) is shown explicitly in (b).	54
3.5	A triangular array with $L_1 = L_2 = 3$ which is finite in the \hat{e}_1 direction.	55
4.1	Schematic figure of $y > 0$ portion of a 4×16 array with a $n = 4$ defect (shown by a shaded region). Black dots and thick lines joining them symbolize superconducting islands and Josephson junctions, respectively. Narrow lines inside the defect denote graded or broken bonds. Arrows marked i symbolize a current i_{ext} in the direction of the arrow.	66
4.2	A plot of i_c and i_v vs. g showing the minimum in i_c for 64×64 array with a linear defect consisting of 20 graded bonds.	67
4.3	Typical configuration of phases in the central corridor of a 32×128 array with a $n = 50, g = 0.1$ graded defect. Only a portion of the corridor is shown. The shaded region is the defect. The vortices are marked with a + sign. For (a) $i_{ext} < i_v$ while for (b) and (c) $i_v < i_{ext} < i_c$. The number of pinned vortices in (a),(b) and (c) are 0, 1 and 2 respectively.	69
4.4	A log-log plot of $(\Delta i_c / i_c^\infty)$ vs. (N_x / n) for various n but constant $N_y / n = 32$ showing the scaling behavior.	72
4.5	A plot of critical currents i_v (\bullet) and i_c (\times) vs. n for a 16×256 array. For $n \simeq 74, i_c = i_v$. Also shown are i_c^∞ values (\circ) using corrections for finite N_x from Fig. 3. The inset shows a magnified region where i_v and i_c bifurcate.	74
4.6	The energy of 16×256 array with $n = 100$ the system as a function of $i_{ext} < i_c$. Discontinuities appear at each transition from one vortex sector to the next. The inset shows a magnified transition region. . . .	76
4.7	The hysteresis loop for a 8×256 array with $n = 50$ for $i_{ext} < i_c$. In this figure the y scale represents energy/bond.	77

4.8	A snapshot of an 32×128 with $n = 9$ array in the periodic regime. The arrows represent the phases at the superconducting sites. The defect is the lightly shaded region. The dark shaded plaquettes are occupied by vortices. The wavefronts corresponding to the spin waves are seen as dark streaks across the picture and form a wake in front of the vortices. Note that the wake is asymmetric about the y -axis.	79
4.9	The critical current i_c vs. the separation d between defects.	82
4.10	Schematic figure of the $y > 0$ section an array with a typical defect (shaded) labeled $2, 3 - 1, 3, 3 - 1, 2$ used to study streamlining. Each side of dotted squares denotes a Josephson junction. Current is injected/withdrawn from left/right edge. All the junctions inside the shaded region are graded with $g = 10^{-7}$ and are equivalent to broken bonds.	83
4.11	The variation of i_c with m used to study streamlining. The circles represent i_c values for defects $2, m - 0, 3, m - 0, 2$ while crosses are for defect pattern $2, m - 1, 3, , m - 1, 2$. The i_c for single $n = 3$ defect is shown by a bold line while the dotted line is for a $15 - 1, 3, 15 - 1$ defect.	84
5.1	A schematic of a 4×8 array with a $n = 2$ defect. Black dots and lines joining them symbolize superconducting islands and Josephson junctions, respectively. Arrows marked i symbolize a current i_{ext} in the direction of the arrow.	89
5.2	A plot of average voltages in various regions of the array versus current i_{ext} applied in the accelerator region.	91
5.3	The images of the charge at O in the x direction and the test charge P	93
5.4	The figure shows the positions of the image charges in the y -direction due to a $-ve$ charge placed at y_1 . The positions as measured from the origin (O), the sequence for naming the charges and their signs are given on the right. Note that each image charge in actuality corresponds to a series of charges in the x direction with the same y coordinate.	95

5.5	The threshold current required to depin a vortex plotted as a function of the force due to VVI on the vortex. The solid line is a linear least square fit to all the measured points using Eq. (5.5) with $i_p = 0.106$.	97
5.6	A plot of the position of vortex versus time. The origin of time is arbitrary. The frequency $\omega = \omega_c$ for $\beta_c = 0$ and $\omega = \omega_p$ for $\beta_c > 0$. The solid lines are fits obtained from integrating the equation of motion given by Eq. (5.6) with $i_{ext} = 0$ and $i_p = 0.106$ with and without the mass term. The β_c values are marked next to each of the fitted curves and the suffix m denotes inclusion of the mass term.	99

Chapter 1

Introduction

Superconductivity has assumed an important role in today's technical world with its usage in the manufacture of scientific devices like superconducting magnets and wires, SQUIDS, etc. In this regard, granular superconductors, in which micrometer sized superconducting grains are placed in a non-superconducting host, hold special importance. Apart from their natural occurrence in the manufacture of bulk superconductors, they are now routinely fabricated in various laboratories using highly sophisticated submicron technology. Their two-dimensional counterparts consist of a network of Josephson links connecting nearest neighbour superconducting grains[1]. Its industrial applications apart, the study of such systems is important from both theoretical and experimental viewpoints. Recent interest in the study of such arrays owes much to the development of standard submicron technology which permits one to fabricate such arrays with relative ease as well as vary their parameters over a wide range of values in a controlled manner. Moreover, these systems are experimental realisations of theoretically well-studied models and provide much insight into the behaviour of conventional and granular high- T_c superconductors.

1.1 Properties

Since a Josephson link consists of superconductors grown on a host material, they are classified into three categories in accordance with the material used as the host. These are :

SIS: Here an insulating material (e.g. Si) is used as a host while the superconductors are made of Nb.

SNS: The superconducting islands (e.g. Pb) are placed on a host which is a normal metal (e.g. Cu).

WL: A weak link consists of a narrow superconducting bridge between two superconducting nodes.

The above classification holds for Josephson Junction Arrays (hereafter referred to as JJAs) too, since they are created from Josephson links. All the categories of arrays listed above are operated well below the BCS temperature of the superconducting islands. The properties of the SNS and the SIS type JJAs are very similar and these are what we would be mostly discussing here.

The procedure used for fabricating such arrays[2] consists of creating a stencil or mask using photo or electron beam lithography and the subsequent etching of the photoresist material. The required material, e. g. the superconductor or the insulator, is next deposited through this mask by evaporation followed by a “lift off” of the stencil layer. Various experimental facilities have used different combinations of materials to achieve the desired properties of arrays and we list some of the basic properties in Table. 1.1. Usually square arrays are manufactured. Recently, however, the Delft Technical University, Netherlands[3] and others[4] have manufactured triangular arrays. Other exotic types of geometries e. g. Penrose tiling schemes, Amman lattices and Strepenki gasket lattices have also been designed and studied[5]. To describe the system at hand, we label each superconducting site (also called a node) by \vec{r} , a two dimensional vector (see Fig. 1.1). Noting that \vec{r} can take on discrete values as specified

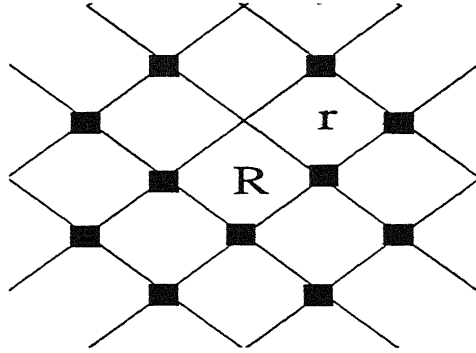


Figure 1.1: A square lattice with the light shaded regions depicting the superconductors and the dark shaded ones the insulator. r indicates the sites while R represents the dual sites.

by the lattice, we also interchangeably use the scalar index i to describe the node, since there exists a definite relationship between the two indices, specified by the underlying lattice structure.

The essential macroscopic physics of such arrays is captured if one considers that, at temperatures below the BCS temperature, the wavefunction of the condensed Cooper-pairs at the superconducting sites, $\Psi(\vec{r}, t)$, to be of the form

$$\Psi(\vec{r}, t) = |\Psi| \exp i\theta(\vec{r}, t) \quad (1.1)$$

This is a oversimplification as it ignores the variation of $|\Psi|$ with t . Moreover, it inherently implies that the phase $\theta(\vec{r}, t)$ is the same over the *entire* superconducting island. However, as shown by Eikmans[6] the phase variation over a typical island (denoted by R_0 in Table. 1.1) is $\sim 10^{-4}$. Under these approximations, the whole array is described by a single parameter set $\{\theta(\vec{r}, t)\}$.

Having laid down the basic tools for describing the system under consideration, we note that the study of such arrays can be broadly classified into two streams. The first stream consists of studying the thermodynamic properties of arrays in statistical equilibrium i.e. the static properties, while the other aims at investigating the behaviour

of JJAs far from equilibrium i.e. the dynamical properties. We discuss both directions briefly. A comprehensive account, including a microscopic treatment of such arrays is present in books of superconductivity[7, 8] and standard text books on JJAs[9].

The Hamiltonian governing the statics of such arrays is:

$$\mathcal{H} = J_0 \sum_{\langle \vec{r}\vec{r}' \rangle} \cos(\theta(\vec{r}, t) - \theta(\vec{r}', t)) \quad (1.2)$$

where $\langle \vec{r}, \vec{r}' \rangle$ represents the nearest neighbours of \vec{r} and $J_0 = (\hbar i_0)/(2e)$. Here i_0 is the single junction critical current.

One assumes that $i_0 \ll i_{c0}$ where i_{c0} is the critical current for which superconductivity is destroyed within the islands. This holds in the weak coupling limit for arrays, which in turn means that the thickness of the barrier between the superconducting sites is $\sim 1^\circ A$. To keep the nodes from becoming normal, the arrays are operated well below the BCS temperature.

Perhaps the most fundamental relation, in the context of JJAs, is that between the voltage (ΔV) developed across a junction due to the existence of a phase difference ($\Delta\theta$) at the the two superconducting sites of a junction. This is called the Josephson relation[1] and is given by

$$\Delta V = \frac{\hbar}{2e} \frac{d\Delta\theta}{dt} \quad (1.3)$$

The relationship has found an important application in the setting up of voltage standards since it involves fundamental constants.

1.2 Arrays In Thermal Equilibrium

Knowing the Hamiltonian (Eq.[1.2]), the thermodynamic properties of the system can be calculated from the canonical partition function \mathcal{Z}

$$\mathcal{Z} = \int_{-\pi}^{\pi} D(\theta) \exp\left(-\frac{\mathcal{H}}{k_B T}\right) \quad (1.4)$$

where the $D(\theta)$ represents integration over all the field variables $\{\theta(\vec{r})\}$ and k_B is the Boltzmann factor.

Using generalised theorems[10–12], forbidding any long range order (LRO) for dimensions $D \leq D_c = 2$, it was predicted that JJAs (as well as helium and super-fluid films) cannot undergo any phase transitions. The theorems suggest that for $D < D_c$, the fluctuations in the system destroy LRO. The absence of LRO rules out the possibility of an ordered phase. This is, however, not the case. Berezenskii[13] and Kosterlitz and Thouless[14, 15](BKT) showed that in such continuous-symmetry systems a transition of the “topological excitations” or vortices can occur: At low temperature the vortices and anti-vortices present in the system are bound together to form dipole pairs which dissociate at high temperatures. To understand the new physics involved, we digress for a moment to discuss the new concept of vortices.

Physically, a vortex signifies a region of circulation of the concerned field variables. In hydrodynamics the vorticity $\vec{\omega}$ is related to the velocity fields \vec{u} as $\vec{\omega} = \nabla \times \vec{u}$. However, in the case of JJAs, there exists a quantisation condition describing a vortex. Mathematically, as a result, vortices are defined by a constraint in the phase differences of the field variables, $\theta_i - \theta_j$. Any path enclosing the center of a vortex is constrained by

$$\oint \theta_i - \theta_j = \pm 2\pi m \text{ where } m \text{ is an integer} \quad (1.5)$$

where the phase differences $\theta_i - \theta_j$ have range $-\pi < \theta_i - \theta_j \leq \pi$. Since the constraint is over *any* path, the vortices are seen to be extended objects. A similar condition is used to describe a vortex in helium films where the phase angles $S(\vec{r}) = \exp i\theta(\vec{r})$ are quantised as $\oint \nabla \theta \cdot d\vec{l} = 2m\pi$.

By mapping the hamiltonian for JJAs onto the 2-D XY model[16] one can extract the critical properties of the arrays. Many authors have performed detailed calculations in this regard[17–21] and we present a brief overview of the procedures followed.

Using the dual-transformation approach[19, 20], one can factor \mathcal{Z} as

$$\mathcal{Z} = \mathcal{Z}^{SW} \mathcal{Z}^{CG} \quad (1.6)$$

where \mathcal{Z}^{SW} is the spin-wave part and \mathcal{Z}^{CG} the Coloumb gas part of the partition function. The spin-wave part is irrelevant to the study of critical behaviour while

$$\mathcal{Z}^{CG} = \sum_{m(\vec{r})} \exp \left[\pi K_0 \sum_{\vec{r} \neq \vec{r}'} m(\vec{r}) m(\vec{r}') \ln \frac{|\vec{r} - \vec{r}'|}{a_0} \right] y_0^{\frac{\pi K_0}{2} \sum_{\vec{r}} m^2(\vec{r})} \quad (1.7)$$

where $\pi K_0 = \pi J_0 / (k_B T)$, a_0 is the lattice constant of the array and y_0 , the bare fugacity of the system, is given by

$$y_0 = \exp(-\pi^2 K_0 / 2) \quad (1.8)$$

In arriving at Eq.(1.7) one uses the neutrality condition

$$\sum_{\vec{r}} m(\vec{r}) = 0 \quad (1.9)$$

which arises from the $U(1)$ symmetry $\theta_i \rightarrow \theta_i + \alpha(t)$ of \mathcal{H} (Eq.[1.2]).

Using a renormalisation technique[14] one can then derive the renormalised couplings (K_l) and fugacities (y_l) at an arbitrary length scale l in the form of differential equations (there is a third differential equation for the free energy of the system). The linearisation of these differential equations provides the renormalisation flows and the transition temperature (T_{BKT}). It can be shown using this procedure that the scaled dielectric constant K_∞ / K_0 attains a universal value of $2/\pi$ at T_{BKT} before dropping to zero and that the phase correlation has a power law behaviour, $\langle \theta(0) \theta(\vec{r}) \rangle \sim r^\eta$ where $\eta(T_{BKT}) = 1/4$.

Experimentally, Sanchez *etal.*[22] observed a square root dependence of temperature of the dc sheet resistance indicative of a BKT transition. Since then many workers[23–30] have seen signatures of the BKT transition in such arrays in the presence/absence of an external magnetic field. Another method to observe the transition is based on the fact that vortex–antivortex pairs experience a Lorentz force in opposite directions in the presence of an external current drive. This causes the pairs to dissociate and flow at right angles to the current. This in turn results in a voltage drop V across the array which is found to be related to the input current I by

$$V \sim I^{a(T)} \quad a(T) = 1 + \pi K_\infty(T) \quad (1.10)$$

Since K_∞ has a universal drop at T_{BKT} , $a(T_{BKT}^-) = 3$ and $a(T_{BKT}^+) = 1$ [31]. Both experimental studies[32] and Monte–Carlo (MC) simulations[30] based on dynamic theories[33] have confirmed the above universal behaviour.

1.3 Imposition of Magnetic Field

When an external magnetic field is applied to a JJA, the line integral $A(\vec{r}, \vec{r}')$ of the vector potential \vec{A} enters the hamiltonian through the minimal coupling prescription $\{\theta(\vec{r}) - \theta(\vec{r}')\} \rightarrow \{\theta(\vec{r}) - \theta(\vec{r}') - A(\vec{r}, \vec{r}')\}$ and

$$\mathcal{H} = J_0 \sum_{\langle \vec{r} \vec{r}' \rangle} \cos\{\theta(\vec{r}, t) - \theta(\vec{r}', t) - A(\vec{r}, \vec{r}')\} \quad (1.11)$$

where $A(\vec{r}, \vec{r}') = \frac{1}{\phi_0} \int_{\vec{r}}^{\vec{r}'} \vec{A} \cdot d\vec{l}$. Here, $\phi_0 = (\hbar c)/(2e)$ is the elementary flux quantum. The magnetic field penetration depth of the superconducting islands is assumed to be much smaller than the size of the islands, which are thus viewed as completely expelling the magnetic field. Moreover, the flux piercing the experimentally prepared junctions is taken to be much smaller than ϕ_0 . This ensures that the magnetic shielding effects, arising from the variation of the phase around the superconductor–insulator contact plane, become negligible. These effects lead to a suppression in i_0 . The vorticity condition in the presence of magnetic fields is

$$\sum (\theta_i - \theta_j - A_{ij}) = 2\pi f \quad (1.12)$$

where f is the flux per plaquette in units of ϕ_0 . In both Monte Carlo (MC) and dynamical simulations of JJAs in the presence of a perpendicular magnetic field, the vector potential is incorporated into the governing equations using the Landau gauge condition

$$A_{ij} = \begin{cases} 2\pi f & \text{for horizontal bonds} \\ 0 & \text{for vertical bonds} \end{cases} \quad (1.13)$$

Following an approach similar to the one outlined above (Sec. 1.2) one can write down \mathcal{Z} as in Eq.[1.7] by replacing $m(\vec{r}) \rightarrow \Omega(\vec{r}) + f$ where $\Omega(\vec{r})$ are integers and f is the static contribution by the magnetic field. The neutrality condition also reads

$$\sum_{\vec{r}} \Omega(\vec{r}) + f = 0 \quad (1.14)$$

Moreover, since \mathcal{Z} has the symmetries

$$f \rightarrow f + n \quad n \in I \quad \text{and} \quad f \rightarrow -f$$

the only relevant range of f is $[0, 1/2]$. In fact, the symmetry of f over integral values is often used to test the quality of the experimentally prepared films[34].

The fact that magnetic fields induce frustration[35, 36] in an array is most easily seen for the case of $f = 1/2$. Here alternate horizontal bonds have $A_{ij} = \pi$ (and $\mathcal{H} = -J_0 \cos \theta_i - \theta_j$) while the rest have $A_{ij} = 0$ (and $\mathcal{H} = J_0 \cos \theta_i - \theta_j$). Thus each plaquette has three anti-ferromagnetic and one ferromagnetic bond causing circumstance frustration. The case of $f = 1/2$ is called the fully frustrated case. The ground state configuration for such an array, even for $T = 0$, is much more complex since field-induced vortices are created to satisfy the neutrality condition (Eq.(1.14)). Teitel and Jayaprakash[37], in their pioneering work, showed that for $f = p/q$ (p and q are integers and coprime) the ground state is a $q \times q$ periodic structure of the vortices. The upper bound of the critical current passing through the junction was estimated to be

$$i_c \left(f = \frac{p}{q} \right) \leq \frac{e\pi}{\hbar} q^{-1} \quad (1.15)$$

This implies that for $T = 0$, $i_c \rightarrow 0$ independent of the size of the system. Halsey[38] considered the “staircase” state of such a $q \times q$ lattice and showed that $i_c(f = p/q) = i_c(f = 0)q^{-1}$ independent of p . The “staircase” state is, however, not the general ground state as revealed by Monte Carlo studies conducted by Teitel[39]. For irrational p/q , it has been predicted that the ground state configuration is that of a superconducting glass[40–42].

The particular case of full frustration where $f = 1/2$ has received a great deal of attention as a realisation of Villian’s “odd-model”[35]. Although the relevant theory[43–47] and experiments[16, 26, 29, 48] are still far from complete in this area. The ground-state configuration, in this case, consists of “chequerboard” pattern of $\pm 1/2$ vortices. The existence of an unnatural phase transition – a mix of the BKT and the Ising phases, as also the universality class of such a transition have been points of considerable debate.

1.4 Capacitive Arrays

Arrays (especially SIS arrays) can have appreciable junction capacitance C_J as well as junction to ground capacitance C_G . The corresponding charging energies for Cooper pair transfer are $E_{CG} = (2e^2)/C_G$ and $E_{CJ} = (2e^2)/C_J$ respectively. Such capacitances tend to destroy phase coherence in the ordered phase. In fact for $E_{CG} \gg E_J$, the junction coupling strength, quantum fluctuations are expected to predominate. Theoretically, the treatment of capacitive arrays follows the route of writing down an effective action[49]

$$\frac{S}{\hbar} = \int_0^{\beta\hbar} \frac{d\tau}{\hbar} \left[-E_J \sum_{\langle ij \rangle} \cos \theta_i - \theta_j + \frac{m}{2} \sum_{(i)} \dot{\theta}_i^2(\tau) + \frac{M}{2} \sum_{\langle ij \rangle} \dot{\theta}_{ij}^2(\tau) \right] \quad (1.16)$$

where $\beta = 1/(k_B T)$, $m = \hbar^2/(2e^2)C_G$, $M = \hbar^2/(2e^2)C_J$ and τ is discretised in units of τ_0 . One then has an $N \times N \times N_\tau$ lattice with $N_\tau = \beta\hbar/\tau_0$. Thus capacitive arrays in d dimensions are effectively treated by a $d + 1$ dimensional field theory. As noted by Anderson and Abeles[50] such arrays can have a Mott-like insulating phase at $T = 0$. Inclusion of perturbative effects is seen to bring down T_{BKT} [51]. In fact, such arrays are seen to undergo a novel first order Quantum Induced Transition for temperatures well below T_{BKT} [52].

The dynamics of vortices in such arrays has been the focus of much recent interest. It has been speculated by Eckern[53, 54] and Korshunov[55] and that vortices in such arrays have a finite mass and under certain conditions can move ballistically in a field depleted region. Van der Zant *et al.*[3] claim to have seen ballistic motion in triangular capacitive arrays. Numerical simulation[56], however, does not show any such motion. Although various reasons have been provided to account for the discrepancy by Geigenmuller *et al.*[57], Yu *et al.*[58, 59] and Fazio *et al.*[60] the reason for the discrepancy is still unclear.

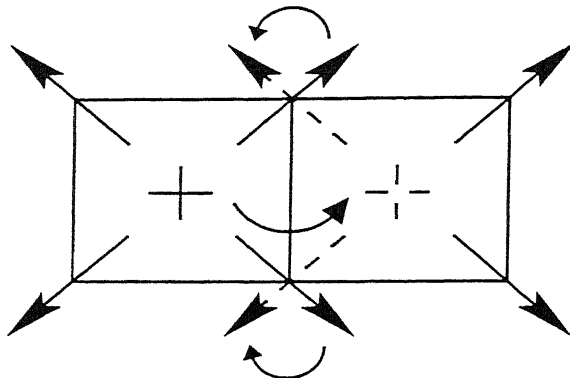


Figure 1.2: The figure shows how the phases in the left plaquette have to rotate by a finite amount so that the vortex (represented by +) can move to the right plaquette.

1.5 Dynamics of Arrays

As we have seen previously, an application of external currents introduces the concept of phase slippage and a voltage drop in the array (Eq.(1.10)). Thus the motion of a vortex present in such an array, causes dissipation. However, in contrast to continuum superconductors, where an infinitesimal external current causes motion of the vortex, JJAs provide a pinning potential which restricts such motion. This is due to the inherent discrete nature of the arrays. The vortex present at the center of a plaquette is in a low-energy site, and has to overcome a finite potential barrier to move to another plaquette (another low-energy site). To see this more clearly, we note that the motion of a vortex from a plaquette to the next must cause a *finite* rotation of the phases which translates to a definite energy barrier (see Fig. 1.2) opposing such motion. Using a pure sinusoidal potential for the pinning, Lobb *et al.*[61] have shown that vortices in an infinite array can move only if the external current scaled by the single junction critical current is ~ 0.1 .

To study the dynamics of JJAs, we take recourse to the well known Resistively and Capacitively Shunted Junction (RCSJ) Model[62]. More refined models exist[9]

to solve the single junction dynamics but the RCSJ model is, for most purposes, completely adequate. According to this model, the total current $i(\vec{r}, \vec{r}', t)$ between the superconducting island \vec{r} and \vec{r}' in general can be divided into four “channels” as

$$i(\vec{r}, \vec{r}', t) = i_S(\vec{r}, \vec{r}', t) + i_R(\vec{r}, \vec{r}', t) + i_C(\vec{r}, \vec{r}', t) + i_F(\vec{r}, \vec{r}', t) \quad (1.17)$$

All the currents are scaled in units of i_0 . The superconducting component, $i_S(\vec{r}, \vec{r}', t)$ is related to the phases $\theta(\vec{r}, t)$ by the relation

$$i_S(\vec{r}, \vec{r}', t) = \sin[\theta(\vec{r}) - \theta(\vec{r}') - A(\vec{r}, \vec{r}')] \quad (1.18)$$

and is due to the tunneling of Cooper pairs across the junction. In the RCSJ model, we consider a linear relationship between the voltage developed due to the current flowing through the junction i.e. we shunt the junction by a ohmic normal-state resistance R_n . This linear approximation adequately describes the dynamics even though the shunt resistance at the operating temperatures ($< T_{BCS}$) is not equal to R_n . In Eq.(1.17), i_C represents the current due to a finite inter-junction capacitance, C . Thus

$$i_R(\vec{r}, \vec{r}', t) = \frac{V}{i_0 R_n} = \frac{\hbar}{2ei_0 R_n} (\dot{\theta}(\vec{r}) - \dot{\theta}(\vec{r}')) \text{ and} \quad (1.19)$$

$$i_C(\vec{r}, \vec{r}', t) = \frac{C}{i_0} \dot{V}(\vec{r}, \vec{r}', t) = \frac{\hbar C}{2ei_0 R_n} (\ddot{\theta}(\vec{r}) - \ddot{\theta}(\vec{r}')) \quad (1.20)$$

Finally, there is the fluctuation current $i_F(\vec{r}, \vec{r}', t)$ which we take to be due to a white noise source, with no spatial correlations, i. e. between the noise in different junctions

$$\langle i_F(\vec{r}, \vec{r}', t) i_F(\vec{r}_1, \vec{r}'_1, t') \rangle = \frac{2}{\beta \omega_c} \delta(t - t') [\delta(\vec{r} - \vec{r}_1) \delta(\vec{r}' - \vec{r}'_1) - \delta(\vec{r} - \vec{r}'_1) \delta(\vec{r}' - \vec{r}_1)] \quad (1.21)$$

Here $\omega_c = (2ei_0 R_n)/\hbar$ and β inversely proportional to the temperature. Since the temperature enters through $\beta = J(T)/(k_B T) \equiv \hbar i_0(T)/(2ek_B T)$, Eq.(1.21) is used in dynamical simulations of arrays at finite temperatures.

The time evolution of the phase difference $\Delta\theta = \theta(\vec{r}) - \theta(\vec{r}')$ across a single junction is thus governed by the equation:

$$\beta_c \Delta \ddot{\theta}(\vec{r}) + \Delta \dot{\theta}(\vec{r}) + \sin(\Delta \theta(\vec{r}) - 2\pi A(\vec{r}, \vec{r}')) + i_F(\vec{r}, \vec{r}', t) = i(\vec{r}, \vec{r}') \quad (1.22)$$

Here we measure time in units of $1/\omega_c$. The Stewart-McCumber characteristic parameter [63, 64], β_c is defined in terms of the frequency, ω_c , of a single junction:

$$\beta_c = \left(\frac{\omega_c}{w_p} \right)^2 \quad (1.23)$$

and the plasma frequency

$$w_p = \sqrt{\frac{2eI_c}{\hbar C}} \quad (1.24)$$

In practice the characteristic frequency is of the order of 10^{10} Hz . One easily finds that β_c is the typical charging energy of the junction, $C(I_c R_n)^2$, divided by the typical coupling energy, J . For the SIS arrays, β_c can be varied continuously between $\beta_c \ll 1$ (overdamped junctions) and $\beta_c \gg 1$ (underdamped junctions). The SNS arrays are always strongly overdamped.

In arrays, these single-junction equations are coupled through the condition of current conservation at each superconducting node of the array. The resulting Total Current Conserving (TCC) dynamics [33] leads to a set of N , first-order, coupled, non-linear differential equations for the case of an array with $N_x \times N_y \equiv N$ overdamped josephson junctions. We shall in Chap. 2 show how such a set of equations can be written such that they are amenable to theoretical analysis and simulations.

Both experiments and numerical simulations have in tandem probed various parameters of the array in detail. Both overdamped ($\beta_c = 0$) and underdamped (finite β_c) current driven arrays have been studied at zero and finite temperatures in the presence/absence of magnetic fields. We briefly discuss some directions in which investigations have proceeded below.

1.5.1 Disordered Arrays

Disorder is introduced in JJAs [65] in the form of

- Bond disorder, where the Josephson coupling $J \rightarrow J_{ij}$ with J_{ij} following a specified distribution (usually Gaussian),
- Bond dilution, wherein bonds are removed either randomly or systematically to form a defect and
- Positional disorder, wherein the magnetic vector potential A_{ij} is a random or Gaussian variable.

Bond disorder has been used to distinguish between a BKT and Ising like transitions[66, 67] for $f = 1/2$, to observe a lowering in the resistivity due to pinning[68, 69], to facilitate the movement of vortices[3] and to simulate spin glass like phases in 3D arrays[70]. Positionally disordered arrays, have been studied[65, 71, 72] to look for a predicted[73] reentrant glass like phase. A novel vortex pattern[74] and a plastic-like flow of vortices are seen in such arrays. Disorder in randomly diluted arrays have been seen to preserve the scale invariance of the BKT transition[75]. The breakdown of a current driven array in the presence of a bond diluted linear defect is seen to occur when a vortex path spans the entire sample[76, 77]. The system becomes chaotic as the “vortex-street” spreads to various columns. Chaos also occurs due to a mixing of positive and negative vortices[78, 79] in an array driven by a linear current profile and in capacitive arrays in the presence of electro-magnetic radiation[80].

1.5.2 Shapiro Steps

The I-V characteristics of a single junction driven by external sinusoidal current $I = I_{rf} \sin 2\pi\nu t$ contains the the well known steps first observed by Shapiro[81]. These result from the fact that the voltage across the junction is mode locked at well known values given by $V_n = \frac{n h \nu}{2e}$. Ch. Leeman *et al.*[48] and T. D. Clark[82] experimentally observed that for a $N \times N$ array these steps were amplified by a factor of N and that the average voltage of the n^{th} step is

$$\langle V \rangle_n = \frac{n N h \nu}{2e} \quad n = 0, 1, 2 \dots \quad N = 1000 \quad (1.25)$$

Under the application of an external magnetic field characterised by $f = p/q$ (p and q are integers and coprime), fractional Shapiro steps were observed by Benz *et al.*[83] for

$$\langle V \rangle_n = \frac{nNh\nu}{2qe} \quad (1.26)$$

These authors explained the steps in terms of a motion of the vortex lattice as a whole, by an integral multiple of the lattice constant a . Numerical simulations[84] for $f = 1/q$ revealed additional steps at $\langle V \rangle_n = \frac{nN/2h\nu}{2qe}$. It was theoretically shown that the extra shapiro steps would occur if certain rows of the vortex lattice, as opposed to the lattice as a whole, moved by qa .

1.6 Overview Of Current Research

Josephson Junction Arrays are “toy universes” which exhibit a broad range of interesting phenomena[85–87]. As a result, the study of such arrays has developed along various lines. We provide a brief overview of the related topics below.

Since JJAs provide laboratory models to verify and test the predictions of the 2D XY Model much effort has been devoted to observing the critical behaviour of such arrays. These experiments have thus helped to verify and extend the theoretical underpinnings of the field. A considerable part of the research has been devoted to understanding the case of full frustration[37, 44, 45, 47, 88–97]. Disordered samples have also been studied in the presence of external magnetic fields since they are believed to be similar to spin-glasses[40, 42, 41, 46]. Generalisations of this model have also been attempted[96, 98–100]. Theoretical predictions[73] of reentrant behaviour have yet to be substantiated unambiguously[65, 71, 72].

The controlled fabrication of arrays have furthered investigations of their dynamical properties[30, 68, 76, 78, 101–106]. These have resulted among other things, in the observance of flux-flow behaviour, vortex pinning[77, 104, 106] and more complicated vortex dynamics. All of these have direct implications on the superconducting properties of granular superconductors. As is the case of statics, the dynamics of these

“collective vortex-variables” have been correlated with breakdown phenomenon and with the advent of chaotic behaviour in JJAs[79, 80, 107]. It has been shown that for disordered samples there exists a novel pattern in which the vortices arrange themselves at 27° angle to the current direction far from equilibrium[74, 108]. Moreover, a plastic-like flow of vortices is seen to occur in such highly disordered samples[109, 110].

The discovery of the Josephson effect has triggered a large effort at using such junctions as generators for microwave signals[9] with the tunable frequency related to the input dc drive current. However, the low power supplied by such junctions makes it inappropriate for industrial applications. Coupled arrays of such junctions capable of producing a coherent radiation was an alternative to overcome such a limitation. These required the existence of in-phase solutions primarily studied in 1-D arrays[111, 112]. So far, no coherence has been observed in 2-D *dc-driven* arrays[113, 114] in contrast to rf-driven arrays[115, 83].

A regime in which the charging energies of the junctions (especially in SIS arrays) is comparable in magnitude to the Josephson coupling has opened up a wealth of new and interesting concepts and observations[116, 117, 114, 118]. Recent experiments have accordingly probed superconductor-insulator transition[118] previously predicted and observed in granular superconductors. Ahranov Casher[119] and Bohm[120] effects have also been seen in JJAs.

1.7 Outline Of The Thesis

Here we present an outline of this thesis.

We shall be mostly concerned with the dynamics of arrays in the presence of current drives and defects in this thesis. Our approach will be to combine the theoretical analysis and numerical investigations to develop the machinery of integrating the coupled RSJ equations in Chap. 2. The machinery includes a range of fast integration algorithms which take into account realistic boundary conditions[121]. In Sec. 2.2 we

present a simple derivation of the Eikmans–Himbergen Algorithm[122] using the technique of Green’s function and cast the RSJ equations into the familiar language of electrostatics. We also clarify the roles played by gauge invariance and boundaries in the context of JJAs. These techniques are generalised to deal with the cases of single and double busbars in Sec. 2.3. Finally, in Sec. 2.4 we extend the scope of the fast procedures to that of a single broken bond and more generally to arrays with linear defects.

We extend the ideas developed in Chap. 2 to design fast algorithms for triangular arrays[123] in Chap. 3. In Sec. 3.2 we show how the Dirac bra-ket algebra can be used to describe the JJA. In developing the algorithm we explicitly demonstrate the relevance of ideas used in digital signal processing to the systems at hand (Sec. 3.3). We show that such arrays admit two types of periodicity and develop fast computational schemes for both. Finally, in Sec. 3.4, we extend the scope of the computational procedures to a finite triangular array.

In Chap. 4, we study the effect of bond disordered/diluted JJAs[124, 125]. The case of a linear defect is dealt with in Sec. 4.2. It is seen that for the case of a bond disordered linear defect, vortex pinning enhances the stability of the system against breakdown from superconducting to resistive flow. In the bond diluted linear defect case, we observe pinning by the perfect lattice for defect sizes much smaller than earlier predicted. A study of the finite-size effects shows scaling behaviour. The energy of the array in the presence of pinned vortices is seen to undergo discontinuous jumps and to display hysteretic behaviour, which we investigate in detail in Sec. 4.2.3. The periodic regime of such arrays is shown to consist of waves which propel the vortices forward. These are traced in Sec. 4.2.4. Sec. 4.3 deals with the idea of streamlining a defect to enhance its stability of the flow as for hydrodynamics. We show that even with increased bond dilution one can defer the onset of the resistive transition.

Motivated by the discrepancy reported in the literature between numerical observations, in Chap. 5, we take up the study of ballistic vortex motion in JJAs[126]. Sec. 5.1 presents a configuration in which vortices are created by defects rather than magnetic

fields. We show in Sec. 5.2 that although a single vortex does not move in a field depleted region, a “vortex-street” does so even in overdamped arrays. This is primarily because the vortices, seen as topological charges, interact via a long-range potential with one another (Sec. 5.3). We take into account the effect of image charges present across the finite array and numerically show that the motion of a single vortex obeys a phenomenological equation of motion containing the vortex-vortex interaction term (Sec. 5.4).

Appendix 1.A

Description	parameter	units	Nb-Si-Nb	Al-AlO _x -Al
BCS Temperature	T_{c0}	K	9.50	1.14
BKT Temperature	T_{KT}	K	5	–
Critical Current	i_0	μA	1	0.5–0.005
Normal-state Resistance	R_n	$k\Omega$	0.5	1-100
Critical Magnetic field	$H_{c0}(T = 0)$	$Gauss$	1980	105
Magnetic Field	$H_{f=1}$	$Gauss$	0.4	0.4
Linear size	l_S	μm	5	5
Thickness	t_S	μm	0.2	0.2
Area of single junction	A_J	μm^2	0.01–0.1	0.01–0.1
London penetration depth	λ_0	μm	0.039	0.016
Coherence length	ξ_0	μm	0.04	1.60
Variation of phase in island	R_0	–	10^{-4}	10^{-5} – 10^{-7}

Table 1.1: Overview of the important array parameters.

Chapter 2

Fast Algorithms for Square Arrays

2.1 Introduction

With the size of experimental arrays increasing continuously, and with the number of interesting effects best seen only in large arrays going up in equal measure, it has become imperative to find ever more efficient algorithms for implementing the corresponding simulations, inclusive of all the experimental conditions. An example of the latter for current-driven arrays is the presence of bus-bars, through which the external current can be conveniently injected or withdrawn.

These algorithms must address the problem of integrating the complete set of coupled equations for each superconducting site describing the array in terms of the phase variables, θ_i . Within the framework of the RCSJ Model, the equations found in Sec. 1.5, have to satisfy current conservation at each site[33]. This yields the form

$$\sum_{\langle ij \rangle} \frac{C\hbar}{2e} \frac{d^2\theta_{ij}}{dt^2} + \frac{\hbar}{2eR} \frac{d\theta_{ij}}{dt} + i_0 \sin \theta_{ij} = I_i^{ext} \quad \forall i \quad (2.1)$$

where C , R and i_0 are the shunt-capacitance, shunt-resistance and critical current of the junction respectively. We note that Eq.(2.1) holds under assumptions of zero temperature, zero magnetic field and infinite perpendicular magnetic penetration depth.

The last of these allows us to neglect self-induced magnetic field effects. We can rewrite Eq.(2.1) as

$$\sum_{\langle ij \rangle} \beta_c \frac{d^2 \theta_{ij}}{d\tau^2} + \frac{d\theta_{ij}}{d\tau} + \sin \theta_{ij} = (i_{ext})_i \quad \forall i \quad (2.2)$$

where $(i_{ext})_i = I_i^{ext}/i_0$ is the normalised current being fed to or extracted from the array site i , $\beta_c = 2ei_0 R^2 C/\hbar$ is the McCumber-Stewart parameter and $\tau = t(2ei_0 R)/\hbar$ is the time measured in units of the characteristic period $\omega_c^{-1} = \hbar/(2ei_0 R)$. The summation on j , over the nearest neighbours of i , can alternatively be expressed in terms of a multiplication by the discrete laplacian, G_0^{-1} . Eq.(2.2) then assumes the matrix form

$$\sum_j (G_0^{-1})_{ij} \ddot{\theta}_j = \beta_c^{-1} [I_i^{ext} - \sum_{\langle ij \rangle} \dot{\theta}_{ij} + \sin \theta_{ij}] = -d_i \quad (2.3)$$

If we set $\theta_i = x_i$ and $\dot{\theta}_i = y_i$, the complete set of dynamical equations reads $(G_0^{-1})_{ij} \dot{y}_j = -d_i([x], [y])$ and $\dot{x}_i = y_i$. For the overdamped case, corresponding to $\beta_c = 0$, the relevant equations are

$$\sum_j (G_0^{-1})_{ij} \dot{\theta}_j = -d_i \quad (2.4)$$

where $-d_i$ is now given by $I_i^{ext} - \sum_{\langle ij \rangle} \sin \theta_{ij}$ but G_0^{-1} is, of course, the same as in Eq.(2.3).

It follows that for an $N_x \times N_y \equiv N$ array each integration time step of Eq.(2.4) has a complexity $\mathcal{O}(N^2)$. This is because at every upgradation of the N state variables, $\dot{\theta}$ in the underdamped, and θ , in the over-damped case, the constant $N \times N$ matrix G_0 has to be multiplied by the divergence vector $[d]$. It was first noticed by Eikmans and Himbergen *et al.*[122] that the form of the G_0^{-1} is such that this multiplication can actually be carried out in $\mathcal{O}(N \ln N)$ steps. The procedure was subsequently improved upon by Dominguez *et al.*[74] who combined the fast-fourier transformation used by Eikmans *et al.* with the method of cyclic reduction to achieve a roughly three-fold increase in speed. This algorithm was also used to study JJAs with inductance[110].

It is noteworthy that these algorithms are applicable even in the presence of an external magnetic field. Indeed, the application of a field, $B_0 \hat{z}$, perpendicular to the

array transforms the phases θ_{ij} into the gauge-invariant combinations $\theta_{ij} - 2\pi A_{ij}$ where $A_{ij} = 1/\phi_0 \sum_l^j \vec{A} \cdot d\vec{l}$, \vec{A} is the vector potential and $\phi_0 = \hbar/(2e)$ is the elementary flux quantum threading a plaquette. This transformation clearly affects only the divergence term, and leaves untouched the matrix G_0^{-1} , on whose form the algorithms are based. Similarly, white noise, which is taken into account by introducing a noise current into Eq.(2.3), also modifies only the divergence and hence does not affect the applicability of these algorithms. The statement continues to hold even if we introduce bond disorder, i.e. make i_0 junction-dependent (see Chap. 4).

In this chapter we extend these fast algorithms firstly to arrays with busbars and secondly to those with defects in the form of missing bonds. Busbars often form the current injection and/or extraction edges of experimental arrays. In experiments involving vortices, which are repelled by busbars, these have been used to produce collimated vortex-streets[3]. The dynamics of vortices have also been investigated with one edge shorted by a single busbar[78, 79]. Arrays with defects have likewise arisen in a number of contexts. The breakdown of superconductive flow in current-driven arrays with linear defects, for example, has been investigated in some detail. The exploration of the multiple-vortex sector, which arises in this study, requires running on large arrays and is all but impossible without the algorithm we discuss in Chap. 4. Defects can also be used to provide a collimated beam of vortices (see Chap. 5).

The chapter is organised as follows. In Sec. 2.2, we present a simplified derivation of the Eikmans-Himbergen algorithm and interpret all the key equations in the familiar language of electrodynamics. Apart from being more transparent, our derivation clarifies the role of boundaries and the connection between the lattice and continuum descriptions of the systems being studied. These insights are used in Sec. 2.3 to generalize this algorithm to arrays with busbars. The case of single busbar forces us to resort to the technique of cyclic reduction, which we consequently discuss at this point. In Sec. 2.4, we extend these algorithms to JJAs with defects, created by eliminating or adding bonds. Sec. 2.5 contains a summary and discussion of our results.

2.2 The Eikmans–Himbergen algorithm

2.2.1 Preliminaries

All efficient algorithms for the numerical integration of Eq.(2.4) make essential use of the properties of the discrete laplacian, G_0^{-1} . We thus begin by listing the more important properties of this matrix. From its definition (as given by Eqs. (2.3 and 2.4), it follows that G_0^{-1} specifies the connectivity between different sites. More precisely, $(G_0^{-1})_{ij} = (G_0^{-1})_{ji} = -1$ for $i \neq j$ (site i connected to site j) and 0 otherwise. The diagonal element $(G_0^{-1})_{ii} = \text{total number of points to which the site } i \text{ is connected}$, and hence $\text{Tr}(G_0^{-1})$ is twice the number of bonds in the network.

Clearly, G_0^{-1} is real and symmetric. As a result, its eigenvalues are real and its eigenbasis complete in the N -dimensional space of states. Furthermore, $\det(G_0^{-1}) = 0$. This can be deduced as follows. We first note that since Eq.(2.2) involves only the phase *differences* (and their time derivatives) it is invariant with respect to the global transformation $\dot{\theta}_i \rightarrow \dot{\theta}_i + \dot{\alpha}(\tau) \forall i$. Substituting this into Eq.(2.4), we have

$$\sum_j (G_0^{-1})_{ij} (\dot{\theta}_j + \dot{\alpha}(\tau)) = -d_i = \sum_j (G_0^{-1})_{ij} \dot{\theta}_j$$

This implies that $\dot{\alpha}(\tau) \sum_j (G_0^{-1})_{ij} = 0 \forall i$. I.e., if we fix i and sum over all the columns j , we get zero. (The same is true, of course, if we fix j and sum over i since the matrix is symmetric). Hence $\det(G_0^{-1}) = 0$ and only $(N - 1)$ of the N equations in Eq.(2.2) are independent. (We could, alternatively, note that $(\Psi_0)_i = 1 \forall i$ is an eigenvector of G_0^{-1} with eigenvalue 0).

To explicitly evaluate $\dot{\theta}_i$ from θ_i we have to eliminate the extra degree of freedom. For what immediately follows, the most convenient choice is $\sum_i \dot{\theta}_i = 0$. Eq.(2.4) is then replaced by

$$\sum_j (G_0^{-1})_{ij} \dot{\theta}_j = -D_i \tag{2.5}$$

where $D_i = d_i$, $i = 1 \dots (N - 1)$ and $D_N = 0$ while $(G_0^{-1})_{ij} = (G_0^{-1})_{ji}$ $i = 1 \dots (N - 1)$, $j = 1 \dots N$ and $(G_0^{-1})_{Nj} = 1 \forall j$. Moreover, the vector $[d]$ must satisfy $\sum_i d_i = 0$ as

can be seen by performing an additional sum over i in Eq.(2.4) and using the fact that $\sum_i (G_0^{-1})_{ij} = 0$. For JJAs this condition is automatically satisfied since $\dot{\theta}_{ij}$ and $\sin \theta_{ij}$ are odd functions of their arguments and the net external current fed to the array is zero.

One can, in principle, invert \mathcal{G}_0^{-1} and determine $[\dot{\theta}]$ from $[D]$. This is the usual $\mathcal{O}(N^2)$ process. We shall refrain from adopting this procedure and return, instead, to working with Eq.(2.2).

In doing so, we shall find it useful to keep in mind some electrostatic analogs of the equations we happen to be dealing with. These emerge clearly if we write the current conservation equation at the site k as

$$I_{k,\mu}^{total} = I_{k,\mu}^s + I_{k,\mu}^n + I_{k,\mu}^{ext} \quad (2.6)$$

Here $\mu = 1, 2$ represents the x and y directions respectively. Furthermore, $I_{k,\mu}^{total}$, $I_{k,\mu}^s = \sin \Delta_\mu \theta_k$, $I_{k,\mu}^n = \Delta_\mu \dot{\theta}_i$ and $I_{k,\mu}^{ext}$ are the total, superconducting, normal and external currents, respectively, at node k in the μ^{th} direction. Using the TCC condition, $\nabla \cdot I_i^{total} = 0$, we have

$$\nabla^2 \dot{\theta}_i = \nabla \cdot (\vec{I}_i^s + \vec{I}_i^{ext}) \quad (2.7)$$

On comparing Eq.(2.7) with the Laplace Equation $\nabla^2 \phi = -\rho_{total}/\epsilon_0$ and recalling that $\rho_{total} = \rho_{free} + \rho_{bound}$, we arrive at the following correspondences

$$\vec{D}(\vec{r}) \equiv \vec{I}_i^{ext} \quad (2.8)$$

$$-\vec{P}(\vec{r}) \equiv \vec{I}_i^s \quad (2.9)$$

$$\phi(\vec{r}) \equiv \dot{\theta}_i \quad (2.10)$$

Thus the condition imposed above on the $\dot{\theta}_i$ is nothing other than a choice of reference potential or gauge. We, furthermore, note that the JJA thought of as a dielectric medium is highly non-linear. Indeed, $P_{k,\mu} \equiv \sin(-\int E_{k,\mu} dt)$, where $E_{k,\mu} = \Delta_\mu \dot{\theta}_k$ is the μ^{th} component of the electric field at site k . This is to be contrasted with $\vec{P}(\vec{r}) \propto \vec{E}(\vec{r})$ for a linear dielectric.

2.2.2 The $\mathcal{O}(N \ln N)$ procedure

Going back to Eq.(2.3), G_0^{-1} can alternatively be inverted by defining the Green's function [see Jackson]

$$\tilde{G}(\vec{r}, \vec{r}') = \sum_{\lambda_{\vec{k}} \neq 0} \frac{1}{\lambda_{\vec{k}}} \Psi_{\vec{k}}(\vec{r}) \Psi_{\vec{k}}^\dagger(\vec{r}') \quad (2.11)$$

where $\lambda_{\vec{k}}$ are the eigenvalues and $\Psi_{\vec{k}}(\vec{r})$ the orthonormalised eigenvectors of G_0^{-1} , i.e.

$$G_0^{-1} \Psi_{\vec{k}}(\vec{r}) = \lambda_{\vec{k}} \Psi_{\vec{k}}(\vec{r}) \quad (2.12)$$

and \vec{r} are points on the lattice. More explicitly, the site coordinates $(x_i, y_i) \equiv \vec{r}_i$ referred to an origin located at the lower left hand corner of the lattice, are related to the site indices i used earlier by $i = (x_i - x_0) + (y_i - y_0)N_x + 1$ where (x_0, y_0) denote the coordinates of the lower left corner of the array. We note that to get a well-defined function, we must explicitly remove from the sum in Eq.(2.11), the zero mode, which necessarily exists, since G_0^{-1} is singular.

The removal of this mode, however, creates a slight problem. Indeed, if we premultiply by G_0^{-1} and use Eq.(2.12) we get

$$\begin{aligned} \sum_{\vec{r}''} G_0^{-1}(\vec{r}, \vec{r}'') \tilde{G}(\vec{r}'', \vec{r}') &= \sum_{\vec{k} \neq 0} \frac{1}{\lambda_{\vec{k}}} \lambda_{\vec{k}} \Psi_{\vec{k}}(\vec{r}) \Psi_{\vec{k}}^\dagger(\vec{r}') \\ &= \sum_{\vec{k}} \Psi_{\vec{k}}(\vec{r}) \Psi_{\vec{k}}^\dagger(\vec{r}') - \Psi_0(\vec{r}) \Psi_0^\dagger(\vec{r}') \\ &= \delta(\vec{r} - \vec{r}') - \frac{1}{\sqrt{L_x L_y}} \begin{pmatrix} 1 \\ \vdots \\ 1 \end{pmatrix} \frac{1}{\sqrt{L_x L_y}} (1, 1 \dots 1) \end{aligned} \quad (2.13)$$

which in discretised form is

$$\sum_j \tilde{G}_{ij} (G_0^{-1})_{jk} = \delta_{ik} - \frac{1}{L_x L_y} \quad (2.14)$$

Now if we multiply Eq.(2.4) from the left by \tilde{G} we get $\dot{\theta}_i - \frac{\sum_j \dot{\theta}_j}{L_x L_y}$ which reads just right, viz.

$$\dot{\theta}_i = \tilde{G}_{ij} d_j \quad (2.15)$$

provided the $\dot{\theta}_i$ satisfy $\sum_i \dot{\theta}_i = 0$. In other words, with an appropriate gauge choice, \tilde{G} does allow us to invert G_0^{-1} . Indeed, the requirement that it does so fixes the gauge uniquely. It is to be noted that Eq.(2.15) involves $[d]$ and not $[D]$.

The function, $\tilde{G}(\vec{r}, \vec{r}')$, can be easily evaluated for a periodic lattice. The form of the operator $G_0^{-1}(\vec{r}, \vec{r}')$, in this case, is given by

$$G_0^{-1}(\vec{r}, \vec{r}') = 4\delta_{\vec{r}, \vec{r}'} - \delta_{\vec{r}+\hat{e}_x, \vec{r}'} - \delta_{\vec{r}-\hat{e}_x, \vec{r}'} - \delta_{\vec{r}+\hat{e}_y, \vec{r}'} - \delta_{\vec{r}-\hat{e}_y, \vec{r}'} \quad (2.16)$$

It is easily checked that the normalised eigenvectors are of the form $\frac{\exp i\vec{k}\cdot\vec{r}}{\sqrt{L_x L_y}}$ and correspond to the eigenvalues

$$\lambda_{\vec{k}} = 4 - 2 \cos k_x - 2 \cos k_y \quad (2.17)$$

We note that $\lambda_{\vec{k}=0} = 0$.

Due to the rectangular periodicity of the lattice the eigenvectors must satisfy $\Psi_{\vec{k}}(\vec{r}) = \Psi_{\vec{k}}(\vec{r} + L_i \hat{e}_i)$ $i = x, y$. To fulfill this condition, the wavevectors must in turn be quantised as $k_i = (2n\pi)/L_i$ $i = x, y$ and $n = 0, 1, \dots (L_i-1)$. The Green's function of interest is consequently

$$\tilde{G}(\vec{r}, \vec{r}') = \frac{1}{L_x L_y} \sum_{\vec{k} \neq 0} \frac{1}{4 - 2 \cos k_x - 2 \cos k_y} \exp i\vec{k} \cdot (\vec{r} - \vec{r}') \quad (2.18)$$

We can now estimate the number of steps required to evaluate $\sum_{\vec{r}'} \tilde{G}(\vec{r}, \vec{r}') d(\vec{r}')$. The sum over \vec{r}' is a fourier transform and can be carried out in $N \ln N$ steps to produce $d(\vec{k})$. Then come the N multiplications $\lambda_{\vec{k}} d(\vec{k})$ followed by the sum over \vec{k} , which has the form of an inverse fourier transform, and requires an additional $N \ln N$ steps, making a grand total of $N(2 \ln N + 1)$ multiplications.

Quite generally then, $\dot{\theta}(\vec{r})$ can be evaluated from Eq.(2.15) by (see Fig. 2.1)

- (i) creating an constant $L_x \times L_y$ matrix $G_0(\vec{k}) = N_{\vec{k}}/\lambda_{\vec{k}}$ where $N_{\vec{k}}$ are the normalisation factors due to $\Psi_{\vec{k}}(\vec{r})$,

- (ii) evaluating $d(\vec{k}) = \sum_{\vec{r}'} d(\vec{r}') \Psi_{\vec{k}}(\vec{r}')$, this being the forward transform (W),
- (iii) computing $d'(k) = G_0(\vec{k})d(\vec{k})$, and
- (iv) taking the 2-D inverse transform \tilde{W} to get $\dot{\theta}(\vec{r}) = \sum_{\vec{k}} d'(\vec{k}) \Psi_{\vec{k}}(\vec{r})$.

For certain types of transforms and certain values of L_x and L_y , W and \tilde{W} can each be performed by matrix decomposition or row-column techniques with a complexity $\mathcal{O}(N \ln N)$. We now turn to a discussion of this procedure in the context of finite arrays.

2.2.3 The Imposition of Boundaries

For a finite array, the general form of G_0^{-1} (Eq.(2.11)) is modified since now fewer than four bonds meet at all sites on the boundary (see Fig. 2.2.3). For non-corner points on the left edge of the array for example, the operator has the form $3\delta_{\vec{r},\vec{r}'} - \delta_{\vec{r}+\hat{e}_x,\vec{r}'} - \delta_{\vec{r}\pm\hat{e}_y,\vec{r}'}$. However, if Ψ satisfies $\Psi(x_0, y) - \Psi(x_0 - 1, y) = 0 \quad \forall y$ along this edge, one can continue using the periodic form of G_0^{-1} because then $(4\delta_{\vec{r},\vec{r}'} - \delta_{\vec{r}+\hat{e}_x,\vec{r}'} - \delta_{\vec{r}\pm\hat{e}_y,\vec{r}'})\Psi(x_0, y)$ automatically reduces to $(3\delta_{\vec{r},\vec{r}'} - \delta_{\vec{r}+\hat{e}_x,\vec{r}'} - \delta_{\vec{r}\pm\hat{e}_y,\vec{r}'})\Psi(x_0, y)$. We thus see that the finiteness of the array imposes the following boundary conditions on Ψ where (x_0, y_0) and (x_L, y_L) are the diagonally opposite corners of the rectangular lattice. It is amusing to note that the left-hand side of Eqs.(2.19) are the discrete derivatives of $\Psi(x, y)$ along the edges $x = x_0$, $y = y_0$, $x = x_L$ and $y = y_L$, respectively. Thus the finite case poses for us a discretised Neumann boundary value problem.

$$\Psi(x_0, y) - \Psi(x_0 - 1, y) = 0 \quad \forall y \quad (2.19a)$$

$$\Psi(x, y_0) - \Psi(x, y_0 - 1) = 0 \quad \forall x \quad (2.19b)$$

$$\Psi(x_L, y) - \Psi(x_L + 1, y) = 0 \quad \forall y \quad \text{where} \quad x_L = x_0 + L_x - 1 \quad (2.19c)$$

$$\Psi(x, y_L) - \Psi(x, y_L + 1) = 0 \quad \forall x \quad \text{where} \quad y_L = y_0 + L_y - 1 \quad (2.19d)$$

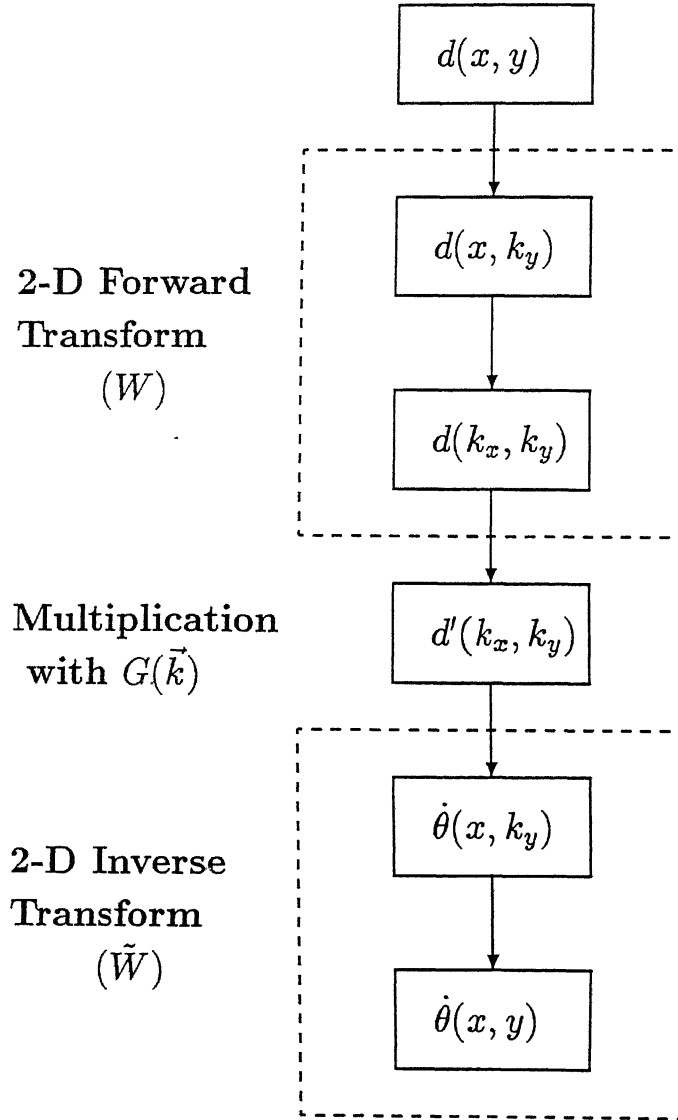


Figure 2.1: The general flowchart of the $\mathcal{O}(N \ln N)$ method. Given $d(x, y)$, one performs a 2-D forward transform and multiplies the resulting $d(k_x, k_y)$ with $G_0(k_x, k_y)$ before taking a 2-D inverse transform to get $\theta(x, y)$.

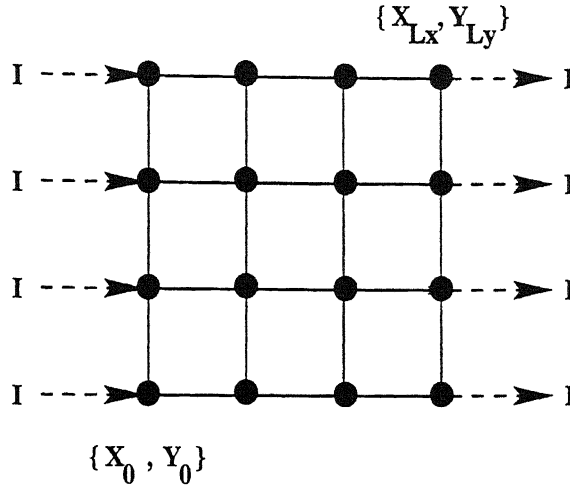


Figure 2.2: An finite $L_x \times L_y$ array with current being injected at the left edge and extracted from the right edge

Furthermore, we note that $\lambda_{\vec{k}}$ (see Eq.(2.17)) has the symmetries of the square, i.e. $\lambda_{k_x, k_y} = \lambda_{\pm k_x, \mp k_y} = \lambda_{-k_x, -k_y}$. Thus any linear combination of the corresponding eigenvectors,

$$\begin{aligned} \Psi(x, y) = & a_1 \exp i(k_x x + k_y y) + a_2 \exp i(-k_x x + k_y y) \\ & + a_3 \exp i(k_x x - k_y y) + a_4 \exp i(-k_x x - k_y y) \end{aligned} \quad (2.20)$$

is an eigenvector of G_0^{-1} with the same eigenvalue $\lambda_{\vec{k}}$. To find the specific linear combination, which satisfies the boundary conditions given above, we need merely impose each of Eqs.(2.19 a-2.19 d) in turn. Eq.(2.19 a) can be satisfied by choosing $x_0 = 1/2$, $a_1 = a_2$, $a_3 = a_4$ and the resulting wavefunction is

$$\Psi(x, y) = 2a_1 \cos k_x x \exp(ik_y y) + 2a_3 \cos k_x x \exp(-ik_y y) \quad (2.21)$$

Subjecting Eq.(2.21) next to the constraint Eq.(2.19b), we get

$$\Psi(x, y) = 4a_1 \cos k_x x \cos k_y y \quad (2.22)$$

where y_0 is now required to be $1/2$ as well. The fact that $x_0 = y_0 = 1/2$ means that the origin of coordinates is chosen on the dual lattice and both coordinates of every lattice point are half integers.

The boundary conditions Eq.(2.19c) and Eq.(2.19d) at the right and upper edges of the array can be satisfied by imposing a quantisation condition on \vec{k} . Indeed, using Eq.(2.19c) we have

$$-8a_1 \cos k_y y \sin(k_x L_x) \sin\left(\frac{k_x}{2}\right) = 0 \quad \forall y \quad (2.23)$$

whereby $k_x = n_x \pi / L_x$, $n_x = 0, 1, \dots, L_x - 1$. Similarly using Eq.(2.19d) $k_y = n_y \pi / L_y$, $n_y = 0, 1, \dots, L_y - 1$.

Thus finally, the orthonormalised wavefunctions we are looking for are

$$\Psi(x, y) = \sqrt{\frac{2}{L_x L_y}} \sqrt{\left(1 - \frac{1}{2}\delta_{k_x,0} - \frac{1}{2}\delta_{k_y,0}\right)} \cos(k_x x) \cos(k_y y) \quad \vec{k} \neq 0 \quad (2.24)$$

The resulting Green's function to be used in Eq.(2.11) is thus[122]

$$\tilde{G}(\vec{r}, \vec{r}') \frac{4}{L_x L_y} \sum_{\vec{k} \neq 0} \frac{(1 - \frac{1}{2}\delta_{k_x,0} - \frac{1}{2}\delta_{k_y,0})}{4 - 2 \cos k_x - 2 \cos k_y} \cos(k_x x) \cos(k_y y) \cos(k_x x') \cos(k_y y') \quad (2.25)$$

The action of this Green's function on a uniform current drive, $I^{ext}(x, y) = I^{ext} [\delta_{x,x_0} -$ can be rigorously shown to be (see Appendix 2.A)

$$\sum_{y'} \tilde{G}(x, y, x', y') I(x', y') = I \left(\frac{L_x}{2} - x \right) \quad (2.26)$$

2.3 Inclusion of Bus-bars

Using the techniques of the previous section we generalise the procedure to arrays with either a single or a double busbar (henceforth referred to as SBB and DBB respectively).

In the SBB case, the busbar is normally placed along the current extraction edge (see Fig. 2.3). The corresponding θ and $\dot{\theta}$ are zero for all time i.e. they do not evolve. The drive edge is however open and can be connected to *any* kind of current

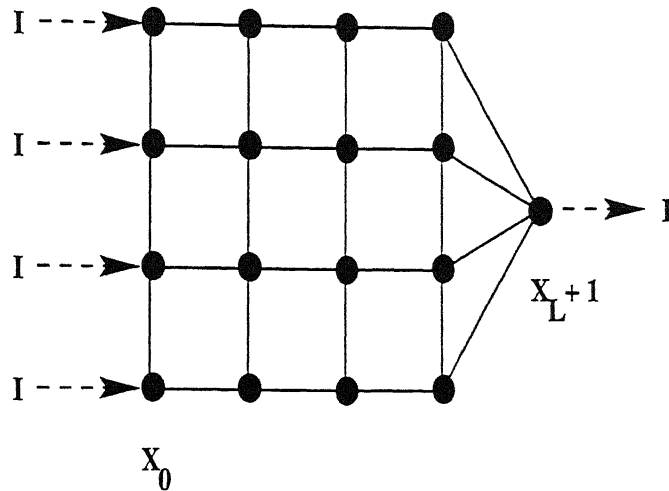


Figure 2.3: An array with a single busbar at $x_L = x_0 + L_x - 1$. The injection edge x_0 can be driven by any current profile.

profile. Such an array, with a linear profile, has been used previously to study vortex dynamics[78, 79]. On the other hand, an DBB array has shorts along a pair of parallel edges (say those at $x = x_0$ and $x = x_L + 1$ as in Fig. 2.3). In this case, no current can be injected in the x - direction but the y - direction is available to an arbitrary current drive. Such an array with electrically connected busbars could be used to simulate e.g. the “channel” in the experiments conducted by Van-der-Zant *et al.*[3].

We note that by setting the $\dot{\theta}$ along the busbar to zero and measuring all other $\dot{\theta}$'s with respect to these preassigned variables, we are unambiguously fixing the gauge. Furthermore, since the wavefunction in a rectangular system is separable, i.e. $\Psi(x, y) = \Psi_1(x)\Psi_2(y)$, any change in the boundary conditions along the x - direction, has no impact on $\Psi_2(y)$, which therefore continues to have the form derived in Sec. 2.2.3, viz.

$$\Psi_2(y) = \sqrt{\frac{2}{L_y}} \sqrt{\left(1 - \frac{1}{2}\delta_{k_y,0}\right)} \cos k_y y$$

The altered b.c.s however enter crucially into the determination of $\Psi_1(x)$ and hence in to that of $\Psi(x, y)$.

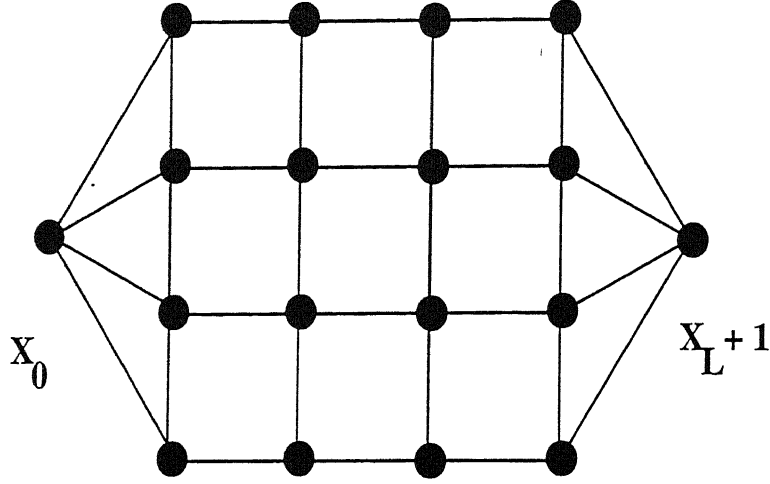


Figure 2.4: An array with a double busbars

2.3.1 Arrays with a Single Bus-bar

For the SBB case, we have the following b.c.s

$$\Psi_1(x_0) - \Psi_1(x_0 - 1) = 0 \quad \forall y \quad (2.27a)$$

$$\Psi_1(x_L + 1) = 0 \quad \forall y \text{ where } x_L = x_0 + L_x - 1 \quad (2.27b)$$

The second of these results from the fact that the wavefunction must vanish at the shorted edge as discussed above. Condition Eq.(2.27a) fixes the form of $\Psi_1(x)$ to be $\sim \cos k_x x$ where x is a half-odd integer, while Eq.(2.27b) quantises k_x : $k_x = ((2n_x + 1)\pi)/(2L_x + 1)$ $n_x = 0, 1, \dots, L_x - 1$. The normalisation constant is fixed by the requirement that $A^2 \sum_{p=1}^{L_x} \cos^2 k_x(p - \frac{1}{2}) = 1$. Thus

$$\Psi_1(x) = \sqrt{\left(\frac{2}{L_x + \frac{1}{2}}\right)} \cos k_x x \quad (2.28)$$

and hence the Green's function \tilde{G} for the case of a single busbar is

$$\tilde{G}(\vec{r}, \vec{r}') = \frac{4}{L_y(L_x + \frac{1}{2})} \sum_{\vec{k}} \frac{(1 - \frac{1}{2}\delta_{k_y,0}) \cos(k_x x) \cos(k_y y) \cos(k_x x') \cos(k_y y')}{4 - 2 \cos k_x - 2 \cos k_y} \quad (2.29)$$

The action of \tilde{G} on a uniform input drive $I^{ext}(x, y) = I^{ext}\delta_{x,x_0}$ can, as in the case of Eq.(2.26), be exactly shown to be (see 2.5)

$$\sum_{y'} \tilde{G}(x, y, x', y') I(x', y') = I \left(L_x - x + \frac{1}{2} \right) \quad (2.30)$$

Although a 1D Fast Cosine transform can be used along the y - axis, this cannot be done for the x -direction, since no *fast* Cosine transform of the form

$$C(m) = \sum_{n=0}^{L-1} \tilde{C}(n) \cos \frac{(2n+1)(2m+1)\pi}{(4L+2)}$$

is known to exist[127]. If we resort to usual matrix multiplication along \hat{e}_x , the algorithm becomes $\mathcal{O}(2NN_x + 2N \ln N_y + N)$ in complexity and is useful only if $N_y \gg N_x$.

A much more efficient approach is to combine the FCT along \hat{e}_y with cyclic reduction along the x -direction. This can be carried out as follows[128]. We begin by writing Eq.(2.4) as

$$\dot{\theta}_{x-1,y} + \dot{\theta}_{x,y'} T_{y',y} + \dot{\theta}_{x+1,y} = -d_{x,y} \quad (2.31)$$

where the operator $T_{y',y}$ is defined to be $T_{y',y} = \delta_{y',y-1} + \delta_{y',y+1} - 4\delta_{y',y}$. Taking the Cosine transform along the y - direction i. e. setting $\dot{\theta}_{x,y} = \sum_{k_y} \dot{\theta}_{x,k_y} \cos k_y y$, we find that

$$\dot{\theta}_{x,y'} T_{y',y} = \sum_{k_y} 2(\cos k_y - 2) \dot{\theta}_{x,k_y} \cos k_y y \quad (2.32)$$

As a consequence the y - cosine transform of $\dot{\theta}_{x,y}$ satisfies

$$\dot{\theta}_{x-1,k_y} + \lambda(k_y) \dot{\theta}_{x,k_y} + \dot{\theta}_{x+1,k_y} = -d_{x,k_y} \quad (2.33)$$

where we have used $\lambda(k_y) = 2(\cos k_y - 2)$. Writing Eq.(2.33) thrice with x set equal to $x-1$, x and $x+1$ respectively, multiplying the second of these equations by $-\lambda(k_y)$ and adding all the three of them together, we get

$$\dot{\theta}_{x-2,k_y} + \lambda^{(1)}(k_y) \dot{\theta}_{x,k_y} + \dot{\theta}_{x+2,k_y} = -d_{x-1,k_y} + \lambda(k_y) d_{x,k_y} - d_{x+1,k_y} = -d_{x,k_y}^{(1)} \quad (2.34)$$

where $\lambda^{(1)}(k_y) = 2 - (\lambda(k_y))^2$. We note that the x values occurring in Eq.(2.34) increase in steps of 2 as opposed to 1 in Eq.(2.33). The two equations are, however, of the same form. We can thus use the reduction procedure repeatedly to get equations with x -values increasing in steps of 4, 8, \dots until after m stages ($2^m = L_x$), we end up with a single equation for the central line of variables:

$$\lambda^{(m-1)}(k_y) \dot{\theta}_{x_0+L_x/2, k_y} = d_{x_0+L_x/2, k_y}^{(m-1)} - \dot{\theta}_{x_0, k_y} - \dot{\theta}_{x_L+1, k_y} \quad (2.35)$$

The $\lambda^{(p)}(k_y)$ and $d_{x, k_y}^{(p)}$ occurring in these equation are defined by the recursive relations:

$$\lambda^{(p)}(k_y) = 2 - \left(\lambda^{(p-1)}(k_y) \right)^2 \quad (2.36)$$

$$d_{x, k_y}^{(p)} = d_{x-2^{p-1}, k_y}^{(p-1)} - \lambda^{(p-1)}(k_y) d_{x, k_y}^{(p-1)} + d_{x+2^{p-1}, k_y}^{(p-1)} \quad (2.37)$$

Thus, if $\dot{\theta}_{x_0, k_y}$ and $\dot{\theta}_{x_L+1, k_y}$ are known, then $\dot{\theta}_{x_0+L_x/2, k_y}$ can be immediately deduced. The knowledge of $\dot{\theta}_{x_0+L_x/2, k_y}$ leads to that of $\dot{\theta}_{x_0+L_x/4, k_y}$ and $\dot{\theta}_{x_0+3L_x/4, k_y}$ which in turn determine $\dot{\theta}_{x_0+qL_x/8, k_y}$ ($q = 1, 3, 5, 7$) etc. As for the starting values, $\dot{\theta}_{x_L+1, k_y} = 0 \forall k_y$, since this is the y -cosine transform of $\dot{\theta}_{x, y}$ for $x = x_L + 1$, i.e. taken along the busbar. $\dot{\theta}_{x_0, k_y}$ must however be determined by explicit multiplication. Fortunately, since we know the relevant Green's function explicitly, we can carry this out in $\mathcal{O}(N)$ steps, by taking the cosine transform of Eq.(2.15):

$$\dot{\theta}_{x_0, k_y} = \frac{4}{L_y(L_x + \frac{1}{2})} \sum_{k_x} \sum_{x'} \frac{\left(1 - \frac{1}{2} \delta_{k_y, 0}\right)}{4 - 2 \cos k_x - 2 \cos k_y} \cos k_x x_0 \cos k_x x' d_{x', k_y} \quad (2.38)$$

The number of steps required to evaluate all the higher-order divergences $d_{x, k_y}^{(p)}$, $p = 1, \dots, m-1$ used by the method can be performed as follows. For a given N_x the number of higher order divergences that need to be calculated (starting from level 0 which correspond to ordinary divergence) is given by $f = \ln_2 N_x - 1$. At the $(f - m)^{\text{th}}$ level there $2^{m+1} - 1$ divergence vectors which need to be calculated. Each such calculation requires N_y multiplications. Thus the total number of multiplications is

$$N_y \left[\sum_{m=0}^{f-1} (2^{m+1} - 1) \right] = N_y \left[\frac{N_x}{2} - \ln_2 N_x \right] \quad (2.39)$$

With these divergences in hand, the cyclic determination of θ_{x,k_y} has a complexity $\mathcal{O}(N)$. Adding to all this, the number of multiplications involved in carrying out the forward and backward FCTs in the y -direction, we conclude that the entire procedure can be carried out in $\mathcal{O}(2N \ln N_y + 2N + N/2 - N_y \ln_2 N_x)$ steps. The restriction of L_x to integral powers of 2 can be removed as shown in Ref.[129]. The whole procedure is described in Fig. 2.5.

2.3.2 The Case of a Double Bus-bar

Turning now to the DBB case, we note that the wave-function, $\Psi_1(x)$, must now satisfy the following b.c.s

$$\Psi_1(x_0) = 0 \quad \forall y \quad (2.40a)$$

$$\Psi_1(x_L + 1) = 0 \quad \forall y \quad (2.40b)$$

Condition Eq.(2.40a) fixes the form of $\Psi_1(x)$ to be $\sim \sin k_x x$ where x is an integer while condition Eq.(2.40b) restricts k_x to the values $(n_x \pi)/(L_x + 1)$, $n_x = 1, \dots, L_x$. The normalisation constant, A , is fixed by $A^2 \sum_{p=1}^{L_x} \sin^2 k_x p = 1$. The resulting orthonormalised wavefunction is then

$$\Psi_1(x) = \sqrt{\frac{2}{L_x + 1}} \sin k_x x \quad (2.41)$$

and hence \tilde{G} for an array with a double bus-bar is

$$\tilde{G}(\vec{r}, \vec{r}') = \frac{4}{L_y(L_x + 1)} \sum_{\vec{k}} \frac{(1 - \frac{1}{2}\delta_{k_y,0}) \sin(k_x x) \cos(k_y y) \sin(k_x x') \cos(k_y y')}{4 - 2 \cos k_x - 2 \cos k_y} \quad (2.42)$$

This \tilde{G} coincides with the G_0 for this case because the zero-mode is absent. In this case, the transformations along both directions are amenable to fast, i.e. $\mathcal{O}(N \ln N)$, procedures provided $L_x + 1$ and L_y are both integral powers of 2.

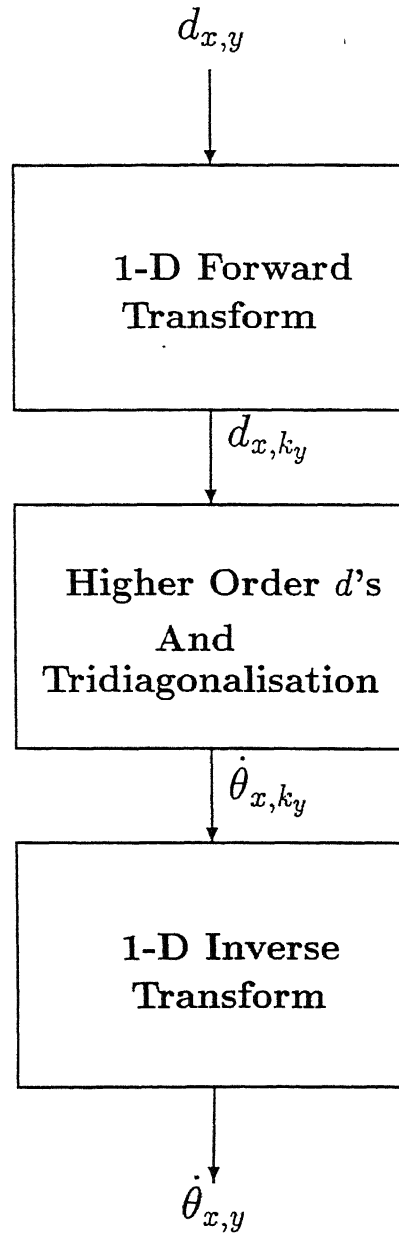


Figure 2.5: The general flowchart of the procedure described in Sec.2.3.1. Given $d_{x,y}$, one performs a 1-D forward transform to get d_{x,k_y} , calculates the higher order divergences (d_{x,k_y}^p) and uses tridiagonalisation to get $\dot{\theta}_{x,k_y}$. Finally, a 1-D inverse transform provides $\dot{\theta}_{x,y}$.

For the case of periodic boundary conditions in one direction (say y), one can use the fast algorithms by simply noting that $\Psi_2(y) \sim \exp ik_y y$ with $k_y = 2n\pi/L_y$. In this case, one would use a fourier as opposed to a cosine transform in the y direction, for the SBB case. For the DBB case, cyclic reduction can be used in the x direction with a fourier transform along the y or alternatively in the y direction with a sine transform along x . Arrays with such boundary conditions have been used by many authors in their numerical studies[57, 74, 77, 109]

2.4 Defects

We move on next onto arrays containing defects in the form of broken bonds. As mentioned in Sec. 2.1, arrays of this sort have recently attracted the attention of several groups. Xia and Leath showed that in contrast to networks of resistors[130, 131], where breakdown emanates from the most critical defect, JJAs with missing bonds do not become resistive, the moment any one junction turns critical. Cohn *et al.*[104] showed that defects exert an additional pinning force on a vortex placed in the system. In Chap. 4 we demonstrate the existence of multiple vortex sectors in the steady state configurations of the system. This is done by running on large arrays using a modified version of the above algorithm which we now describe in detail.

The evolution equation $\dot{\theta}$ for an array containing a single missing bond between the sites $k \equiv (x_0, y_0)$ and $(k+1) \equiv (x_0+1, y_0)$ can be written in matrix notation (see Eq.(2.2)) as

$$(G_0^{-1} + h)[\dot{\theta}] = [d] \quad (2.43)$$

where G_0^{-1} is the discrete Laplacian with free, periodic, SBB or DBB boundary conditions and h is given by

$$\begin{aligned} h_{k,k} &= h_{k+1,k+1} = -1 \\ h_{k,k+1} &= h_{k+1,k} = 1 \\ h_{i,j} &= 0 \quad i, j \neq k, k+1 \end{aligned} \quad (2.44)$$

Multiplying Eq.(2.43) with \tilde{G} from the left we get

$$(I + A)[\dot{\theta}] = \tilde{G}[d] = \xi \quad (2.45)$$

where $A = \tilde{G}h$ and I is the identity matrix. The process of determining $\tilde{G}[d] = \xi$, as already been outlined and can be executed in $N \ln N$ steps. One then needs to evaluate $(1 + A)^{-1}\xi$ efficiently. To this end, we note that A has the form

$$A_{ij} = X_i(\delta_{j,k} - \delta_{j,k+1}) \quad (2.46)$$

where the numbers X_i are got by explicitly by multiplying G_0 and h . From Eq.(2.46) it follows that

$$A^q = A(\Delta e)^{q-1} \quad (2.47)$$

where $\Delta e = X_k - X_{k+1}$. In fact, Δe is the only non-zero eigen value of the matrix A and for the case of SBB discussed in Sec. 2.2.3 it is given by

$$\Delta e = \frac{4}{L_x L_y} \sum_{\tilde{k} \neq 0} \frac{(1 - \frac{1}{2}\delta_{k_x,0} - \frac{1}{2}\delta_{k_y,0})}{4 - 2 \cos k_x - 2 \cos k_y} (\cos k_x(x_0 + 1) - \cos k_x x_0)^2 \cos^2 k_y y_0 \quad (2.48)$$

where $k_i = (n_i \pi)/L_i$, $n_i = 0 \dots L_i - 1$ and $i = x, y$. From Eq.(2.47) it follows that

$$(I + A)^{-1} = I - A + A^2 - A^3 + \dots = I - \frac{A}{1 + \Delta e} \quad (2.49)$$

Since the constant matrix $R = -A/(1 + \Delta e)$ contains only two non-zero columns, which are moreover negatives of each other, $[\dot{\theta}]$ can be determined from ξ in just N multiplicative steps.

The extension of the above procedure to the case of a linear defect[77] consisting of n broken bonds is straight forward as each additional defect introduces into h a 2×2 diagonal block of the form given in Eq.(2.44). In this case, the series (Eq.(2.49)) cannot be summed analytically due to the presence of cross terms. An analytic summation is, however, unnecessary. It is sufficient to note that

$$A_{ij} = X_i^1(\delta_{j,k_1} - \delta_{j,k_1+1}) + X_i^2(\delta_{j,k_2} - \delta_{j,k_2+1}) + \dots + X_i^n(\delta_{j,k_n} - \delta_{j,k_n+1}) \quad (2.50)$$

for bonds missing between k_i and k_{i+1} ($i = 1, 2 \dots n$), and that consequently A^q has the same form as above. The numbers X_i^p 's occurring in A^q are of course q -dependent. It follows from this that the series can once again be written in the form

$$(I + A)^{-1} = I + R \quad (2.51)$$

where R is a constant matrix of the form given in Eq.(2.50). Clearly the action of R on a vector of length N can be determined in nN multiplicative steps. The overall complexity of the algorithm in this case is thus $\mathcal{O}(N \ln N + nN)$. Since the number of broken bonds required to observe various breakdown phenomena[77] is much smaller than N , this results in a very large saving in the time required to perform the computations.

It is interesting to note that the Green's function for the broken bond system G^{bb} satisfies the Dyson's equation[132]

$$G^{bb} = \tilde{G} + \tilde{G}(-h)G^{bb} \quad (2.52)$$

The matrix $(-h)$ is thus the analog of the potential due to an impurity in an otherwise perfect lattice and the case of the single defect is the analog of the δ function impurity at a given site in the system.

The procedure developed above is for the situation where no pair of broken bonds has any site in common. This ensures that the block matrices introduced in h are always 2×2 rather than $m \times m$, $m > 2$. The general case can be dealt with in a similar manner albeit with an increase in complexity. Lastly, bonds can be added in the interior of the network rather than being eliminated since this does not violate the constraint $\sum_i d_i = 0$.

2.5 Summary And Discussion

To summarize, we have extended the Eikman-Himbergen algorithm to a number of practically occurring situations. In particular, we have extended it to the case of a

bus-bar placed along one edge of a rectangular array as also to that of electrically connected bus-bars placed along two parallel edges. Finally we have shown that our simulation can be carried out, with only a marginal increase in complexity, for bonds eliminated from or added to the array. In all cases, the open edges can be connected to current sources having any profile whatsoever.

The algorithms for bus-bars as also for perfect arrays subject to magnetic fields, noise, and/or current drives, all involve Green's functions specific to the lattice in question. The Green's function of interest can straight-forwardly be constructed once the eigen-basis of the corresponding connectivity matrix or discrete Laplacian has been determined. We have shown that this eigen-basis consists precisely of those linear combinations of eigenfunctions of the connectivity matrix for a *periodic* lattice, which satisfy an appropriate set of boundary conditions.

The addition and removal of bonds introduces additional boundaries often in the interior of the array. As a result our earlier procedure becomes invalid. An island of defects created at the center of the array, e.g., defines a lattice version of the *sinai* billiard problem, which classically has only chaotic solutions. However if the number of bonds eliminated is small, Green's function techniques which have been extensively used to study disordered solids can be very effectively applied. We have shown that this technique yields an $\mathcal{O}(N \ln N + nN)$ algorithm. The extensions of such algorithms to the case of 3D arrays is easy since the corresponding eigen-vectors are specified to be either $\exp(i\vec{k} \cdot \vec{r})$ or $\cos(k_x x)$ depending on whether the boundaries are periodic or free boundaries respectively. The eigen-values are now changed to $6 - 2\cos k_x - 2\cos k_y - 2\cos k_z$. In this case, one has to obviously use 3-D transforms.

It is also worth noting that many of the expressions we have derived can be written in terms of continuous functions, which are, of course, to be evaluated or sampled only at points belonging to the array. Now if we turn this observation around and think of the discrete lattice as being *produced* by the sampling of the continuous 2-D waveform, we make contact with a long-standing problem in electrical engineering, viz. that of the digitisation and subsequent recovery of band-width limited analog wave-forms. Usually

such waveforms are processed as rectangular spaced arrays i. e. they are periodically sampled along the two orthogonally independent variables. However, one can also use hexagonal sampling[133]. Once discretised, the waveforms can be processed as arrays of numbers $x(n_1, n_2)$ by the computer where (n_1, n_2) is a discrete point on which the observable x has some value. The periodicity of the observable $x(n_1, n_2)$ is important as it specifies the eigenfunctions associated with the system. The matrix G_0^{-1} has precisely the information about the chosen sampling raster and the periodicity of the lattice. The raster defines the total number of nearest neighbours of a general site (n_1, n_2) while the periodicity (or finiteness) of the lattice decides the connectivity of the sites at the boundary of the network. The eigenfunctions used in both cases are the same. Indeed, the analogy goes deeper and we can think of the JJA itself as a latticized version of the continuum case (superconducting islands embedded in a normal background much as the Abrikosov lattice consists of normal regions embedded in a superconducting background). Finally, since hexagonally sampled waveforms can be recovered in $\mathcal{O}(N \ln N)$ steps, this analogy opens up the very interesting possibility of working out $\mathcal{O}(N \ln N)$ algorithm for a triangular JJA (see Chap. 3).

Appendix 2.A

In this appendix we show that the effect of a constant current applied at the edges of a finite array. The sum as in Eq.(2.26) can be written as

$$\begin{aligned} \tilde{X}(x, y) &= I \left[\sum_{y'} G(\vec{r}, x' = 1/2, y') - G(\vec{r}, x' = L_x - 1/2, y') \right] \\ &= \frac{4I}{L_x L_y} \sum_{y'} \sum_{\vec{k}} \frac{(1 - 1/2\delta_{k_x,0} - 1/2\delta_{k_y,0})}{4 - 2\cos k_x - 2\cos k_y} \cos k_x x \cos k_y y \\ &\quad \left[\cos k_x/2 - \cos k_x(L_x - \frac{1}{2}) \right] \cos k_y y' \end{aligned} \quad (2.A.1)$$

Noting that $\sum_{y'} \cos k_y y' = L_y \delta_{k_y,0}$ and $k_x \neq 0$ (since $k_y = 0$) this gives

$$\tilde{X}(x) = \frac{I}{L_x} \sum_{k_x \neq 0} \frac{\cos k_x x \sin^2 \frac{k_x L_x}{2} \cos \frac{k_x}{2}}{\sin^2 \frac{k_x}{2}} \quad (2.A.2)$$

independent of y . Since x , y and y' are half-odd integers and $k_i = (n_i\pi)/L_i$, $i = x, y$ we can rewrite the above expression as

$$\tilde{X}(m) = \frac{2I}{L_x} \sum_{n=1}^{L_x-1} X(n) \cos \frac{\pi n(m+1/2)}{L_x} \quad (2.A.3)$$

where $0 \leq m \leq (L_x - 1)$ and

$$X(n) = \frac{\sin^2 \frac{n\pi}{2} \cos \frac{n\pi}{2L_x}}{\sin^2 \frac{n\pi}{2L_x}} \quad (2.A.4)$$

Now we claim that

$$\tilde{X}(m) = I \left(\frac{L_x - 1}{2} - m \right) = I \left(\frac{L_x}{2} - x \right) \quad (2.A.5)$$

To prove this we define $X(0) = 0$, then

$$\tilde{X}(m) = \frac{L_x - 1}{2} - m = \frac{2}{L_x} \sum_{n=0}^{L_x-1} k_n \cos \frac{(2m+1)n\pi}{2L_x} X(n)$$

where $k_0 = 1/\sqrt{2}$ and $k_n = 1$ for $n \neq 0$. This is exactly the forward cosine transform of $X(n)$ [127]. The inverse cosine transform is

$$X(n) = k_n \sum_{m=0}^{L_x-1} \tilde{X}(m) \cos \frac{(2m+1)n\pi}{2L_x}$$

which for $n = 0$ gives

$$X(0) = \frac{1}{\sqrt{2}} \sum_{m=0}^{L_x-1} = \frac{1}{\sqrt{2}} \left[\frac{(L_x - 1)L_x}{2} - \frac{L_x(L_x - 1)}{2} \right] = 0$$

as required.

For $n \neq 0$, we get $X(n) = -\sum_{m=0}^{L_x-1} m \cos \left[\frac{(2m+1)n\pi}{2L_x} \right]$ since the first term yields 0 when $n \neq 0$. Expanding the cosine term and using the identities[134]

$$\begin{aligned} \sum_{m=0}^{L_x-1} m \sin \frac{mk\pi}{L_x} &= \frac{\sin k\pi}{4 \sin^2 \frac{k\pi}{2L_x}} - \frac{L_x \cos \frac{2(L_x-1)k\pi}{2L_x}}{2 \sin \frac{k\pi}{2L_x}} \\ \sum_{m=0}^{L_x-1} m \cos \frac{mk\pi}{L_x} &= \frac{L_x \sin \frac{(2L_x-1)k\pi}{2L_x}}{2 \sin \frac{k\pi}{2L_x}} - \frac{1 - \cos \frac{L_x k\pi}{L_x}}{4 \sin^2 \frac{k\pi}{2L_x}} \end{aligned} \quad (2.A.6)$$

This yields the required result for $X(n)$ (Eq.(2.A.4)).

This appendix shows the effect of a constant current applied to a SBB configuration. To evaluate the sum as in Eq.(2.30) we once again use the above procedure whereby

$$\tilde{X}(x, y) = I \sum_{y'} G(\vec{r}, x' = 1/2, y') \quad (2.B.1)$$

$$= \frac{4I}{(L_x + 1/2)L_y} \sum_{y'} \sum_{\vec{k}} \frac{(1 - 1/2\delta_{k_x,0})}{4 - 2\cos k_x - 2\cos k_y} \cos k_x x \cos k_y y \cos k_x/2 \cos k_y y' \quad (2.B.2)$$

where $k_y = (n_y\pi)/L_y$ and $k_x = ((2n_x + 1)\pi)/(2L_x + 1)$. Noting once again using the fact the the y' summation yields $L_y\delta_{k_y,0}$ and that x, y are both half-odd integers we can rewrite the above expression as

$$\tilde{X}(m) = \frac{2I}{L_x + 1/2} \sum_{n=0}^{L_x-1} X(n) \cos \frac{(2n+1)(2m+1)\pi}{4L_x+2} \quad (2.B.3)$$

where

$$X(n) = \left(\cos \frac{(2n+1)\pi}{4L_x+2} \right) / \left(\sin^2 \frac{(2n+1)\pi}{4L_x+2} \right) \quad (2.B.4)$$

We claim that

$$\tilde{X}(m) = I(L_x - n) = I(L_x - x + \frac{1}{2}) \quad (2.B.5)$$

To prove this one needs to first determine the inverse transform of Eq.(2.B.3). Although such a transform is rarely used, one can show that the inverse transform is

$$X(n) = \sum_{m=0}^{L_x-1} \tilde{X}(m) \cos \frac{(2n+1)(2m+1)\pi}{4L_x+2} \quad (2.B.6)$$

Now using Eq.(2.B.5) in Eq.(2.B.6) and the identities (Eq.(2.A.6)), it can be shown that indeed one gets Eq.(2.B.4).

Chapter 3

Fast Algorithms For Triangular Arrays

3.1 Introduction

Various experimental[32] and numerical studies[30, 37, 74, 76] studies on JJAs indicate that vortices, which are natural excitations of the system, play an important role in determining both the equilibrium and dynamical properties of these arrays. The behaviour of vortices, in turn, depends in large part on the vortex pinning potential, which arises from the discreteness of the lattice. Many features of vortex behaviour are thus better understood by varying the pinning potential. This can be achieved by switching to a triangular lattice, which has a ~ 5 times smaller pinning potential than a square array[61]. Triangular lattices are hence better suited for the study of the dynamics of an ideal 2D gas of vortices[4]. They also provide a better chance for the observation of ballistic vortex motion, i.e. the motion of a “massive” vortex through a force-free region due to its own inertia, which has been predicted theoretically[135, 55, 53, 136] and has to some extent been investigated experimentally[3] and numerically[56, 57, 59, 137]. The geometry of the hexagon, which occurs naturally in triangular arrays,

allows us to conveniently study the Aharonov–Casher effect wherein vortices, as quantum objects, can interfere constructively or destructively after following two different paths enclosing a charge placed at the center of the hexagon[119]. The ground state configuration of triangular arrays under the application of an external magnetic field has unique features of its own. For example domain wall superlattices[138] occur at characteristic values of f , the quantum of magnetic flux threading a plaquette, and there is an accidental degeneracy of the ground state for $f = 1/3$ and $1/4$ [139]. In fact, there are indications that the case of $f = 1/4$ belongs to the same universality class as the fully frustrated $f = 1/2$ case of the square lattice[94, 140]. It has also been observed that the presence or absence of fractional Shapiro steps depends on the relative orientation of the lattice and the external current drive[141]. Lastly, we note that a triangular configuration of three capacitive[142] and resistive[143] junctions offers the simplest geometry capable of sustaining a vortex while being amenable to explicit theoretical analysis.

As indicated in Chap. 2, a number of authors have evolved fast algorithms for square lattices with a variety of boundary conditions. No fast algorithms have however been discovered so far for the case of triangular arrays making numerical work with the latter prohibitively time consuming. We, accordingly, take up next the task of filling this lacuna.

3.2 Notation

The algorithms which we develop in this chapter can very conveniently be discussed in terms of the bra–ket formalism of Dirac[144, 145]. A given state of the system corresponds to a specific configuration of the θ ’s and can be denoted by $|\theta\rangle$. In the position basis $\{|\vec{x}\rangle \equiv |x_1, x_2\rangle\}$, the components of $|\theta\rangle$ are obtained by taking the usual projections $\langle x_1, x_2|\theta\rangle = \theta(x_1, x_2)$. We note that the coordinates (x_1, x_2) of the various lattice sites are related to the labels i used in Eq.(2.4) by $(x - x_0) + (y - y_0)N_x + 1$ where (x_0, y_0) are the coordinates the bottom–left corner of the array. We could alternatively

consider the components $\theta(k_1, k_2) = \langle \vec{k} | \theta \rangle$ in the momentum basis $\{|\vec{k}\rangle\}$. These are related to $\theta(x_1, x_2)$ by the unitary transformation matrix $\langle \vec{k} | \vec{x} \rangle$:

$$\theta(k_1, k_2) = \sum_{\vec{x}} \langle \vec{k} | \vec{x} \rangle \langle \vec{x} | \theta \rangle \quad (3.1)$$

where the summation is to be carried out over all the lattice points. The validity of this equation as also the unitarity of $\langle \vec{k} | \vec{x} \rangle$ rests on the completeness of the two bases in the N - dimensional space of interest:

$$I = \sum_{\vec{x}} |\vec{x}\rangle \langle \vec{x}| = \sum_{\vec{k}} |\vec{k}\rangle \langle \vec{k}| \quad (3.2)$$

where I is the N dimensional Identity matrix. Both bases are further assumed to be orthonormal, i. e.

$$\langle \vec{x} | \vec{x}' \rangle = \delta_{x_1, x'_1} \delta_{x_2, x'_2} \quad \text{and} \quad \langle \vec{k} | \vec{k}' \rangle = \delta_{k_1, k'_1} \delta_{k_2, k'_2} \quad (3.3)$$

We note that the delta functions occurring in Eq.(3.3) are the kronecker (as opposed to dirac) deltas. Furthermore, Eq.(3.3) indicates that in the position basis, the vector $|\vec{x}\rangle$ is zero at all points other than $\vec{x} \equiv (x_1, x_2)$ where it is 1.

The $\dot{\theta}_i$ and the divergence d_i similarly give rise to the vectors $|\dot{\theta}\rangle$ and $|d\rangle$. Eq.(2.15) is then

$$G_0^{-1} |\dot{\theta}\rangle = |d\rangle \quad (3.4)$$

written out in the position basis.

The underpinnings of the fast algorithms can now be made transparent by writing Eq.(2.15) as follows:

$$\begin{aligned} \langle \vec{x} | \dot{\theta} \rangle &= \langle \vec{x} | \tilde{G} | d \rangle \\ &= \sum_{\vec{x}'} \sum_{\vec{k}} \sum_{\vec{k}'} \langle \vec{x} | \vec{k} \rangle \langle \vec{k} | \tilde{G} | \vec{k}' \rangle \langle \vec{k}' | \vec{x}' \rangle \langle \vec{x}' | d \rangle \end{aligned} \quad (3.5)$$

We note that the r. h. s. of Eq.(3.5) involves

- (i) Evaluating $\sum_{\vec{x}'} \langle \vec{k}' | \vec{x}' \rangle \langle \vec{x}' | d \rangle = \langle \vec{k}' | d \rangle$. This is the forward transform W and can be executed in certain cases with complexity $\mathcal{O}(N \ln N)$
- (ii) Multiplying $\langle \vec{k}' | d' \rangle$ by $\langle \vec{k} | \tilde{G} | \vec{k}' \rangle$ i. e. the operator \tilde{G} expressed in the \vec{k} basis, to get $\langle \vec{k} | d' \rangle$. If \tilde{G} happens to be diagonal in this basis, the multiplication can be carried out in N steps.
- (iii) Taking the backward transform \tilde{W} i. e. $\sum_{\vec{k}} \langle \vec{x} | \vec{k} \rangle \langle \vec{k} | d' \rangle$. Here too, the complexity, for some cases, is $\mathcal{O}(N \ln N)$.

It follows that we have a fast algorithm for a given lattice as soon as we have discovered a basis $\{|\vec{k}\rangle\}$ which (i) is related to the position basis $\{|\vec{x}\rangle\}$ by a fast transform of some sort and (ii) completely or almost completely diagonalises the corresponding \tilde{G} or G_0^{-1} .

For a periodic $L_1 \times L_2$ square lattice (where L_1 and L_2 refer to the lengths in the x and y directions respectively)

$$\langle \vec{x}' | G_0^{-1} | \vec{x} \rangle = (4\delta_{\vec{x}, \vec{x}'} - \delta_{\vec{x}, \vec{x}'+\hat{e}_1} - \delta_{\vec{x}, \vec{x}'-\hat{e}_1} - \delta_{\vec{x}, \vec{x}'+\hat{e}_2} - \delta_{\vec{x}, \vec{x}'-\hat{e}_2}) \quad (3.6)$$

and the basis defined by

$$\langle \vec{x} | \vec{k} \rangle = \frac{1}{\sqrt{L_1 L_2}} \exp(i\vec{k} \cdot \vec{x}) \quad (3.7)$$

with $k_i = 2n_i\pi/L_i$, does the job. The transform W and \tilde{W} in this case are the usual direct and inverse fast fourier transforms respectively, and \tilde{G} is clearly diagonal:

$$\langle \vec{k}' | \tilde{G} | \vec{k} \rangle = \frac{1}{4 - 2\cos k_x - 2\cos k_y} \langle \vec{k}' | \vec{k} \rangle = \frac{1}{\lambda_{k_x, k_y}} \delta_{\vec{k}', \vec{k}} \quad (3.8)$$

For a finite square lattice, the G_0^{-1} matrix, on the other hand, is

$$\begin{aligned} \langle \vec{x}' | G_0^{-1} | \vec{x} \rangle = & (\delta_{\vec{x}, \vec{x}'} - \delta_{\vec{x}, \vec{x}'-\hat{e}_1})(1 - \delta_{x_1, x_0}) + (\delta_{\vec{x}, \vec{x}'} - \delta_{\vec{x}, \vec{x}'+\hat{e}_1})(1 - \delta_{x_1, x_0+L_1-1}) \\ & + (\delta_{\vec{x}, \vec{x}'} - \delta_{\vec{x}, \vec{x}'-\hat{e}_2})(1 - \delta_{x_2, y_0}) + (\delta_{\vec{x}, \vec{x}'} - \delta_{\vec{x}, \vec{x}'+\hat{e}_2})(1 - \delta_{x_2, y_0+L_2-1}) \end{aligned} \quad (3.9)$$

where (x_0, y_0) are the coordinates of the bottom-left edge of the array. The \vec{k} -basis is now given by

$$\langle \vec{x} | \vec{k} \rangle = N_{\vec{k}} \cos k_1 x_1 \cos k_2 x_2 \quad (3.10)$$

where $k_i = n\pi/L_i$, $1/2 \leq x_i \leq L_i - 1/2$; $i = 1, 2$ and $N_{\vec{k}}$ are the normalisation constants. We note that the set of $|\vec{k}\rangle$ vectors spans the vector space of states/configurations and moreover diagonalises \tilde{G} . The transforms W and \tilde{W} are now the direct and inverse fast discrete cosine transforms.

It is to be noted that the $\{|\vec{k}\rangle\}$ basis is different for different lattices. Strictly speaking, we should introduce a new symbol each time to indicate this. However, that would make the notation cumbersome. We, accordingly, use the symbol $\{|\vec{k}\rangle\}$ uniformly and let the context and the explicitly stated form of $\langle \vec{x} | \vec{k} \rangle$ decide its precise meaning.

3.3 Periodic Triangular Lattice : Sampling Strategies

In contrast to square lattices which have four nearest neighbours, triangular lattices have six nearest neighbours. The connectivity matrix G_0^{-1} is therefore different in this case. Moreover, the bonds are at a relative angle of 60° to each other. Such configurations are found in crystallographic studies and in various radio physics applications (e.g. radar). We, therefore, digress for a moment to study how such lattices are constructed especially in the context of Digital Signal Processing. In the process we learn some important techniques applicable to the JJA context.

It is well known that both square as well as triangular lattices can be created by sampling a 2-D continuous waveform can be sampled at certain discrete points[146]. The value of any variable, say Φ , is measured at these discretised points. Intuitively, rectangular sampling i.e. periodic sampling along the two orthogonally independent directions is the most common. Such a sampling produces, in general, a rectangular lattice and hence a discrete Φ field.

$$\langle \vec{n} | \Phi \rangle = \Phi(n_1, n_2) = \Phi_a(n_1 a, n_2 b) \quad \text{where } n_1, n_2 = 0, 1, 2, \dots \quad (3.11)$$

and Φ_a is the corresponding continuous (analog) waveform. One of the many assets of using such sampling is its separability whereby the sampling along each of the axis is independent

$$\langle \vec{n} | \Phi \rangle = \langle n_1 | \Phi_1 \rangle \langle n_2 | \Phi_2 \rangle = \Phi_1(n_1 a) \Phi_2(n_2 b) \quad (3.12)$$

Here a and b are the units in which sampling is done along the two directions.

There exists other sampling strategies e. g. hexagonal sampling which essentially produces a triangular lattice (see Fig. 3.1). Mathematically, this sampling is described as

$$\langle \vec{n} | \Phi \rangle = \Phi(n_1, n_2) = \Phi_a\left(\frac{2n_1 - n_2}{2}a, n_2 b\right) \quad (3.13)$$

whereby each odd row is shifted half a unit from the even rows in the n_1 direction. Unlike rectangular sampling, this is not separable in the variables n_1 and n_2 . However, as shown by Merserau[133], such a sampling has the added advantage in that it requires fewer samples to describe the analog waveform restricted to a particular area.

Periodicity of the observable $\Phi(n_1, n_2)$ is another important concept and finiteness (as in finite JJAs) essentially disrupts the periodicity. In the most general case, the observable Φ is said to be periodic if it obeys

$$\Phi(\vec{n}) = \Phi(\vec{n} + N\vec{r}) \quad (3.14)$$

where N is a 2×2 matrix and \vec{r} is any 2D integer vector. Here too, the most obvious choice is rectangular periodicity whereby

$$\Phi(n_1, n_2) = \Phi(n_1 + L_1, n_2) = \Phi(n_1, n_2 + L_2) \quad (3.15)$$

However, for some lattices, (e.g. triangular lattices) one can have in *addition* to rectangular periodicity, hexagonal periodicity which is defined as

$$\begin{aligned} \Phi(n_1, n_2) &= \Phi(n_1 + 2L_1 + L_2, n_2) \\ &= \Phi(n_1 + L_1 + L_2, n_2 + L_2) \\ &= \Phi(n_1 + L_1, n_2 + 2L_2) \end{aligned} \quad (3.16)$$

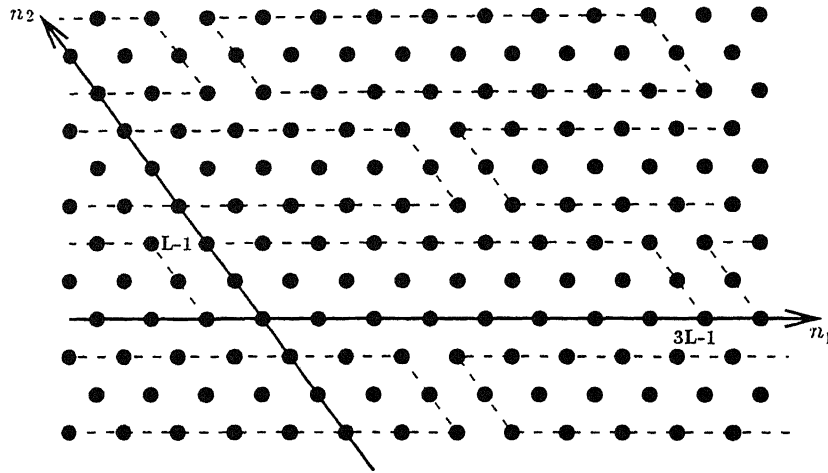


Figure 3.1: A sampling strategy for triangular arrays producing tiles

Such periodicity, when imposed on an infinite triangular lattice, produce a tiling (see Fig. 3.1) of the latter by the array in question (this has been referred to as the “fundamental period” in Ref.[133]). This tiling is quite distinct from the one which follows from the conditions (3.15). If corresponding points on different tiles are now identified with one another, one immediately obtains the connectivity of points on the boundary of each tile. For example, in the rectangularly periodic lattice of Fig. 3.2, the points carrying the same labels on the top and bottom rows (left and right columns) are treated as identical. In other words, the lattice is folded like a torus. The folding of the hexagonally periodic lattice of Fig. 3.3, on the other hand, is quite unfamiliar but follows straight-forwardly from the tiling displayed in Fig. 3.3. The points to be identified here have, as before, been given identical labels. We should mention that the above identification can be physically be realised through the use of electrical shorts. For a given value of L_1 and L_2 the number of samples present in a tile is given by $\det N$. In the case of a diagonal N , as in the rectangularly periodic case,

$\det N = L_1 L_2$ while for the hexagonally periodic case it is $L_2(2L_1 + L_2)$. For further details on hexagonal periodicity, we refer the reader to Ref.[133]. Apart from specifying the connectivity of an arbitrary site, the underlying periodicity limits the choice of eigenfunctions $\langle \vec{x} | \vec{k} \rangle$ needed to diagonalize the corresponding laplacian G_0^{-1} . With a knowledge of the sampling strategy and the periodicity of the variable, the important task for electrical engineers is the complete recovery of a bandwidth limited analog waveform Φ_a , from the given samples, Φ (called the sampling theorem). This is done by taking various transforms e. g. Fourier Transform in the case of rectangularly periodic samples and Hexagonal Fourier Transforms in the case of hexagonally periodic samples. When L_i 's are restricted to 2^p , the corresponding fast transforms are used. The G_0^{-1} matrix in the case of JJAs has precisely the information about the chosen sampling and the periodicity (or the finiteness) of the lattice. In fact, the eigen-functions of G_0^{-1} and the transformations used to process such digitised signals are *exactly* the same. It is, thus, natural to believe that JJAs are like the discrete versions of a continuum case. Sampling strategies are thus inherently connected to the development of fast algorithms in such arrays.

The above discussion shows that a triangular lattice of Josephson junctions admits both rectangular and hexagonal periodicity. Accordingly, we discuss each type of periodicity and develop fast algorithms for each in turn.

3.3.1 Fast Algorithms for Rectangularly Periodic Lattice

A convenient choice of coordinate system for a rectangularly periodic triangular array is shown in Fig. 3.2. The eigenfunctions in this case can be taken to be $\propto \exp(i\vec{k} \cdot \vec{x})$ where $\vec{k} = k_1 \hat{e}_1 + k_2 \hat{e}_2$ and $\vec{r} = x_1 \hat{e}_1 + x_2 \hat{e}_2$ with $\hat{e}_1 \cdot \hat{e}_2 = -1/2$. The action of G_0^{-1} on these eigenfunctions is best described in terms of $\kappa_1 = k_1 + k_2/2$ and $\kappa_2 = k_2 + k_1/2$. Indeed,

$$\langle \vec{x} | G_0^{-1} | \vec{x}' \rangle = (6\delta_{\vec{x}, \vec{x}'} - \delta_{\vec{x}, \vec{x}' \pm \hat{e}_1} - \delta_{\vec{x}, \vec{x}' \pm \hat{e}_2} - \delta_{\vec{x}, \vec{x}' \pm (\hat{e}_2 - \hat{e}_1)}) \quad (3.17)$$

whence

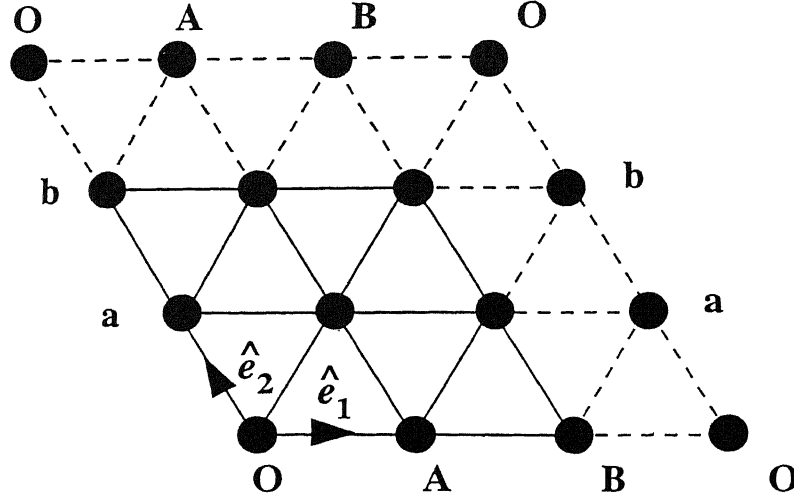


Figure 3.2: A triangular lattice with $L_1 = L_2 = 3$ showing rectangular periodicity. Equivalent points on the edges are marked with same labels.

$$\begin{aligned}
 \langle \vec{x} | G_0^{-1} | \vec{k} \rangle &= \sum_{\vec{x}'} \langle \vec{x} | G_0^{-1} | \vec{x}' \rangle \langle \vec{x}' | \vec{k} \rangle \\
 &= \sum_{\vec{x}'} \langle \vec{x} | G_0^{-1} | \vec{x}' \rangle \exp i \vec{k} \cdot \vec{x}' \\
 &= [6 - 2 \cos \kappa_1 - 2 \cos \kappa_2 - 2 \cos(\kappa_1 - \kappa_2)] \exp i(\kappa_1 x_1 + \kappa_2 x_2) \\
 &= \lambda_{\kappa_1, \kappa_2} \langle \vec{x} | \vec{k} \rangle
 \end{aligned} \tag{3.18}$$

It is noteworthy that $\lambda_{\kappa_1, \kappa_2}$ has all the 12 symmetries of the hexagonal group:

$$\begin{aligned}
 \lambda_{\kappa_1, \kappa_2} &= \lambda_{-\kappa_1, -\kappa_2} = \lambda_{\pm \kappa_1, \pm(\kappa_1 - \kappa_2)} = \lambda_{\mp(\kappa_1 - \kappa_2), \pm \kappa_2} \\
 &= \lambda_{\mp \kappa_2, \pm(\kappa_1 - \kappa_2)} = \lambda_{\pm \kappa_2, \pm \kappa_1} = \lambda_{\pm(\kappa_1 - \kappa_2), \pm \kappa_1}
 \end{aligned} \tag{3.19}$$

Due to rectangular periodicity (Eq.(3.15)), the wavevectors have to satisfy the quantisation conditions $\kappa_i = (2n_i\pi)/L_i$, $i = 1, 2$ with $n_i = 0, 1, \dots, L_i - 1$ and the Green's function for the rectangularly periodic triangular lattice reads, accordingly,

$$\tilde{G}(\vec{x}, \vec{x}') = \frac{4}{L_1 L_2} \sum_{\vec{\kappa} \neq 0} \frac{\exp i [\kappa_1(x_1 - x'_1) + \kappa_2(x_2 - x'_2)]}{6 - 2 \cos \kappa_1 - 2 \cos \kappa_2 - 2 \cos(\kappa_1 - \kappa_2)} \tag{3.20}$$

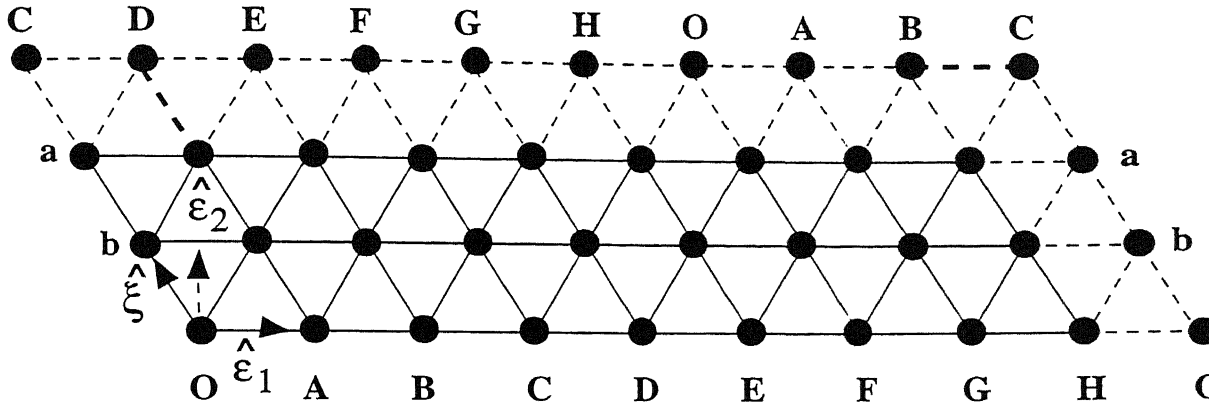


Figure 3.3: A triangular lattice with $L = 3$ showing hexagonal periodicity. Equivalent points on the edges are marked with same labels.

This is the same as the Green's function of a periodic square lattice with only the eigenvalues changed. Thus a knowledge of the $\mathcal{O}(N \ln N)$ algorithm for the square case immediately provides a fast algorithm for this configuration, as well.

3.3.2 Fast Algorithms for Hexagonally Periodic Lattice

The eigenfunctions of G_0^{-1} for this case can, once again, be written as $\exp(i\vec{k} \cdot \vec{x})$, provided we set $\vec{k} = k_1\hat{e}_1 + k_2\hat{e}_2$ and $\vec{x} = x_2\hat{\xi} + x_1\hat{e}_1$ with $\hat{e}_i \cdot \hat{e}_j = \delta_{ij}$ and $\hat{\xi} = \frac{\sqrt{3}}{2}\hat{e}_1 - \frac{1}{2}\hat{e}_2$ (see Fig. 3.3). In terms of $\kappa_1 = \frac{\sqrt{3}}{2}k_1$, $\kappa_2 = \frac{1}{2}k_2$, these functions, on being normalized, take the form

$$\langle \vec{x} | \vec{k} \rangle = \frac{1}{\sqrt{L_2(2L_1 + L_2)}} \exp i \{ \kappa_1(2x_1 - x_2) + \kappa_2 x_2 \} \quad (3.21)$$

It is easily verified that the action of G_0^{-1} on $\langle \vec{x} | \vec{k} \rangle$ yields

$$\begin{aligned} \langle \vec{x} | G_0^{-1} | \vec{k} \rangle &= \sum_{\vec{x}'} \langle \vec{x} | G_0^{-1} | \vec{x}' \rangle \langle \vec{x}' | \vec{k} \rangle \\ &= N \left[6\delta_{x_1, x_1'} \delta_{x_2, x_2'} - \delta_{x_1 \pm 1, x_1'} \delta_{x_2, x_2'} - \delta_{x_1 \pm 1, x_1'} \delta_{x_2 \pm 1, x_2'} - \delta_{x_1, x_1'} \delta_{x_2 \pm 1, x_2'} \right] \\ &\quad \exp i \{ \kappa_1(2x_1 - x_2) + \kappa_2 x_2 \} \\ &= N [6 - 2 \cos(\kappa_1 + \kappa_2) - 2 \cos(\kappa_1 - \kappa_2) - 2 \cos(2\kappa_1)] \end{aligned} \quad (3.22)$$

$$\begin{aligned} & \exp i\{\kappa_1(2x_1 - x_2) + \kappa_2 x_2\} \\ & = \lambda_{\kappa_1, \kappa_2} N \exp i\{\kappa_1(2x_1 - x_2) + \kappa_2 x_2\} \end{aligned}$$

where $N = [L_2(2L_1 + L_2)]^{-1/2}$ is the appropriate normalization constant. The eigenvalues $\lambda_{\kappa_1, \kappa_2}$ are 12-fold degenerate and the corresponding eigenfunctions are easily checked to be

$$\begin{aligned} & \exp i\{\pm\kappa_1(2x_1 - x_2) + \kappa_2 x_2\}, \exp i\{\pm\kappa_1(x_1 + x_2) + \kappa_2(x_1 - x_2)\}, \\ & \exp i\{\pm\kappa_1(x_1 - 2x_2) + \kappa_2 x_2\} \end{aligned} \quad (3.23)$$

and their complex conjugates.

All these wavefunctions can be made to respect the hexagonal periodicity of the lattice by simply quantising κ_i . The quantised values of the momenta, for the case $L_1 = L_2 = L$, are

$$\kappa_1 = (2n_1 - n_2) \frac{\pi}{3L} \quad \text{and} \quad \kappa_2 = \frac{n_2 \pi}{L} \quad (3.24)$$

where n_1 and n_2 are integers, $0 \leq n_1 < 3L$, $0 \leq n_2 < L$.

With this in hand, we can write down the Green's function for the hexagonally periodic triangular lattice as

$$\begin{aligned} \tilde{G}(x_1, x_2 | x'_1, x'_2) &= \frac{1}{3L^2} \sum_{\substack{n_1=0, n_2=0 \\ n_1, n_2 \neq 0}}^{3L-1, L-1} \frac{1}{\lambda_{n_1, n_2}} \exp -i \left[\frac{\pi}{3L} (2x_1 - x_2)(2n_1 - n_2) + \frac{\pi}{L} x_2 n_2 \right] \\ & \quad \exp i \left[\frac{\pi}{3L} (2x'_1 - x'_2)(2n_1 - n_2) + \frac{\pi}{L} x'_2 n_2 \right] \end{aligned} \quad (3.25)$$

with

$$\lambda_{n_1, n_2} = \left(6 - 2 \cos(2n_1 - n_2) \frac{2\pi}{3L} - 2 \cos(2n_2 - n_1) \frac{2\pi}{3L} - 2 \cos(n_1 + n_2) \frac{2\pi}{3L} \right)$$

It has been shown by Mersereau that one can move back and forth between the \vec{x} -basis and the \vec{k} -basis defined above in $\mathcal{O}(N \ln N)$ steps by the forward and backward Hexagonally Discrete Fourier Transforms (HDFT) when $L = 2^m$. This is done by noting that the forward transform of $d(x_1, x_2)$ is a sum

$$d(n_1, n_2) = \sum_{x_1=0}^{3L-1} \sum_{x_2=0}^{L-1} d(x_1, x_2) \exp -i \left[\frac{\pi}{3L} (2x_1 - x_2)(2n_1 - n_2) + \frac{\pi}{L} x_2 n_2 \right]$$

can be divided into four smaller sums

$$d(n_1, n_2) = S_{oo}(x_1, x_2) + S_{ee}(x_1, x_2) + S_{oe}(x_1, x_2) + S_{eo}(x_1, x_2) \quad (3.26)$$

Here the symbols $S_{oo}(x_1, x_2)$ etc. signify that both x_1 and x_2 go over odd values (in $S_{oe}(x_1, x_2)$, x_1 goes over odd values while x_2 goes over even values). Using the notation $d(n_1, n_2) = \text{HDFT}_N[d(x_1, x_2)]$ one then immediately gets

$$\begin{aligned} S_{ee}(n_1, n_2) &= \text{HDFT}_{N/2} d(2r_1, 2r_2) \\ S_{eo}(n_1, n_2) &= \exp -i \frac{2\pi}{3L} (n_1 - 2n_2) \text{HDFT}_{N/2} d(2r_1, 2r_2 + 1) \\ S_{oe}(n_1, n_2) &= \exp -i \frac{2\pi}{3L} (2n_1 - n_2) \text{HDFT}_{N/2} d(2r_1 + 1, 2r_2) \\ S_{oo}(n_1, n_2) &= \exp -i \frac{2\pi}{3L} (n_1 + n_2) \text{HDFT}_{N/2} d(2r_1 + 1, 2r_2 + 1) \end{aligned} \quad (3.27)$$

Knowing the outputs S_i , $i = (ee), (oo), (eo), (oe)$, one can immediately get $d(n_1, n_2)$ as

$$\begin{aligned} d(n_1, n_2) &= S_{ee} + W_{3L}^{2n_2 - n_1} S_{eo} + W_{3L}^{2n_1 - n_2} S_{oe} + W_{3L}^{n_1 + n_2} S_{oo} \\ d(n_1 + \frac{3L}{2}, n_2) &= S_{ee} + W_{3L}^{2n_2 - n_1} S_{eo} + W_{3L}^{2n_1 - n_2} S_{oe} + W_{3L}^{n_1 + n_2} S_{oo} \\ d(n_1 + L, n_2 + \frac{L}{2}) &= S_{ee} + W_{3L}^{2n_2 - n_1} S_{eo} + W_{3L}^{2n_1 - n_2} S_{oe} + W_{3L}^{n_1 + n_2} S_{oo} \\ d(n_1 + \frac{5L}{2}, n_2 + \frac{L}{2}) &= S_{ee} + W_{3L}^{2n_2 - n_1} S_{eo} + W_{3L}^{2n_1 - n_2} S_{oe} + W_{3L}^{n_1 + n_2} S_{oo} \end{aligned} \quad (3.28)$$

where $W_k^n = \exp[-(2\pi i n)/k]$. The calculation is summarized in the flowchart of Fig. 3.4. We mention in passing that $\langle \vec{x} | d \rangle$'s being real leads to a further saving in computational time over what has been described by Mersereau.

3.4 Finite Triangular Lattice

We now show how boundaries can be introduced *without* losing the asymptotically linear nature of our algorithms. The finite array can be driven by currents injected or extracted through the open edges. To keep things as simple as possible, we discuss a

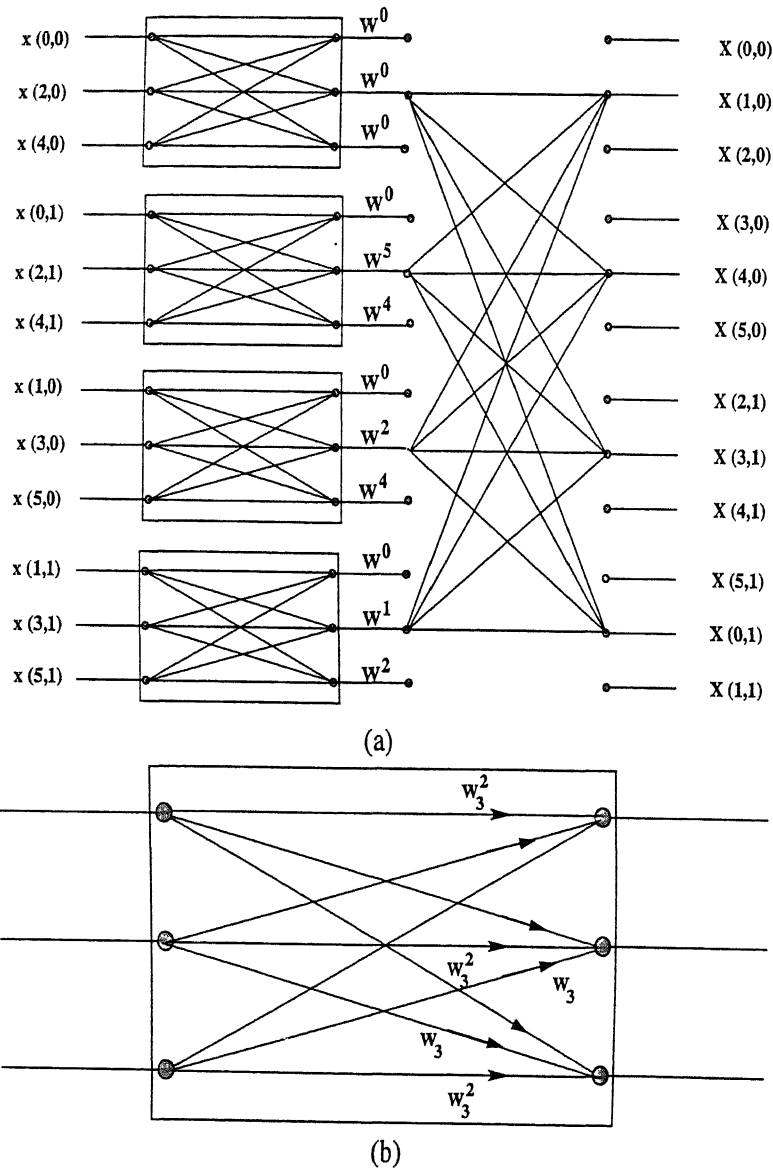


Figure 3.4: The flow diagram for the case of a $L = 2$ hexagonal FFT. One of the 3-point “butterflies” in (a) is shown explicitly in (b).

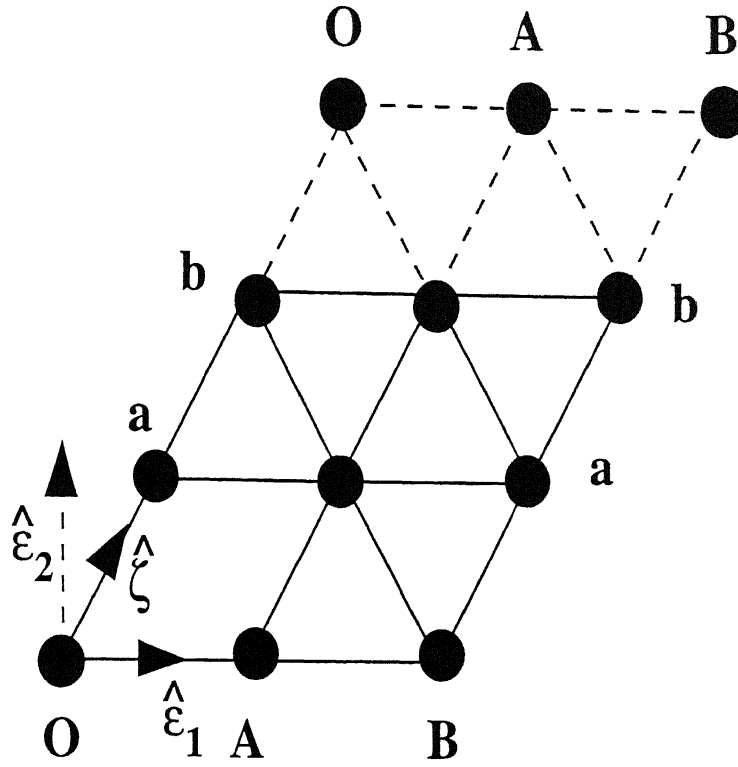


Figure 3.5: A triangular array with $L_1 = L_2 = 3$ which is finite in the \hat{e}_1 direction.

lattice which is periodic in the y - direction and open in the x - direction (see Fig. 3.5). Square arrays with such boundary conditions have been repeatedly used by many authors in numerical studies[77, 109].

We can conveniently study the G_0^{-1} operator for this configuration by separating it into two parts, namely,

$$G_0^{-1} = P - B \quad (3.29)$$

where P is the rectangularly periodic operator for the triangular lattice given by Eq.(3.17) and B is the boundary operator defined by

$$\begin{aligned} \langle \vec{x}' | B | \vec{x} \rangle = & \delta_{x_1, x_0} [2\delta_{\vec{x}, \vec{x}'} - \delta_{x_1-1, x_1'} \delta_{x_2, x_2'} \delta_{x_1-1, x_1'} \delta_{x_2+1, x_2'}] + \\ & \delta_{x_1, x_0+L_1-1} [2\delta_{\vec{x}, \vec{x}'} - \delta_{x_1+1, x_1'} \delta_{x_2, x_2'} \delta_{x_1+1, x_1'} \delta_{x_2-1, x_2'}] \end{aligned} \quad (3.30)$$

One can easily check that B deletes all the bonds required to introduce boundaries along $x = x_0$ and $x = x_0 + L_1 - 1$.

We examine next the \vec{k} basis defined by

$$\langle \vec{x} | \vec{k} \rangle \propto \cos \kappa_1 x_1 \cos \kappa_2 (2x_2 + x_1) \quad (3.31)$$

where $\vec{k} = k_1 \hat{e}_1 + k_2 \hat{e}_2$, and $\kappa_1 = \frac{\sqrt{3}}{2} k_1$, $\kappa_2 = \frac{1}{2} k_2$, as in Sec.(3.3.2). However, in this case $\vec{x} = x_2 \hat{\zeta} + x_1 \hat{e}_1$ with $\hat{e}_i \cdot \hat{e}_j = \delta_{ij}$ and $\hat{\zeta} = \frac{\sqrt{3}}{2} \hat{e}_1 + \frac{1}{2} \hat{e}_2$.

To motivate this choice, we note that the wavefunctions on the r. h. s. of this equation can be constructed as linear combinations of the degenerate hexagonally periodic wavefunctions listed in Sec.(3.3.2) and can further be made to satisfy at least in part, the appropriate boundary conditions for our configuration (see below). The \vec{k} -basis is, moreover, accessible from $\{|\vec{x}\rangle\}$ through a fast transform.

The normalisations on the eigenfunctions are easily determined to be

$$\langle \vec{k} | \vec{k}' \rangle = \langle k_1, k_2 | k'_1, k'_2 \rangle = \begin{cases} L_1 L_2 & \text{if } \vec{k} = \vec{k}' = 0 \\ \frac{L_1 L_2}{2} & \text{if } k_i = k'_i = 0; i = 1 \text{ or } 2 \\ \frac{L_1 L_2}{4} & \text{if } k_i = k'_i \neq 0; i = 1, 2 \end{cases} \quad (3.32)$$

We shall, however, work with the unnormalized eigenfunctions and normalize them at the appropriate junctures.

For these functions to be periodic under $x_2 \rightarrow x_2 + L_2$ as required by the geometry of our configuration, we must have $\kappa_2 = (m_2 \pi)/L_2$, $m_2 = 0, 1, \dots, L_2 - 1$ but can choose x_2 arbitrarily. We shall for convenience work with $x_2 = 0, 1, \dots, L_2 - 1$.

As before, we can show that the operator P is diagonal in the \vec{k} basis. Indeed,

$$\begin{aligned} \langle \vec{k} | P | \vec{k}' \rangle &= \sum_{\vec{x}', \vec{x}} \langle \vec{k} | \vec{x} \rangle \langle \vec{x} | P | \vec{x}' \rangle \langle \vec{x}' | \vec{k}' \rangle \\ &= \sum_{\vec{x}', \vec{x}} \langle \vec{k} | \vec{x} \rangle \left[6\delta_{\vec{x}, \vec{x}'} - \delta_{x_1 \pm 1, x'_1} \delta_{x_2, x'_2} - \delta_{x_1 \pm 1, x'_1} \delta_{x_2 \pm 1, x'_2} - \delta_{x_1, x'_1} \delta_{x_2 \pm 1, x'_2} \right] \\ &\quad \cos \kappa'_1 x'_1 \cos \kappa'_2 (2x'_2 + x'_1) \\ &= \sum_{\vec{x}} \langle \vec{k} | \vec{x} \rangle (6 - 4 \cos \kappa_1 \cos \kappa_2 - 2 \cos \kappa_2) \langle \vec{x} | \vec{k}' \rangle \\ &= \lambda_{\kappa_1, \kappa_2} \langle \vec{k} | \vec{k}' \rangle = \lambda_{\kappa_1, \kappa_2} \delta_{\vec{k}, \vec{k}'} \end{aligned} \quad (3.33)$$

On the other hand, B is only block diagonal, at best. Indeed, $\langle \vec{x}|B|\vec{k}'\rangle$ can be brought close to being proportional to $\langle \vec{x}|\vec{k}'\rangle$ but not quite. More specifically, by choosing $x_0 = 1/2$ and $\kappa'_1 = \pi m'_1/L_1$, $m'_1 = 0, 1, \dots, L_1 - 1$, we get

$$\langle \vec{x}|B|\vec{k}'\rangle = 2(1 - \cos \kappa'_2) [\delta_{x_1, 1/2} + \delta_{x_1, L_1 - 1/2}] \langle \vec{x}|\vec{k}'\rangle \quad (3.34)$$

From this equation it immediately follows that

$$\begin{aligned} \langle \vec{k}|B|\vec{k}'\rangle &= \sum_{\vec{x}} \langle \vec{k}|B|\vec{x}\rangle \langle \vec{x}|\vec{k}'\rangle \\ &= 2(1 - \cos \kappa'_2) \frac{L_2}{2} \left[\cos \frac{\kappa_1}{2} \cos \frac{\kappa'_1}{2} - \cos \frac{\kappa_1(2L_1 - 1)}{2} \cos \frac{\kappa'_1(2L_1 - 1)}{2} \right] \delta_{\kappa_2, \kappa'_2} \\ &= 2(1 - \cos \kappa'_2) [1 + (-1)^{m_1 + m'_1}] \cos \frac{m_1 \pi}{2L_1} \cos \frac{m'_1 \pi}{2L_1} \delta_{\kappa_2, \kappa'_2} \end{aligned} \quad (3.35)$$

where $\kappa_1 = \pi m_1/L_1$ and $\kappa'_1 = \pi m'_1/L_1$. We note that for $\kappa_2 = \kappa'_2 = 0$, the r. h. s. vanishes. Thus in the $\kappa_2 = 0$ sector, G_0^{-1} is diagonal. Furthermore, we note that if $(m_1 + m'_1)$ is odd, the corresponding element of B is zero, signifying that odd and even m_1 values do not mix.

This, in turn, implies that there are two blocks in B corresponding to every non-zero value of κ_2 . One of these, of size $[L_1/2]$ (where $[m]$ is the largest integer contained in m) corresponds to odd m_1 and m'_1 while the other of size $[(L_1 + 1)/2]$ corresponds to even values of m_1 and m'_1 . If we denote these two blocks by $B^{oo}(\kappa_2)$ and $B^{ee}(\kappa_2)$ (for “odd-odd” and “even-even”) respectively, we see that from Eqs.(3.32) and (3.35) that their matrix elements, in terms of *normalized* basis vectors are

$$\frac{\langle \kappa_1 \kappa_2 | B^{oo} | \kappa'_1 \kappa'_2 \rangle}{\langle \kappa_1 \kappa_2 | \kappa'_1 \kappa'_2 \rangle} = \frac{\langle m_1 | B^{oo}(\kappa_2) | m'_1 \rangle}{\langle m_1 | m'_1 \rangle_{\kappa_2}} = \frac{8}{L_1} (1 - \cos \kappa_2) \cos \frac{m_1 \pi}{2L_1} \cos \frac{m'_1 \pi}{2L_1} \quad (3.36)$$

and

$$\langle m'_1 | B^{ee}(\kappa_2) | m_1 \rangle = \frac{8}{L_1} (1 - \cos \kappa_2) (1 - \frac{1}{2} \delta_{m_1, 0}) \cos \frac{m_1 \pi}{2L_1} \cos \frac{m'_1 \pi}{2L_1} \quad (3.37)$$

We point out that since $\langle m_1 = 0 | B^{ee}(\kappa_2) | m_1 \rangle = \frac{1}{2} \langle m_1 | B^{ee}(\kappa_2) | m_1 = 0 \rangle$, $B^{ee}(\kappa_2)$ is not symmetric, while $B^{oo}(\kappa_2)$ clearly is.

It is worth mentioning that the boundary matrix for the finite *square* lattice commutes with the corresponding periodic matrix and hence the two can be simultaneously diagonalized. Even this turns out to be unnecessary, for that case, because we can make B a null operator, satisfying $B|\vec{k}\rangle = 0 \forall \vec{k}$, by choosing $\langle \vec{x}|\vec{k}\rangle$ as in Eq.(3.10) and letting the origin lie on the dual lattice.

Returning to $G_0^{-1} = P - B$, we note that this differs from $-B$ only in its diagonal elements. It follows that G_0^{-1} is diagonal in the $\kappa_2 = 0$ sector and each of the blocks in it corresponding to a given $\kappa_2 = n_2\pi/L_2 \neq 0$ can be written as

$$\begin{bmatrix} \lambda_{m_1, m_2} - pAC_{m_1}C_{m_1} & -pAC_{m_1+2}C_{m_1} & \cdots & -pAC_{m_1+q}C_{m_1} \\ -pAC_{m_1}C_{m_1+2} & \lambda_{m_1+2, m_2} - AC_{m_1+2}C_{m_1+2} & \cdots & \vdots \\ \vdots & \ddots & \cdots & \vdots \\ -pAC_{m_1}C_{m_1+q} & & & \lambda_{m_1+q, m_2} - AC_{m_1+q}C_{m_1+q} \end{bmatrix} \quad (3.38)$$

where λ_{m_1, m_2} is given by substituting values of κ_1 and κ_2 in Eq.(3.33), $p = 1$ (*oo* case), $p = 1/2$ (*ee* case), $A = 8/L_1(1 - \cos \kappa_2)$ and $C_{m_1} = \cos(m_1\pi)/(2L_1)$. The starting value of m_1 is 1 (*oo* case) or 0 (*ee* case) while $m_1 + q = L_1 - 1$ (*oo* case) or L_1 (*ee* case).

Having explicitly determined the forms of P and B in the \vec{k} - basis we can write

$$G_0^{-1} = P - (B^{oo} \oplus B^{ee}) = (G_0^{-1})^{oo} \oplus (G_0^{-1})^{ee} \quad (3.39)$$

Each of these blocks can be individually diagonalized to arrive at the eigenvalues and eigenvectors of G_0^{-1} . The eigenbasis of G_0^{-1} can, unfortunately, not be accessed from the position basis through any known fast transform, and we shall, therefore, continue working in the \vec{k} - basis in preference to carry out these diagonalisations. This is because much as $G_0(\vec{k}, \vec{k}')$ is not diagonal, each block in it can be reduced by simple manipulations of the rows to an effectively tridiagonal matrix, which can be solved for $\langle \vec{k}|\theta\rangle$, in terms of $\langle \vec{k}|d\rangle$, in essentially linear order. Since $\langle \vec{k}|d\rangle = \sum_{\vec{x}} \langle \vec{k}|\vec{x}\rangle \langle \vec{x}|d\rangle$ can be obtained from $\langle \vec{x}|d\rangle$ through a fast transform and $\langle \vec{x}|\theta\rangle = \sum_{\vec{k}} \langle \vec{n}|\vec{k}\rangle \langle \vec{k}|\theta\rangle$ from $\langle \vec{k}|\theta\rangle$ likewise, the entire procedure becomes effectively linear.

Since G^{ee} is diagonal for $\kappa_2 = 0$ one can directly solve for $d(n_1, n_2)$ instead of using the the tridiagonal procedures. Furthermore, in this sector, the restriction of $d(\kappa_1 = 0, \kappa_2 = 0) = 0$, removes the zero mode and implies the usage of the gauge-fixing condition $\sum_i \dot{\theta}_i = 0$.

To see this in explicit detail we recall that in solving

$$G[u] = [v] \quad (3.40)$$

where G is of the form given in Eq.(3.38) for $[u]$ in terms of $[v]$, scalar multiplication and addition are allowed operations on rows but not on columns[128].

Now, from Eq.(3.38), we see that by multiplying the zeroth row by $C_{m_1+2}/(pC_{m_1})$ and subtracting it from the second, we reduce G to

$$\begin{bmatrix} \lambda_{m_1, m_2} C_{m_1+2}/(pC_{m_1}) & -\lambda_{m_1+2, m_2} & 0 & 0 \\ -pAC_{m_1} C_{m_1+2} & \lambda_{m_1+2, m_2} - AC_{m_1+2} C_{m_1+2} & \cdots & \cdots \\ \vdots & \ddots & \cdots & \vdots \\ -pAC_{m_1} C_{m_1+q} & & \lambda_{m_1+q, m_2} - AC_{m_1+q} C_{m_1+q} \end{bmatrix} \quad (3.41)$$

By further multiplying the r^{th} row by C_{m_1+2r+2}/C_{m_1+2r} and subtracting it from the $(r+1)^{th}$ row $r = 1, \dots, q-1$, we turn G into

$$\begin{bmatrix} \lambda_{m_1, m_2} C_{m_1+2}/(pC_{m_1}) & -\lambda_{m_1+2, m_2} & 0 & 0 \\ 0 & \lambda_{m_1+2, m_2} C_{m_1+4}/C_{m_1+2} & -\lambda_{m_1+4, m_2} & 0 \\ \vdots & \ddots & \cdots & \vdots \\ -pAC_{m_1} C_{m_1+q} & & \lambda_{m_1+q, m_2} - AC_{m_1+q} C_{m_1+q} \end{bmatrix} \quad (3.42)$$

i. e. into a matrix which is non-zero only along its diagonal, super-diagonal and last row. A three-band matrix of this form has (i) the same number of elements as tridiagonal matrix and (ii) is amenable to a fast $\mathcal{O}(N)$ solution which is similar to that used in tridiagonal systems. We remark that for a given configuration the numbers $C_{m_1+2r+2}/(pC_{m_1+2r})$ are constants and need be determined once at the outset.

We conclude this section by verifying that for a lattice which is rectangularly periodic in the y -direction, the direct and the inverse transforms are both separable with respect to the arguments concerned. More explicitly,

$$\begin{aligned}
 \langle \vec{k} | \vec{d} \rangle &= \sum_{\vec{x}} \langle \vec{k} | \vec{x} \rangle \langle \vec{x} | \vec{d} \rangle \\
 &= \sum_{\vec{x}} d(x_1, x_2) \cos \frac{m_1 \pi x_1}{L_1} \cos \frac{m_2 \pi (2x_2 + x_1)}{L_2} \\
 &= \sum_{x_1} \cos \frac{m_1 \pi x_1}{L_1} \sum_{x_2} d(x_1, x_2) \left[\cos \frac{2m_2 \pi x_2}{L_2} \cos \frac{m_2 \pi x_1}{L_2} - \sin \frac{2m_2 \pi x_2}{L_2} \sin \frac{m_2 \pi x_1}{L_2} \right]
 \end{aligned} \tag{3.43}$$

where $x_2 = 0, 1, \dots, L_2 - 1$ and $x_1 = 1/2, 3/2, \dots, L_1 - 1/2$. The summation over x_2 can be performed by noting that $\sum_{x_1} d(x_1, x_2) \cos \frac{2m_2 \pi x_2}{L_2}$ and $\sum_{x_1} d(x_1, x_2) \sin \frac{2m_2 \pi x_2}{L_2}$ are the real and imaginary parts of the fourier transform of $d(x_1, x_2)$. This (fast) fourier transform is followed by the multiplication of the real (imaginary) parts by $\cos \frac{m_2 \pi x_1}{L_2}$ ($-\sin \frac{m_2 \pi x_1}{L_2}$) and the addition of the resulting products, to get the function multiplying $\cos \frac{2m_1 \pi x_1}{L_1}$ in Eq.(3.43). Finally, the sum over x_1 can be performed by using the fast cosine transform. The complexity of the whole procedure is then essentially $\mathcal{O}(N \ln N)$. The backward transform i. e.

$$\langle \vec{x} | \theta \rangle = \sum_{\vec{k}} \langle \vec{x} | \vec{k} \rangle \langle \vec{k} | d' \rangle = \sum_{m_1, m_2} d'(\kappa_1, \kappa_2) \cos \frac{m_1 \pi x_1}{L_1} \cos \frac{m_2 \pi (2x_2 + x_1)}{L_2}$$

can likewise be performed with a complexity $\mathcal{O}(N \ln N)$. By contrast, for a lattice with *hexagonal* periodicity in the y -direction, W and \tilde{W} are *not* separable in x_1 and x_2 . They can nevertheless be performed with a complexity $\mathcal{O}(N \ln N)$ using the HDFT procedures outlined in[133].

3.5 Summary and Discussion

To summarize, we have extended to triangular arrays, the fast algorithms, which were so far available only for square geometries. More specifically, we have developed algorithms for periodic triangular lattices and those with one set of parallel edges free.

In treating the former, we have kept track of the fact that a triangular lattice admits rectangular as well as hexagonal periodicity and have shown that the rectangularly periodic case is a relatively straight-forward extension of the square case. On the other hand, the hexagonally periodic situation is quite distinct in that the eigenfunctions of the corresponding discrete laplacian are not separable in x_1 and x_2 . Their eigenbasis can nevertheless, be accessed from the position basis in $\mathcal{O}(N \ln N)$ steps by the Hexagonally Discrete Fourier Transforms. This circumstance has allowed us to take the algorithm through. The finite case is rather more difficult for the triangular lattice than it is for the square. This is because the creation of a boundary in the former, requires the removal of two bonds placed obliquely with respect to each other, rather than one. This case therefore requires a new approach and this has been developed in the paper. In particular we have broken up the inverse laplacian G_0^{-1} into a periodic (P) and a boundary (B) matrix and have shown that for a specific choice of the basis both B and $P - B = G_0^{-1}$ take on forms which are amenable to diagonalisation in linear order. This has allowed us to present for the finite case an algorithm which is asymptotically linear to within constants and factors of $\ln N$. I would be worthy to investigate the case of the fully finite array by removing the y periodicity too.

We should also mention that we have not fully exploited the symmetries of the triangular lattice in this paper. In particular, we still need to investigate the circumstances under which the wavefunctions related by symmetry transformations to the one we have actually used (see Eq.(3.23)) are more convenient.

It is also interesting to note that the approach adopted in this paper has much in common with the one used in Sec. 2.4 to treat missing bond defects in square arrays. There, too, G^{-1} was decomposed into two parts: one (G_0^{-1}) for the perfect finite lattice and the other (h) for the defect: $G^{-1} = G_0^{-1} - h$, with $G_0^{-1} = P - B$ and $[P, B] = 0$. For a linear defect with $n(< N_i)$ broken bonds, $[G_0^{-1}, h] \neq 0$. The form of h , however, makes the problem amenable to a perturbative approach rather than to the tridiagonalisation described in this paper.

Finally we observe that for a hexagonally periodic lattice, equivalent points in different tiles (see Ref.[133]) can be exchanged to create a new fundamental period. These periods therefore come in several shapes of which Fig. 3.1 is but one example. The corresponding eigenvalues and eigenfunctions, however, remain unaltered and the $\mathcal{O}(N \ln N)$ algorithm continues to be equally applicable to each of them. These shapes can serve as starting points for creating several different finite lattices. The various types of boundaries which result are especially significant in view of the interesting question: For which class of boundaries does the matrix B commute with P ? Indeed if there are cases for which $[P, B] = 0$, they will automatically lead to $\mathcal{O}(N \ln N)$ algorithms.

Chapter 4

Defects

4.1 Introduction

Recently the study of the dynamical properties of JJAs, especially in the presence of controlled[76] and random disorder[74, 109], has attracted lots of attention. In accordance with Forrester *et al.*[65], we note that disorder can be introduced into JJAs in three ways: (i) Bond disorder in which the coupling strength of individual junctions is varied, (ii) Positional disorder in which the vector potential entering via an external magnetic field takes on random values, and (iii) Bond dilution in which certain junctions are eliminated altogether. Bond disorder has been studied by Berge[66] to distinguish between the Ising and the Kosterlitz–Thouless (KT) transition temperatures in fully frustrated square lattices and by Chung *et al.*[68] and Li *et al.*[69] who find that disordered arrays have a higher resistance than perfect ones. Positional disorder has, similarly, been investigated in various contexts by a number of authors. Reentrant glassy behaviour in the temperature versus disorder–parameter plot for positionally-disordered arrays has been predicted by Granato *et al.*[73] and investigated experimentally by Benz *et al.*[72]. It has further been found that such arrays lead to the formation of a novel vortex pattern far from equilibrium[74] as also to a plastic-like flow of vortices[110]. Finally, experiments on the critical behaviour of randomly bond-diluted

arrays[75] have revealed that disorder of this type does not destroy the scale invariance of the KT transition. Furthermore, Leath *et al.*[77] have discovered that the transition to resistive behaviour in arrays with missing junctions occurs only when the external current reaches a value for which a vortex path spanning the entire sample becomes possible. This is in contrast to breakdown phenomenon in fuse networks and other linear systems, wherein breakdown emanates from the most critical defect and spreads outwards[131]. They have also found that current-flow past a row of missing bonds in an otherwise perfect array gives rise to voltages on becoming resistive. The behaviour of voltages changes from periodic to quasi-periodic and eventually chaotic, as the vortex “street”, in the corridor containing the defect, spreads to adjacent columns.

In this chapter, we investigate additional effects of bond-disorder and dilution in current driven JJAs. More specifically, we study, through computer simulations, the behaviour of vortices in the superconductive regime, i.e. their nucleation, movement and pinning. We do this for arrays much larger than those studied previously. We find that the time-independent states of uniformly-driven arrays with linear defects, created through bond disorder *or* dilution, fall naturally into various sectors, separated by kink discontinuities in energy. Each sector is characterised by a fixed number of pinned vortices. These pinned vortices produce a hysteresis in the system, which we explore in some detail. Several complementary insights into each of these phenomena are obtained by keeping track of the changes in phase variables caused by modifications in current drive. Studying these changes carefully for the periodic regime, in addition to the superconductive one, accords us a deeper understanding of how the breakdown of superconductive flow actually occurs. We find, for instance, that the periodic flow of vortices is sustained by the absorption of energy present in spin-waves. Finally, we examine current flow past extended defects. We find that in some cases *increased* bond dilution can enhance the i_c of the system, provided the current flow around the extended defect is more streamlined. This effect is analogous to hydrodynamic flows.

The chapter is organised as follows. In Sec. 4.2, we study bond disorder/diluted linear defects, the transitions to various vortex-sectors, and the periodic regime present

in such arrays. In Sec. 4.3, current flow past defects of various shapes is studied to explore streamlining properties in analogy with hydrodynamics. The summary and conclusions are presented in Sec. 4.4.

4.2 Linear Defects

Using the fast algorithms (see Chap. 2), we have numerically studied ¹ large arrays (as big as 128×256 in size) with linear defects of varying sizes. The case of bond disorder can easily be incorporated into such a formalism as it affects only the divergence term in Eq.(2.4) since $i_0 \sin \theta_{jk} \rightarrow g i_0 \sin \theta_{jk}$. We call such bonds as “graded” bonds. A typical geometry is shown in Fig. 4.1. A linear defect, consisting of n broken/graded bonds all parallel to the x -axis, is placed symmetrically along the central column (CC). The current drive, i_{ext} is uniform along the left edge. We have taken advantage of the symmetry, $\theta(x, y) = \theta(x, -y)$, about the y axis to speed up the simulations ². We thus calculate only the $y > 0$ section of the array. A positive vortex located at (x, y) has a negative image vortex located at $(x, -y)$ due to this symmetry. Henceforth, all array and defect sizes refer to the size of the full array and the defect even though the calculations are done only on half the array. The number of vortices and their description, however, pertains only to $y > 0$ section of the array. All currents are scaled in units of i_0 .

4.2.1 Graded Defects

Here we explicitly show that vortices can be pinned inside a linear defect of graded bonds. This pinning in turn increases the i_c of the system signifying a greater stability. We first study the steady-state regime of an array with a linear defect of uniformly graded bonds with grading g . The variation of i_c , the critical current for the breakdown

¹The calculations were done on a Hewlett Packard 9000 series model 735 workstation.

²The symmetry $\theta(x, y) = \theta(-x, y)$ also exists and could be exploited. However, we have found that if the array is driven into the chaotic region, the symmetries about the x - and y - axes are broken. We monitor both $\theta(x, y)$ and $\theta(-x, y)$ to ascertain that the array is not driven chaotic.

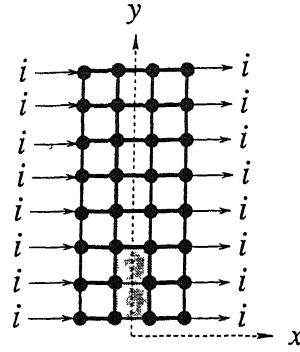


Figure 4.1: Schematic figure of $y > 0$ portion of a 4×16 array with a $n = 4$ defect (shown by a shaded region). Black dots and thick lines joining them symbolize superconducting islands and Josephson junctions, respectively. Narrow lines inside the defect denote graded or broken bonds. Arrows marked i symbolize a current i_{ext} in the direction of the arrow.

of superconductive flow in the array, with g is shown in Fig. 4.2 for a 64×64 array with 20 graded bonds forming a linear defect. The most striking feature of the curve is minimum at $g = g_m$. Intuitively, one would have expected i_c to decrease monotonically with g since a smaller value of g implies a reduced capacity to carry super-current. However, this is clearly not the case. To understand the origin of this minimum, it is useful to examine the behaviour of the phases θ at a number of relevant sites:

For very small values of i_{ext} , the x -bond current in the CC decreases monotonically from a maximum at the center of the defect to $\sim i_{ext}$ at large values of y . In other words, the θ 's along the left edge of the central corridor (LECC) are arranged (see Fig. 4.3(a)) in a monotonically decreasing sequence (while those along the right edge are just their negatives and the phase differences across x -bonds are twice the LECC phase values). As i_{ext} increases, so does each of these phase angles. Eventually, for $i_{ext} = i_1$, the phase, θ_1 at the site $(-1/2, 1/2)$ (see Fig. 4.1) reaches a value of $\pi/4$ and the current $\sin(2\theta_1)$ in the corresponding x bond becomes unity, i.e., it turns critical. As i_{ext} is raised beyond i_1 , the phases simply go on increasing. As a consequence, $2\theta_1$ goes into the second quadrant and the current in the junction begins to fall. Thus, the criticality of a single junction does *not* mark the onset of dissipation, as also noted

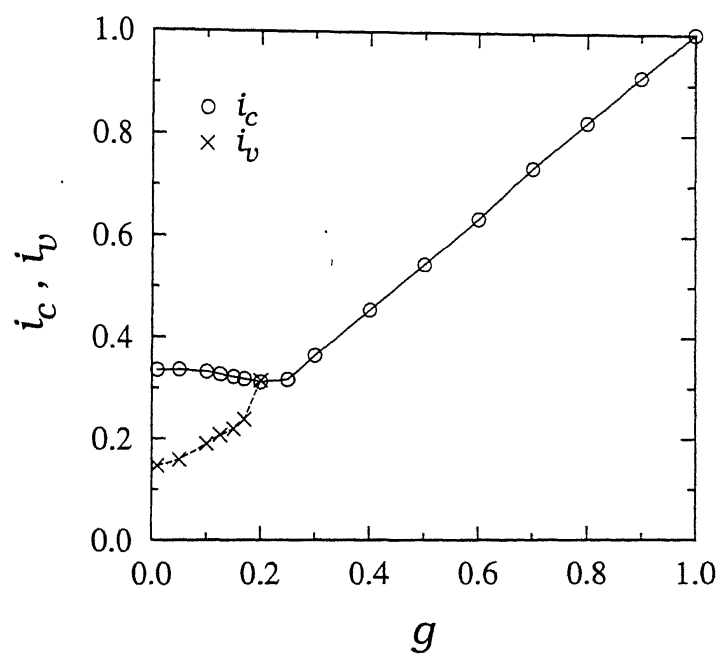


Figure 4.2: A plot of i_c and i_v vs. g showing the minimum in i_c for 64×64 array with a linear defect consisting of 20 graded bonds.

by Leath and Xia[77]. However, in contrast to their observations, this criticality is *not* accompanied by the formation of a vortex. A further increase in i_{ext} causes the next few bonds in the corridor away from the center to successively carry the critical current. This phenomenon persists until i_{ext} reaches a value i_v , θ_1 becomes equal to $\pi/2$ and the current in the junction drops to zero. As soon as i_{ext} exceeds i_v , the current becomes negative and a vortex appears since the next x -bond still carries a positive current and there is a current circulation in the central plaquette located at $(0,1)$. The behaviour of this vortex now depends on whether $g > g_m$ or $g < g_m$. For $0 < g < g_m$, the vortex remains pinned inside the defect (Fig. 4.3(b)) with the pinning center shifting to larger values of y as g increases. Eventually, at $g = g_m$, the pinning occurs just outside the defect at its tip. For $g > g_m$, there is no pinning at all. We notice, however, that the vortex is never pinned at its point of nucleation even as $g \rightarrow 0$.

Finally, for $g < g_m$ but $i_v < i_{ext} < i_c$, the pinned vortex moves outwards, only to get pinned again, always inside, or at most at the edge of the defect. At $i_{ext} = i_c$, the Lorentz force on a vortex at any point along the CC exceeds the pinning force. Consequently, the vortex moves all the way out to the edge of the array and begins to cause dissipation.

The i_v vs. g curve (see Fig. 4.2), on the other hand, does not show any minimum. For $g > g_m$ the i_v and the i_c curves are coincident but separate out for $g < g_m$. We thus infer that grading causes the pinning of vortices which in turn raises the i_c of such systems. This is quite in conformity with the case of continuum superconductors where vortex pinning centers are artificially created (e.g. by ion bombardment[147]) to avoid dissipation. What is surprising, however, is that $g_m \sim 0.2$ is independent of the lattice and defect size provided the latter is small compared to N_y . In the case of $n \sim N_y$ the vortices do not get pinned for *any* value of g due to the presence of edge effects in the array. Consequently, i_c for such an array increases monotonically with g without showing any minimum.

The profile of currents in the x -bonds in the CC, for the case described above, suggest that it is possible to pin several vortices inside the defect for $g < g_m$ provided

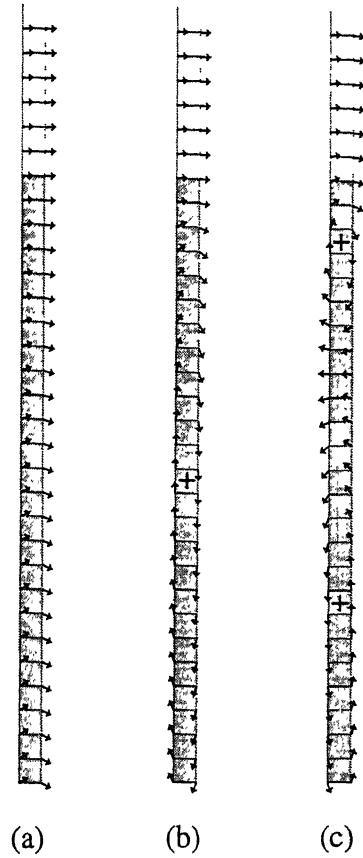


Figure 4.3: Typical configuration of phases in the central corridor of a 32×128 array with a $n = 50, g = 0.1$ graded defect. Only a portion of the corridor is shown. The shaded region is the defect. The vortices are marked with a + sign. For (a) $i_{ext} < i_v$ while for (b) and (c) $i_v < i_{ext} < i_c$. The number of pinned vortices in (a),(b) and (c) are 0, 1 and 2 respectively.

the latter is sufficiently long. In accordance with this expectation, we have found that for a long narrow array 8×128 with $n = 60$ ($g = 0.05$) and for $i_{ext} = 0.064$ we get as many as 3 vortices pinned inside the defect (as in Fig. 4.3(c) which shows the presence of 2 vortices). After the formation and the movement of the first vortex, the magnitude of θ_1 at the center of the array once again passes through the same cycle of events to produce a second vortex which forces the first one outward (the second vortex is formed when $\theta_1 = 3\pi/2$). From a plot of the x bond-current in the CC versus y , one can easily locate the pinned vortices since these are clearly situated wherever a change in sign of the bond-current occurs.

4.2.2 Broken Bonds

We next investigate the behaviour of arrays in the presence of a linear defect produced by bond removal. It had been conjectured[77] that for infinite lattices, the pinning of vortices nucleated by a defect of this type, would occur for defect sizes ~ 200 . With our improved algorithm, we are in a position to check this out.

To begin with, we observe that the sequence of events described in Sec.(4.2.1) is followed for this system as well, with some minor differences: The vortices are now formed at the tip, rather than the center, of the defect and their subsequent behaviour depends on the value of i_v as compared to i_p , the depinning current required to overcome the potential barrier[16] for vortex-motion from one plaquette to another. If $i_v < i_p$, the vortices are pinned by the lattice away from the defect. The transition to the periodic (resistive) state takes place at $i_{ext} = i_c > i_v$. For $i_v > i_p$, the vortices move right across the central corridor, out of the array, and the transition to the periodic state takes place without any vortex-pinning. In this case, i_c coincides with i_v .

We next describe how i_p , i_v , and i_c vary with N_x , N_y , and n . This dependence leads to an understanding not only of the $N_x, N_y \rightarrow \infty$ limit, but also of a number of finite-size effects which are interesting in their own right.

We recall that Lobb *et al.*[16] calculated the potential barrier, E_B for a vortex to move from the center of one plaquette to the adjacent one for *square* arrays assuming

a sinusoidal form for the pinning potential. Their formalism[148] can likewise be used to calculate $i_p = E_B/(2E_J)$ for various values of N_x, N_y , where E_J is the Josephson coupling energy. In carrying this out for vortex motion in the y -direction, we find that for fixed $N_y=32$ and $N_x = 4, 8, 16, 32$, $i_p = 0.147, 0.112, 0.102, 0.099$, respectively. Similarly for $N_x = 32$ and $N_y = 8, 16$, $i_p = 0.072, 0.093$, respectively. We thus see that in rectangular arrays, the finite size effects in the x - and y - directions are different, resulting in a highly anisotropic i_p , which can, for $N_x < N_y$, be larger than the infinite array limit of $i_p^\infty \simeq 0.1$ [148]. This implies that in finite arrays, it should be possible to observe vortex pinning for a defect of size smaller than $\simeq 200$ [77]. This is confirmed by our simulations, e.g., of a narrow 4×256 array with $n = 22$. Here we observe as many as 10 pinned vortices lined up in the central corridor for $i_{ext} = 0.17396$, which incidently is much larger than i_p^∞ .

To isolate the effect of finite array size on i_c , it is expedient to define $\Delta i_c = i_c^\infty - i_c$, where i_c^∞ is the critical current in an infinite array. A log-log plot of $\Delta i_c/i_c^\infty$ vs. N_x/n for a fixed $N_y/n = 32$ is shown in Fig. 4.4. In obtaining this curve, we have taken $i_c^\infty = i_c(N_x = 128)$ for all values of n considered. To convince ourselves that an array with $N_x = 128$ is infinite for all practical purposes, we have checked that i_c varies by less than 0.3% and 0.002% as N_x is changed from 64 to 128 for $n = 8$ and $n = 2$, respectively. From Fig. 4.4, we see that i_c scales in N_x/n and that, furthermore, for $n \simeq 2N_x$, $\Delta i_c/i_c^\infty$ is $\gtrsim 30\%$. This can be understood as follows. The current injected at the left edge of the array must flow around the defect. The smaller the value of N_x , for a given defect size, the larger the curvature of the current flow lines around the defect and hence the larger the vorticity $\partial i_x/\partial y$. Since i_c is related to nucleation of vortices, and this occurs more easily for an enhanced vorticity, i_c diminishes, if N_x is reduced keeping n fixed.

A similar reduction in i_c also occurs with decreasing N_y for a given N_x/n because current redistribution away from the defect gets increasingly constrained. In Fig. 4.4, the error in i_c due to the finiteness of N_y is $\sim 0.01\%$.

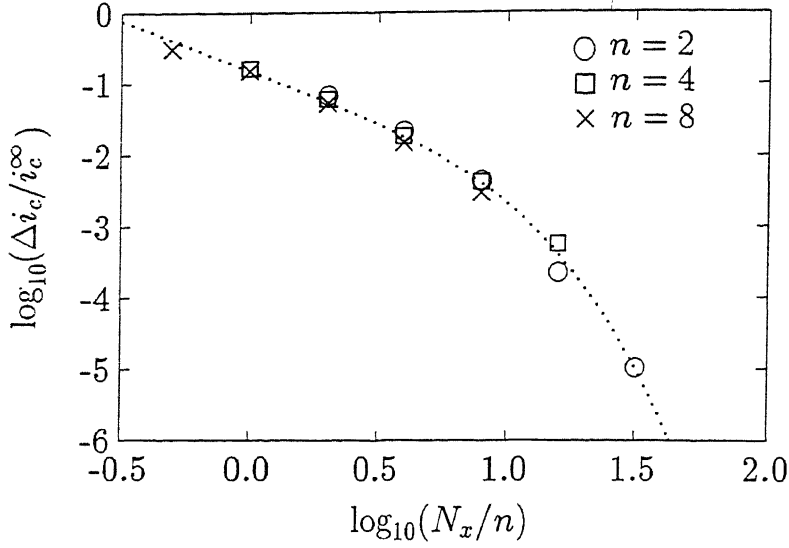


Figure 4.4: A log-log plot of $(\Delta i_c/i_c^\infty)$ vs. (N_x/n) for various n but constant $N_y/n = 32$ showing the scaling behavior.

The effects of a sharp increase in vorticity near the tip of the defect are dramatically exhibited by the formation and flow of vortices *along* rather than perpendicular to the direction of i_{ext} . This is observed for small values of N_x/n for which the current flowing near the tip has a large $\partial i_x/\partial y$ component. This in turn produces large values of both i_y and $\partial i_y/\partial x$. As a result, pairs of vortices (both of the same sign due to symmetry about the y -axis) nucleate at the sides of the tip for $i > i_c$, and flow in opposite directions along the x -axis. This phenomenon can be observed, for example, in an 8×128 array with $n = 48$ and $i_{ext} = 0.15$.

Having shown that in long narrow arrays with moderate-sized defects, i_p goes up and outstrips i_v , while i_c in general comes down, we turn to a detailed study of the vortex-pinning regime ($i_c > i_p > i_{ext} > i_v$). For concreteness, we specialise all our observations to a 16×256 array with 100 missing bonds. We find that the vortex which appears at the tip of the defect for $i_{ext} = i_v$ is always unstable there and moves up the corridor as soon as it forms. However, it gets pinned 15 plaquettes away from the defect and all voltages then quickly drop to zero. The phases along the LECC are

now configured as follows: Those preceding the vortex are all in the second and third quadrants while those following it are in a decreasing sequence lying entirely in the first quadrant. A continuous enhancement in i_{ext} sees each of these angles increasing continuously. Whenever the phase difference across the upper edge of the plaquette containing the vortex becomes π , the current through it changes from being parallel to i_{ext} to being antiparallel and the vortex moves up by one plaquette. Likewise, when $2\theta_{tip}$ reaches the value $(2k + 1)\pi$, $k = 1, 2, \dots$, the k^{th} vortex is nucleated at the tip of the defect. This vortex immediately moves up the corridor pushing the other vortices upward ahead of itself. All the vortices which are thus set into motion eventually get pinned and the transient time-dependence in voltage disappears. The process continues until (for the above-mentioned values of N_x , N_y and n) a maximum of five vortices are pinned by the lattice. Thereafter, for $i_{ext} > i_c$, the vortex street begins to run with a definite periodicity. It is noteworthy that in the periodic domain, the minimum number of vortices simultaneously present in the central corridor either equals or exceeds by one the maximum number pinned in the steady-state regime.

The vortex train formed in the CC is found to be unstable in long narrow arrays at any finite temperature (the rounding off errors in numerical simulations are equivalent to a small but finite temperature). For long narrow arrays (e.g. 4×32), the vortices in the CC are close together, typically 3–4 lattice spacings apart. This is because the image charges across the edges in the narrow dimension screen the vortex charges in the CC. As the position of a given vortex inside its plaquette fluctuates away from the center, $x = 0$, it experiences a destabilising force, due to y —bond currents in this plaquette, produced by the other vortices in the CC. This current is large enough (owing to the proximity of these vortices) to overcome the pinning force in the x —direction. The images of the vortex across the width of the array are also sufficiently close to exert a force which further helps the destabilisation process. The linear chain of the vortices in the CC is thus rendered unstable. This instability is also seen in wider arrays with long linear defects, which create appreciable y —bond currents in the plaquettes along the CC close to the tip of the defect.

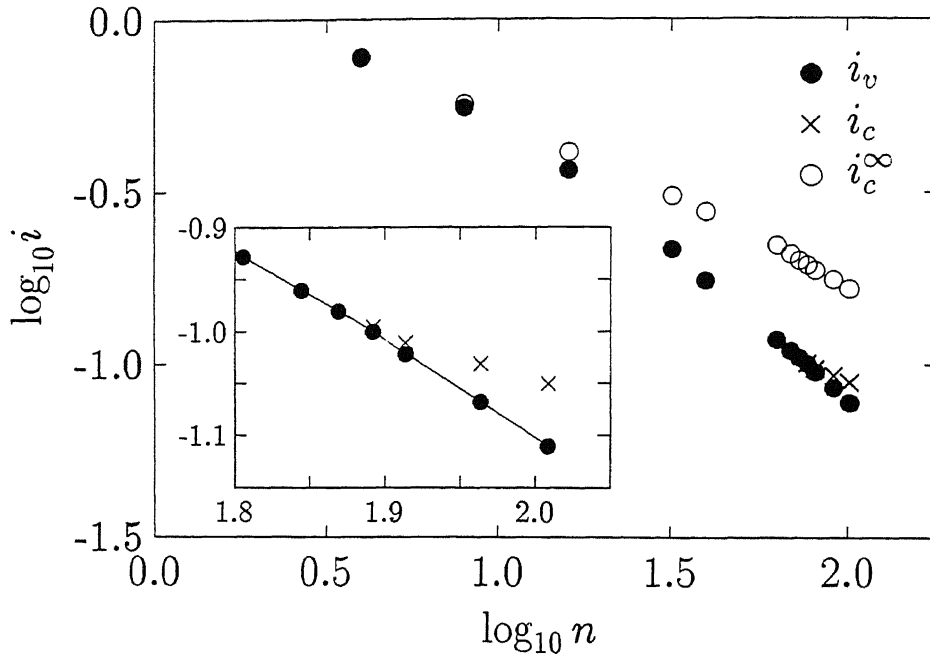


Figure 4.5: A plot of critical currents i_v (\bullet) and i_c (\times) vs. n for a 16×256 array. For $n \simeq 74$, $i_c = i_v$. Also shown are i_c^∞ values (\circ) using corrections for finite N_x from Fig. 3. The inset shows a magnified region where i_v and i_c bifurcate.

Finally in this section, we consider the asymptotic dependence of i_c on the defect size n , particularly in the presence of pinned vortices. Since vortices redistribute the current, increasing its value away from the defect, they could conceivably make the defect effectively larger[77]. On the contrary we find that, as far as i_c is concerned, the effective size of the defect is *reduced* by pinned vortices. We plot i_c vs. n in Fig. 4.5 for a 16×256 array. For $n \lesssim 74$, the vortices cannot be pinned as $i_c(= i_v)$ is larger than i_p , while for $n \gtrsim 74$, they can. Hence, for $n > 74$, we plot both i_v (full circles) and i_c (crosses). It is seen that while the values of i_v follow the curve smoothly across the value $n = 74$, those of i_c bifurcate from and lie above this curve. This increase in i_c relative to i_v shows that the effective size of the defect is reduced by the pinned vortices. The extrapolated values of i_c^∞ using the results of Fig. 4.4 are also shown. Each of these values is larger than $i_p^\infty (\simeq 0.1)$. It follows that defects of size much larger than 74 would be needed to observe pinning in infinite arrays: The estimate of Leath and Xia[77] is in the right ball-park.

4.2.3 Energy Of the System and Hysteresis

The energies of the static configurations forming the steady-state regime of a bond-diluted array acquire, in the presence of pinned vortices, a range of interesting features which we now investigate. As mentioned in Sec.(4.2.2), a vortex which forms at $i_{ext} = i_v$ never stabilises at the point of nucleation (the tip of the defect for the case of broken bonds) and moves a certain distance along the CC before getting pinning. Thus the variation of the phases in the CC (and elsewhere) is discontinuous between i_v^- and i_v^+ . It follows that the energy of the system defined as[62]

$$\frac{E}{E_J} = \sum_{\langle i,j \rangle} [1 - \cos \theta_{ij}] - i_{ext} \sum_{i,j=\frac{N_x+1}{2}} [\theta_{i,-j} - \theta_{i,j}] \quad (4.1)$$

registers a downward discontinuity at the formation and eventual pinning of each new vortex. The energy versus i_{ext} graph (see Fig. 4.6) can thus be conveniently divided into different sectors with the p^{th} sector having p pinned vortices. The energy decreases continuously within a given vortex sector and registers a kink discontinuity only where

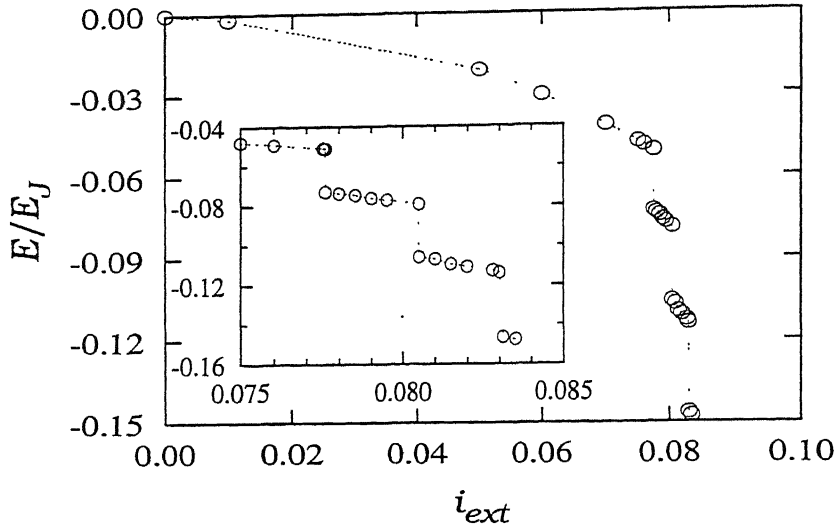


Figure 4.6: The energy of 16×256 array with $n = 100$ the system as a function of $i_{ext} < i_c$. Discontinuities appear at each transition from one vortex sector to the next. The inset shows a magnified transition region.

one enters a higher vortex sector. Moreover, the difference between successive values of i_{ext} , at which these kinks occur, decreases continuously, while the energy discontinuity itself becomes larger and larger.

These observations suggest that for an infinite array (or one which is infinite in the y -direction, at least), there would be an infinite number of vortex sectors. The energy of the system for any of these sectors would be infinite, but the energy *differences* would be finite and well-defined. However, the sequence E_n of energy-gap values would diverge for $n \rightarrow \infty$. On the other hand, the sequence of i_{ext} -values marking transitions from one vortex sector to another would rapidly converge to the depinning current, i_p^∞ , for a single vortex in a perfect array. The spacing between vortices pinned by the lattice would increase with distance from the defect and would become infinite for those furthest out. The vortex-vortex interaction, which inevitably comes into play for finite separation between vortices, would thus become negligible at large distances from the defect[126]. It is because of this that the infinite vortex street would be set into motion only by i_p^∞ .

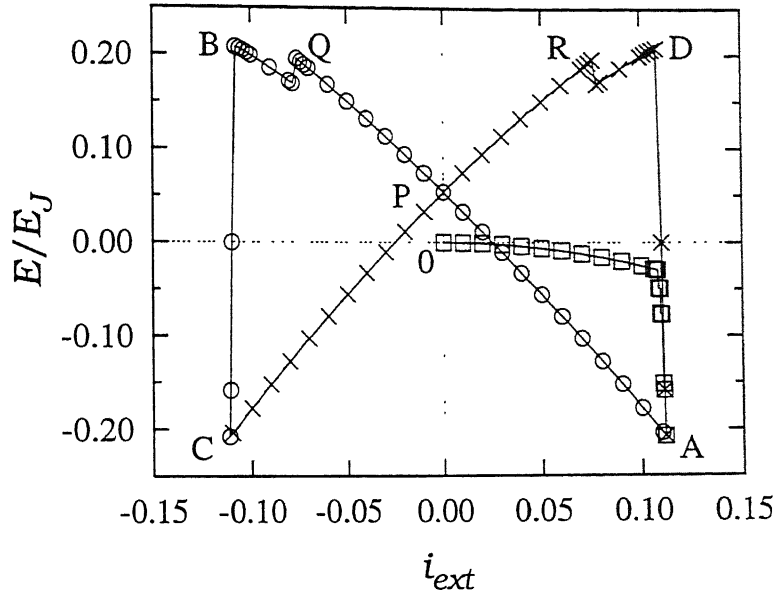


Figure 4.7: The hysteresis loop for a 8×256 array with $n = 50$ for $i_{ext} < i_c$. In this figure the y scale represents energy/bond.

Finally, once vortices have formed and stabilised at various pinning sites in the presence of a certain i_{ext} , they will remain as configured even when this current is reduced to zero. There are consequently at least two configurations of the array at $i_{ext} = 0$ with different values of energy. The actual number is, of course, much larger. In fact there are as many states as there are allowed vortex configurations in the time-independent regime of the given array. The energy is, therefore, multiple-valued in i_{ext} and the i_{ext} - E curve is, in this sense, hysteretic. A typical graph, for an array of size 8×256 with 50 broken bonds, is shown in Fig. 4.7. We note that this graph is symmetric about the E -axis. In plotting it, we first raise i_{ext} from 0 to i_{max} , a current for which there are 5 pinned vortices in the array, and obtain section OA of the hysteresis curve. We next decrement the current from i_{max} through 0 to $-i_{max}$ (curve $APQBC$) and finally raise it back to i_{max} (curve $CPRDA$). The hysteresis loop so obtained is found to be independent of the size of the current-step used in tracing it.

The various features of the closed curve displayed in Fig. 4.7 are understood as follows. A set of 5 vortices forms and stabilises over part OA , as described above. There is no change in the positions of these vortices as the array goes from A to Q . However, the system's energy increases steeply (so much so that at $i_{ext} = 0$, corresponding to point P in Fig. 4.7, the energy is positive). Both circumstances persist until we come close to Q , wherein one of the vortices gets annihilated by the anti-vortex nucleated at the tip of the defect decreasing its energy. Slightly short of this point, anti-vortices steadily begin nucleating at the tip of the defect. Once this happens, the vortices originally present in the CC rapidly disappear through vortex-anti-vortex annihilation and their positions are taken shortly thereafter by anti-vortices. The energy of the array suffers a sharp drop in the process. For $i_{ext} = -i_{max}$, this energy is negative and equal to its value at i_{max} . Since the figure is symmetric about $i_{ext} = 0$, a similar process occurs during the branch $CPRDA$ with the vortices now annihilating the anti-vortices present in the array. Interestingly enough, at our level of resolution in i_{ext} , we did not encounter, at any point of the hysteresis loop, a regime in which there are no vortices present in the array. Finally, it should be pointed out that hysteresis loops of this kind are not uncommon among superconducting systems [149]

4.2.4 The Periodic Regime

In this section we examine the periodic regime of arrays with linear defects and study the mechanism of propagation of vortices in the CC. Once the system enters the time-dependent state (for $i_{ext} > i_c$), vortices nucleate and peel off periodically from the tip of the defect, traverse the entire length of the corridor and pass out of the array[77]. All the phases in the array rotate at the same average angular velocity, ω , where the averaging is done over a time period. The angular velocity is *not constant* since that would imply that the super-current in each link is independent of time.

A snapshot of the phases in an array of size 32×128 is shown in Fig. 4.8. All the phases to the left of the CC rotate anticlockwise while those on the right rotate clockwise. The phases along the columns of the array form "spin waves" moving in the

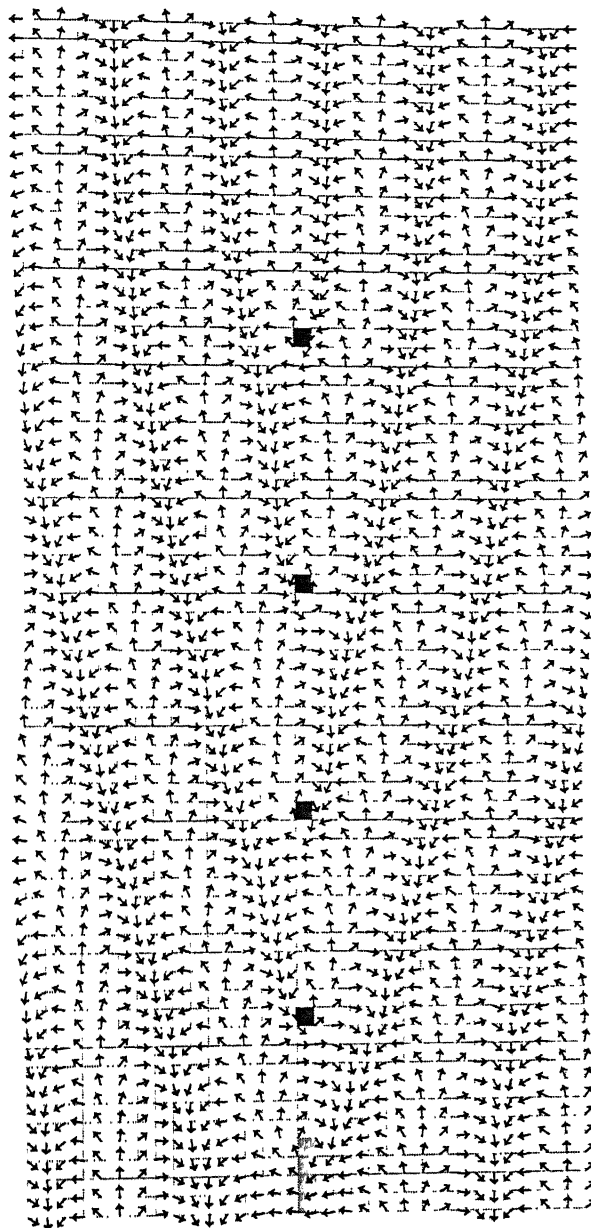


Figure 4.8: A snapshot of an 32×128 with $n = 9$ array in the periodic regime. The arrows represent the phases at the superconducting sites. The defect is the lightly shaded region. The dark shaded plaquettes are occupied by vortices. The wavefronts corresponding to the spin waves are seen as dark streaks across the picture and form a wake in front of the vortices. Note that the wake is asymmetric about the y -axis.

positive y -direction, while the phases along the rows constitute spin waves converging onto the CC. The resultant spin waves, therefore, seemingly form a wake, but actually move into the vortex and propel it forward. In Fig. 4.8, the wavefronts corresponding to the spin waves can be seen easily as dark streaks running across the picture. However, these wavefronts are *ahead* of the vortex rather than behind it. The situation is akin to a time reversed motion of a boat moving in water. Whereas the boat provides the energy to propel itself forward while transferring some of it to the waves in the wake, here the vortex absorbs energy to move forward from the spin waves present in the JJA. The “wake” here is asymmetric along the x -direction as the vortex has the special property of changing the phase by π across the plaquette containing it.

The nature of the waves discussed here is different from those in arrays with capacitive junctions[53, 136]. In such arrays, a vortex moving across a plaquette induces voltages on the superconducting islands, which keep oscillating due to stored capacitive energy long after the vortex has moved away. Thus, vortices (having a finite mass in capacitive arrays) can interact with each other through these spin waves. In overdamped arrays, the vortices just “ride” the spin waves described in this paper. In capacitive arrays, we observe that the inertial oscillations are superimposed upon the waves that the vortices ride.

The separation between successive vortices along the CC is $\lambda/2$, where λ is the wavelength for spin waves in that direction. The frequency ω is roughly proportional to $1/\lambda$ showing a linear dispersion. The value of λ is, however, affected by edges. It increases monotonically as one moves towards the boundary. This is because the frequency of the periodic regime is constant at ω (for a given i_{ext}) while the speed of vortices is higher near the edges due to attraction from the image charges across the latter.

In the x -direction, the phases wind with a finite wavelength even in the steady state regime. This static configuration corresponds to a wavelength which decreases monotonically with an increase in i_{ext} . As i_{ext} crosses i_c , this “frozen” spin wave starts moving. Consequently, at $i_{ext} = i_c$, $\omega = 0$, but the wavelength in the x -direction is

finite. Similarly a finite wavelength along the y -direction would also exist for $\omega = 0$ in the case of sufficiently large arrays where pinned vortices in the CC are present in the steady state regime (and the transition from steady state to periodicity takes place through an n -vortex sector with finite n , as described in Sec. 4.2.3 above).

The angle subtended by the wake at each vortex can be deduced from the ratio of the wavelengths in the y - and x - directions. As expected, this angle decreases as the vortices move faster under an increase in i_{ext} .

4.3 Extended Defects

We now turn to more complicated defect-patterns with a view to determining the dependence of i_c on defect-shape and size and distribution. In doing this, we shall find it useful to keep in mind the analogies, brought out by Mehrotra and Shenoy[78, 79], between current flow in JJAs and hydrodynamic flow through a pipe. These authors consider non-uniformly driven JJAs at zero-temperature. They find that the linear gradient of the external current drive, $\partial i_x / \partial y$ is a measure of injected vorticity which, multiplied by the y -dimension of the array (pipe diameter), and scaled by the inverse shunt resistance gives the analog of the Reynold's number. They further note that the chaotic behaviour observed above a certain injected-vorticity threshold is, as in turbulent fluid flows, due to a mixing of positive and negative vortices. In the spirit of this analogy, we now liken current flows past bond diluted/disordered linear defects to fluid flows past obstacles. Such current flows are closely related to those explored in Ref.[79] because the defect automatically creates a non-zero current gradient, $(\partial i_x) / (\partial y)$. We examine effects of streamlining and find that similarities with fluid flow continue to exist.

We study the bond diluted case by grading defective bonds with a $g \rightarrow 0$ (we use $g = 10^{-7}$, in actual practice) rather than by eliminating them. This permits the use of faster algorithms and makes no difference to the i_c values we are interested in. Indeed,

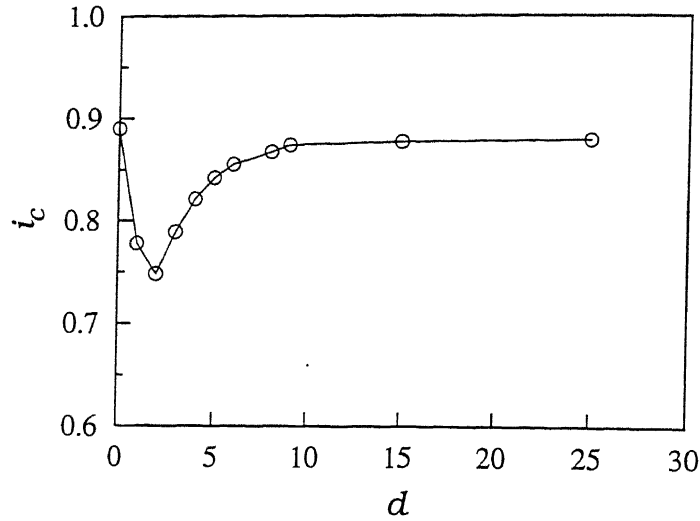


Figure 4.9: The critical current i_c vs. the separation d between defects.

only supercurrents flow through the bonds in the time independent state, and even these turn off wherever g is set to zero.

To determine the effect on i_c of the distance between defects, we consider the case of two highly graded bonds ($g = 10^{-7}$), placed in the central column with an inter-defect separation d . A plot of i_c versus d (Fig. 4.9) shows a minimum at $d = 2$. As both defects try to force current away from themselves, a “squeezing” of current into the channel between the two defects occurs resulting in a “breakdown” inside the channel. This is similar to hydrodynamic flow through a narrow passage. For $d \lesssim 2$, the channel is too narrow for current to flow through and the two defects are seen as just one large defect. This causes an initial decrease in i_c . For $d \gtrsim 2$, the current starts flowing through the channel. For large values of d , the two defects become independent of each other and i_c approaches its value for a single defect.

In studying the effects of streamlining, we use the following notation to denote defect configurations. A sequence of numbers $a, m-b, c, m-b, a$ corresponds to a defect placed at the center of the array, with c graded x -bonds in the central corridor, m -columns of b graded x -bonds each followed by a single column of a graded x -bonds, on either

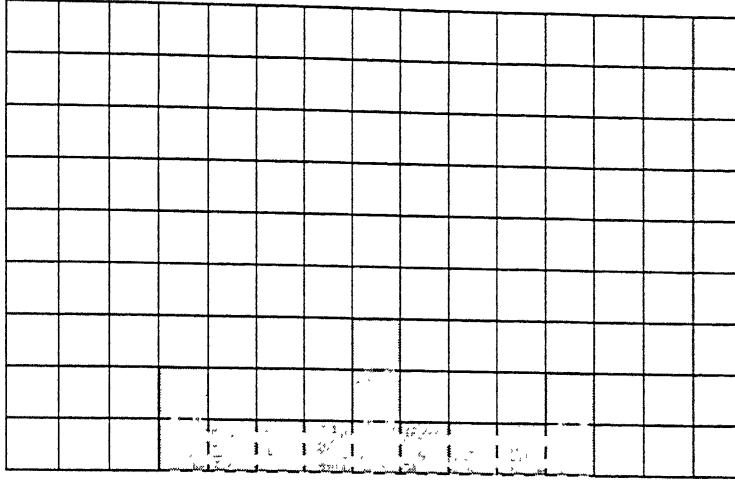


Figure 4.10: Schematic figure of the $y > 0$ section an array with a typical defect (shaded) labeled $2, 3 - 1, 3, 3 - 1, 2$ used to study streamlining. Each side of dotted squares denotes a Josephson junction. Current is injected/withdrawn from left/right edge. All the junctions inside the shaded region are graded with $g = 10^{-7}$ and are equivalent to broken bonds.

side of the CC. A typical defect configuration $(2, 3 - 1, 3, 3 - 1, 2)$ is shown in the inset of Fig. 4.10.

Our results are shown in Fig. 4.11 where the values of i_c are plotted versus m for two distinct cases. We first consider the $2, m - 0, 3, m - 0, 2$ class of defects which corresponds to placing an 2 defective bonds in front of 3, along the injected current path. For $m = 0$, the i_c value is 0.592, which is 0.025 higher than $i_c^{(3)}$, the value for a single $n = 3$ defect. As m is increased, i_c goes through a maximum at $m = m_{max} = 2$ and then decreases asymptotically to $i_c^{(3)}$. A second class of defects $2, m - 1, 3, m - 1, 2$ shows a similar trend, except that the asymptotic value now corresponds to the value for the $\infty - 1, 3, \infty - 1$ defect (The dotted line actually represents measurements on a $15 - 1, 3, 15 - 1$ defect). It should be noted that while the second class has more defective bonds than the first, the i_c values of the former are *higher* than those of the latter, for all m .

The above results are consistent with hydrodynamic flows and can be understood as follows: Any reduction in the curvature and y -gradient of current density in the

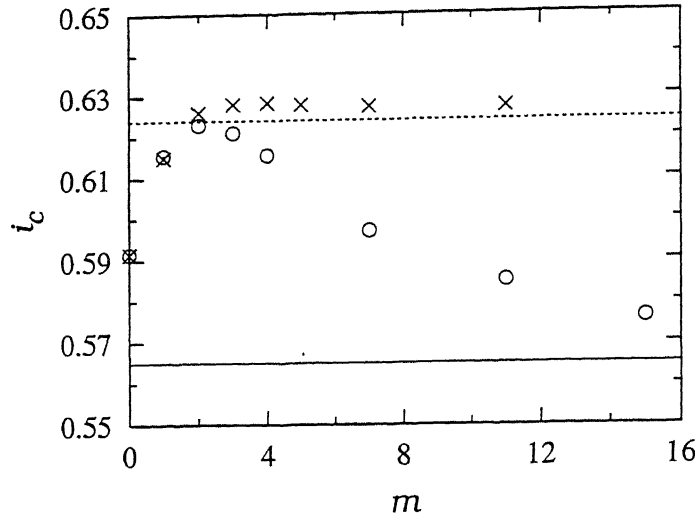


Figure 4.11: The variation of i_c with m used to study streamlining. The circles represent i_c values for defects $2, m-0, 3, m-0, 2$ while crosses are for defect pattern $2, m-1, 3, m-1, 2$. The i_c for single $n=3$ defect is shown by a bold line while the dotted line is for a $15-1, 3, 15-1$ defect.

x -direction ($\partial i_x / \partial y$) increases the value of i_c , as it corresponds to an improved streamlining of the current flow. For example, the i_c value for $m=0$ is higher than $i_c^{(3)}$. Similarly, rectangular defects have higher i_c 's when aligned along the current direction as opposed to being perpendicular[104]. As m increases to m_{max} , i_c increases further because of even better streamlining. The current flow does not sense the small separation between the $n=2$ and $n=3$ defects and does not enter the inter-defect region significantly. For $m > m_{max}$, the current starts penetrating this region and in going around the $n=3$ defect produces a larger value of $\partial i_x / \partial y$. This in turn decreases the values of i_c . For very large values of m , the defects becomes independent and hence i_c asymptotically approaches $i_c^{(3)}$. As the current flow lines cannot bend back into the region between the $n=3$ and $n=2$ defects far enough in the second class of defects, the i_c values are higher than the corresponding ones in the first class, for all m .

4.4 Summary and Conclusions

In conclusion, we have systematically studied JJAs with defects. Using a fast algorithm we have investigated the steady-state regime, the pinning of vortices, the hysteresis present in such arrays and the periodic regime for the case of bond diluted/disordered defects. For bond disordered arrays with linear defects we have shown that for $g < g_m$ vortex pinning increases its stability against breakdown. In the case of bond diluted linear defects, we have shown that (i) i_c scales with N_x/n (for fixed N_y/n), (ii) vortices can be pinned in smaller arrays than thought earlier, (iii) for narrow (small N_x/n) arrays the vorticity at the tip of the defect can increase to a point where vortices form and move along the injected current direction, (iv) the presence of pinned vortices increases the super-current carrying capacity of the array, (v) the energy of these arrays registers a discontinuous drop at each transition from one vortex sector to a higher one, and (vi) these pinned vortices cause hysteresis. An investigation of the periodic regime of such arrays shows the presence of waves which propel the vortices forward. The study of extended defects have shown that an improved streamlining can enhance the i_c of the defects analogous to hydrodynamic flows.

Chapter 5

Ballistic Vortices

The dynamics of vortices in two-dimensional JJAs has been a topic of much current interest both theoretically and experimentally. A large part of this interest has focused on the motion of vortices in JJA and on understanding the physical content of an effective equation of their motion[53, 54, 106, 136, 150]. An exciting possibility to result from these studies is that of vortices moving ballistically in arrays of underdamped junctions[54, 151]. The first experiment which claimed to have observed such ballistic motion in the classical regime was reported by van der Zant *et al.*[3] (hereafter referred to as ZFOM). Computer simulations[56–59, 137], however, failed to observe any ballistic motion in square or triangular arrays. In these simulations a single vortex was accelerated by an applied external current which was subsequently switched off. A ballistic vortex would have continued moving under its own inertia. Several explanations have been put forward to account for the discrepancy.

Eckern *et al.*[53] employed a path-integral approach to arrive at an action which included the quasi-particle tunneling present in capacitive junctions. Separating the field variables into two parts (one of which is due to a single vortex configuration) they obtain an equation of motion of the vortex coordinate in the classical regime. This formulation leads to a finite vortex mass proportional to the inter-junction capacitance of the JJA. Later Eckern *et al.*[136] show that the vortex velocity is strongly affected by the pinning potential of the lattice. As a result they predict that the window for

ballistic motion in a square array is negligibly small. The case of the triangular array is presented as a more promising candidate since the potential barrier was ~ 5 times lower in such arrays.

Bobbert[56], using a piecewise linear potential instead of the sinusoidal pinning potential, found a non-vanishing viscosity for low damping and an energy transfer by the moving vortex to junctions just behind it. He could not find ballistic motion in square and triangular arrays and conjectured that the experiments could be measuring some collective property involving vortex-vortex interactions (VVI) rather than ballistic motion.

Geigenmüller *et al.*[57] probed the extra losses resulting from the generation of charge oscillations by the moving vortex to the spin waves. They found that the friction coefficient η is proportional to $\beta_c^{1/2}$ and was independent of the resistance R for large values of β_c . Using a continuum theory in the presence of a moving vortex (represented by a star-like configuration of the phases) they calculated the vortex velocity as a function of the external current. They concluded that ballistic motion could exist only under very special circumstances: a weak pinning potential (a triangular as opposed to a square array), a driving current just above the depinning threshold i_p , and extremely high values of β_c .

Yu and Stroud *et al.*[58] studied the I - V characteristics of an underdamped array with f near 0 and $1/2$. They found that there exists two critical currents $I_{c1}(f)$ and $I_{c2}(f)$ for JJAs. While the single vortex depinned at the former value, the whole vortex lattice depinned at the latter. The motion of the vortex was non-hysteretic although single junctions were highly underdamped. For high β_c and high vortex velocities row switching occurred instead of ballistic motion. They also confirmed[59] and extended the predictions of Geigenmüller *et al.*[57] to triangular arrays that there is extra damping due to loss of vortex energy to the plasma oscillations.

Fazio *et al.*[60] took the effects of the discrete nature of charges into account theoretically and concluded that the spin wave spectrum is altered so as to reduce the dissipation. Ballistic motion of vortices thus becomes possible for a wider range of

velocities. Recently, Hagenaaers *et al.*[137] numerically studied the enhanced nonlinear viscosity for vortex motion. They found that the viscosity varies as $\eta = A/(1 + Bv^2)$ where A and B are constants and v is the velocity of the vortex. They, however, did not find any ballistic motion and concluded that further theoretical and experimental work was needed to resolve the discrepancy between experiment and theory.

In this chapter, we explicitly demonstrate that a *vortex-street* can move through a field-free region, even for a square array with overdamped junctions. In other words, we show that VVI are large enough to overcome the pinning potential for vortices and cause them to move without any help from an external current drive. Our results thus explain the experimental observations of ZFOM in terms of VVI.

5.1 System Configuration

We recall that the experimental arrangement of ZFOM involves a H shaped array of triangular Josephson junctions. The setup can be divided into three regions :

- (i) The accelerator region where vortices, produced by an applied magnetic field, are accelerated by an external current i_{ext} .
- (ii) These vortices are collimated by a narrow channel and
- (iii) A field-free detector region to detect the collimated vortices at the far end of the accelerator.

Voltage probes at various points detect the movement of the vortex through the array.

We have simplified the ZFOM geometry to the one shown in Fig. 5.1. A linear defect, consisting of n broken bonds parallel to the x -axis, is placed in the central column (CC) at the bottom edge of an $N_x \times N_y$ square array. Most of our work is on two sample arrays, A and B , 16×64 and 32×128 in size with $n = 15$ and 30 , respectively. In sample $A(B)$ a d.c. drive i_{ext} is applied to rows 1–25 (1–45) and is linearly decreased to zero between rows 25–35 (45–55) to avoid large gradients of current in the y -direction which would cause movement of vortices in the x -direction

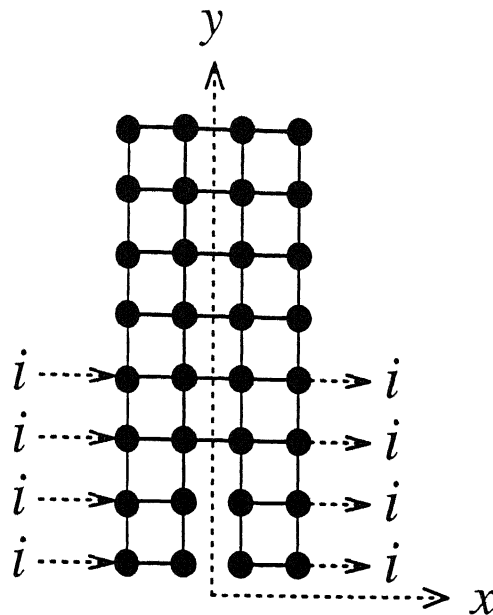


Figure 5.1: A schematic of a 4×8 array with a $n = 2$ defect. Black dots and lines joining them symbolize superconducting islands and Josephson junctions, respectively. Arrows marked i symbolize a current i_{ext} in the direction of the arrow.

as described in Chap. 4. We do not require a channel to collimate the vortices as these nucleate at the tip of the defect and automatically move exclusively along the CC[76, 77], for the range of currents used. The bus bars used by ZFOM to provide a parabolic potential for confining vortices near the CC are likewise not needed and we consequently use free boundary conditions. Moreover, by placing the defect at the bottom edge, vortices of a particular sign are created as in the ZFOM geometry. Finally, for sample $A(B)$, the rows $> 41(72)$ are essentially field-free and correspond to the detector region. The current flowing across the CC x -bonds falls to $0.1i_{ext}$ at rows 41(72) and to $0.01i_{ext}$ at rows 52(95), as measured in the absence of vortices.

We emphasize that the arrangement used by us is very convenient to study the issue at hand since it automatically produces a collimated vortex beam. The geometry is also easily realizable experimentally.

5.2 Numerical Simulation

We have numerically studied the above-mentioned configuration using the standard classical RCSJ model for $0 \leq \beta_c \leq 100$ and temperature $0 \leq T \leq 0.01 E_J$ (introduced via a Langevin noise term), where E_J is the Josephson coupling energy. We scale all currents by i_0 , the single junction critical current, and set the lattice constant $a = 1$. Time is measured in units of $\omega_c^{-1} = \hbar/(2eRi_0)$, the inverse characteristic Josephson frequency or $\omega_p^{-1} = \sqrt{\beta_c} \omega_c^{-1}$, the inverse plasma frequency. We use a fast cosine transform algorithm extended to arrays with missing bonds as discussed in Chap. 2.

For $0.25 \lesssim i_{ext} \lesssim 0.4$, which is large enough to nucleate vortices at the defect but insufficient to cause column switching, we observe that a vortex nucleated at the tip of the defect and accelerated by i_{ext} moves up the CC, where it gets pinned in the field-depleted region. When another vortex is nucleated, the first vortex is pushed forward and both vortices move until each one gets pinned in the CC. This process continues until in the s -vortex sector (see Chap. 4) (s is between 7 and 8 for array A), the vortex farthest from the defect is pushed out of the array. At this stage the vortex-street begins to run and vortices flow out of the array periodically now moving all the way across the field-free region to the far end of the array for *all* the above values of β_c .

To make direct contact with the experiment of ZFOM, we measure in array A the voltage between the current driven edges of the array, averaged both along the edges from rows 1–39 and in time. This corresponds to the voltage V_a in the accelerator region of ZFOM. Similarly, the average voltages V_{ch} and V_d , from rows 40–41 and rows 42–64, correspond to the channel and the detector regions, respectively. We also monitor the voltage V_e across the bond in the CC at the far end where the vortices leave the array. In Fig. 5.2, we plot each of these voltages as functions of i_{ext} at two values of T with $\beta_c = 10$. For $T = 0.003$, all voltages are equal (V_{ch} not shown for clarity) showing that all the vortices nucleated at the tip of the defect manage to reach the edge of the detector region and do not diffuse away from the CC. At a higher temperature, $T = 0.01$, the voltages fall as the vortices move through the accelerator, channel and detector regions showing that not all vortices reach the detector region. Furthermore,

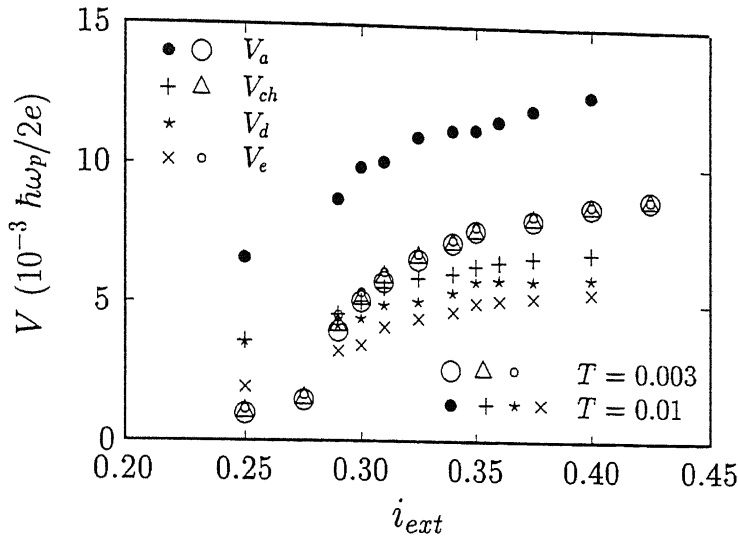


Figure 5.2: A plot of average voltages in various regions of the array versus current i_{ext} applied in the accelerator region.

the voltage V_e is smaller than V_d showing that the vortex beam spreads and not all the vortices which hit the far end of the array do so right in the center. This behavior is just like the one seen by ZFOM. However, the typical value of the temperature T_d at which vortices start diffusing is found to be $\sim 0.01E_J$ as compared to $\sim 0.1E_J$ by ZFOM.

There are three reasons for this discrepancy: The pinning potential in a square array (our case) is ~ 5 times larger than for a triangular array (ZFOM). With forces between vortices varying inversely as the separation between them, the linear density of vortices for a square array is ~ 5 times larger than that for a triangular array. At a given temperature with a certain density of thermally created vortices the annihilation of vortices in the vortex-street is then ~ 5 times larger in a square array (cf. law of mass action). The loss of a single vortex from the vortex-street disturbs the VVI mediated motion of the whole vortex-street. Secondly, we have no bus bars and any vortex in the vortex-street which gets out of the CC easily diffuses towards the current-driven

edges. Thirdly, ZFOM have reduced the i_0 of junctions in the channel and detector region to facilitate the entry of vortices in that region. We find in our simulations that having bus bars and changing the i_0 of selected junctions increases the ratio V_e/V_{ch} at a given T . All these effects are of the correct sign and order of magnitude to roughly give agreement with ZFOM for the values of T_d .

5.3 Vortex Vortex Interactions

To trace the origin of the propagation of vortices in the field-free region we first study quantitatively the interaction between vortices in finite-size arrays. We take boundaries into account by introducing image charges across each edge of the array. We check all our calculations against simulations in arrays of sizes 16×128 and 32×64 . A uniform current drive of 0.9 initially applied to all rows is turned off after a desired number of vortices have been injected into the array from a defect with $n = 5$.

We first consider the case of a single injected vortex. This gets pinned in the CC, all voltages drop to zero and only supercurrents due to the vortex flow after i_{ext} is turned off. This pinned vortex can be moved by applying a local current i_d to each of the two left corners of the plaquette containing the vortex and withdrawing it from the two right corners. With the vortex positioned close to the center of the array, the effect of its image charges across the edges is negligible. We now vary i_d and measure the threshold current i_t required to depin and move the vortex to an adjacent plaquette in the CC. We find that $i_t = 0.167$, independent of the direction of depinning. The effective current exerting a Lorentz force on the vortex is the average current flowing in the top and bottom bonds of the plaquette containing the vortex. This can be found by measuring the fraction α of the current i_d which flows through these bonds in the absence of the vortex. We measure $\alpha = 0.6338$. Hence, the depinning current i_p for a single vortex is given by $i_p = \alpha i_t = 0.106$, in agreement with the predicted theoretical value[61].

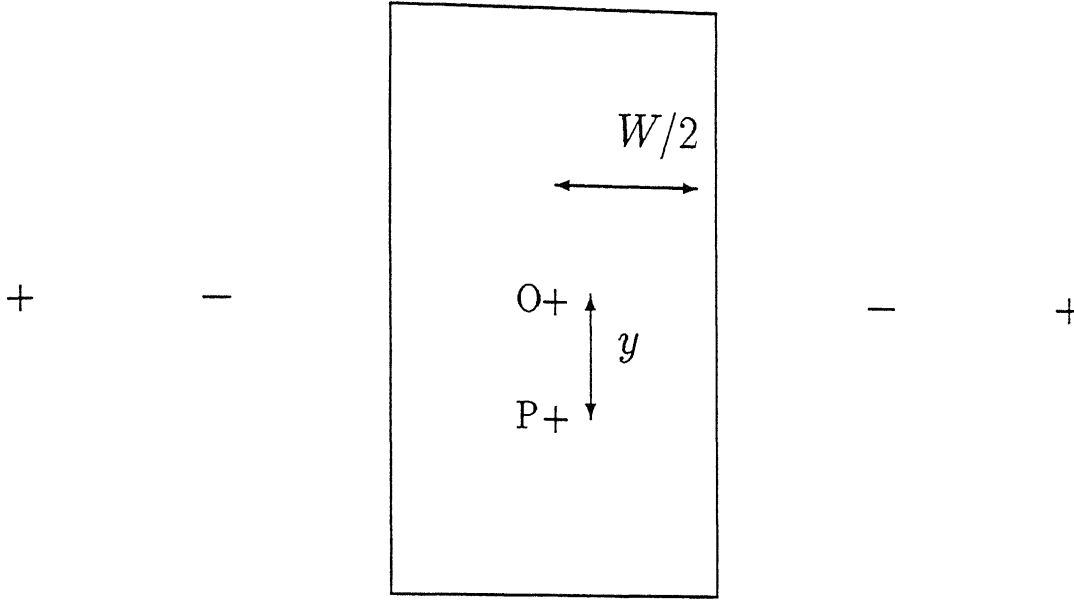


Figure 5.3: The images of the charge at O in the x direction and the test charge P

We consider next the VVI between two vortices located at y_i and y_j in the central column (point O and P in Fig. 5.3 respectively). As topological charges in 2D they interact via a logarithmic potential, $-2\pi E_J \log y_{ij}$ where $y_{ij} = |y_i - y_j|$. The repulsive force, $F_{ij}(y_i, y_j)$, between the vortices is however modified by the effect of an infinite array of image charges across the edges of the finite array of length L and width W . Hence, we calculate the net force between the two vortices taking into account the effect of the image charges ¹.

Due to finiteness of the array in the x direction there exists a one-dimensional infinite array of images of the charge placed at O at points nW $n = -\infty, \dots, 0, \dots, \infty$. Since the set of image charges are symmetric about the y axis, the force exerted on the test charge placed at P at a distance y_{ij} from O , has only a vertical component given by

¹We neglect the effect of the linear defect in the array on the vortex-vortex interaction.

$$\begin{aligned}
F &= 2\pi E_J \left[\frac{1}{y_{ij}} + 2 \sum_{n=1}^{\infty} \frac{(-1)^n}{(y_{ij}^2 + n^2 W^2)^{\frac{1}{2}}} \frac{y_{ij}}{(y_{ij}^2 + n^2 W^2)^{\frac{1}{2}}} \right] \\
\frac{F}{2\pi E_J} &= \frac{1/W}{y_{ij}/W} + 2 \frac{y_{ij}/W}{W} \sum_{n=1}^{\infty} \frac{(-1)^n}{(y_{ij}/W)^2 + n^2} \\
&= \frac{1}{W} \left[\frac{1}{z} + 2z \sum_{n=1}^{\infty} \frac{(-1)^n}{z^2 + n^2} \right] \text{ where } z = \frac{y_{ij}}{W} \\
&= \frac{\pi}{W} \operatorname{cosech}\left(\frac{\pi y_{ij}}{W}\right)
\end{aligned} \tag{5.1}$$

It is interesting to note that as the above expression is dependent only on y_{ij} as long as both the charges are placed along the y axis.

Having found the effect of image charges due to finiteness of the array in the x direction, we proceed to calculate the effect of image charges due to finiteness in the y direction. In Fig. 5.4 we show the positions, the descriptive scheme for naming the charges and their signs. All distances are measured from the origin. We divide the region into two halves separated by the origin and the m^{th} charge on the lower (upper) half is called y_{ml} (y_{mu}). Moreover we note that each image charge is in actuality a representative of a set of line charge perpendicular to the $x = 0$ line due to the finiteness of the array in the x direction as noted above. The general recursion relation that holds between the upper and the lower half sequences of image charges are:

$$\begin{aligned}
y_{nl} &= |y_{(n-1)L}| + L \\
|y_{nu}| &= y_{(n-1)l} + L \\
y_{nu} &= -|y_{(n-1)l}| \\
y_{1l} &= L + y_1 \\
y_{1u} &= L - y_1
\end{aligned} \tag{5.2}$$

The terms arising out of +ve charges in the upper half are from the previous analysis of the form $\sum_{m=0}^{\infty} \operatorname{cosech}(2mL + \Delta y)$ while those arising arising out of -ve terms are $\sum_{m=0}^{\infty} \operatorname{cosech}([2m+1]L + Y)$, where $\Delta y = y_2 - y_1$ and $Y = y_1 + y_2$. A similar analysis for the lower half shows that the sum from +ve charges gives $\sum_{m=0}^{\infty} \operatorname{cosech}([2m+1]L - Y)$ while those arising from -ve charges give $\sum_{m=1}^{\infty} \operatorname{cosech}(2mL - \Delta y)$. Incorporation of

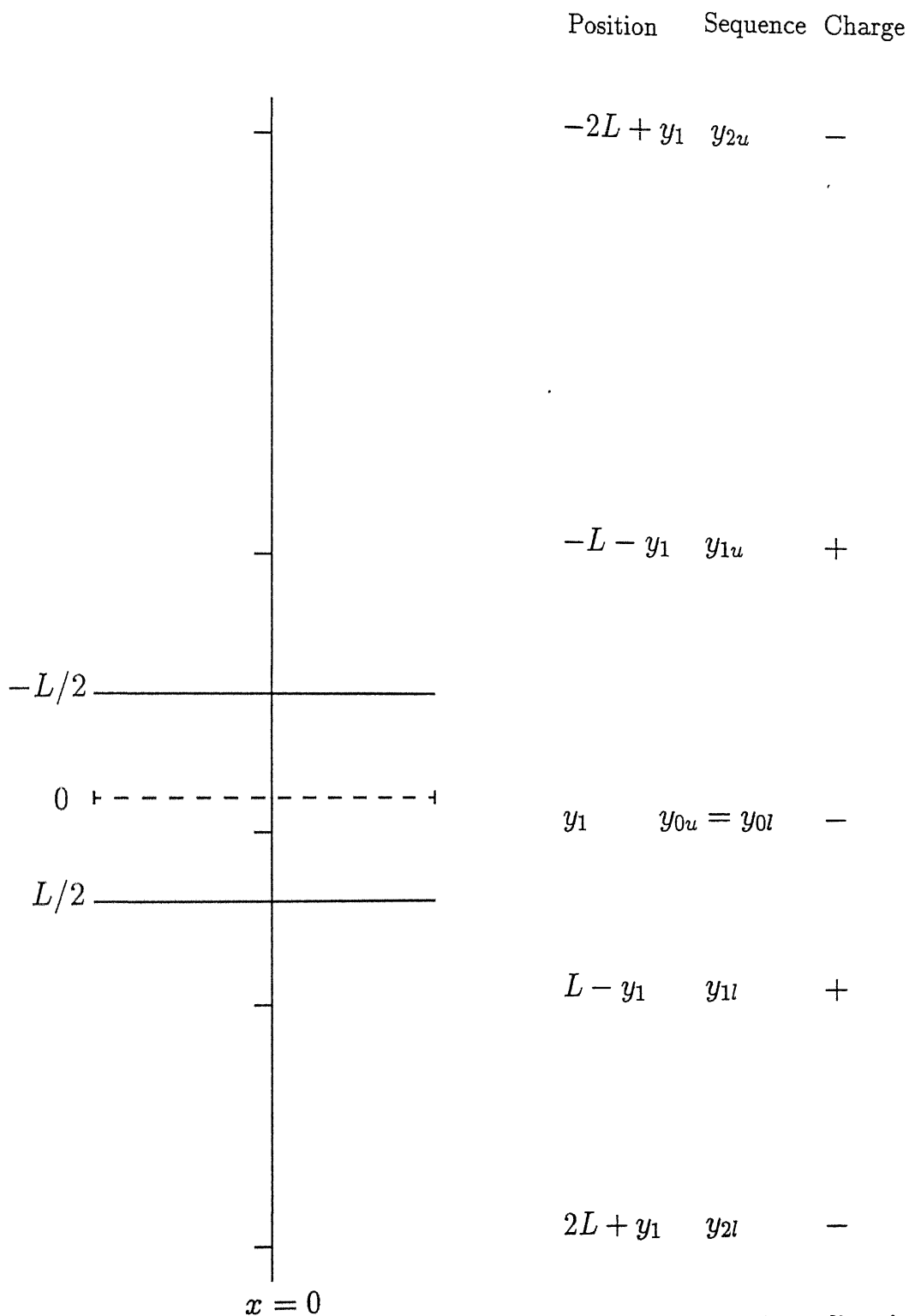


Figure 5.4: The figure shows the positions of the image charges in the y -direction due to a $-ve$ charge placed at y_1 . The positions as measured from the origin (O), the sequence for naming the charges and their signs are given on the right. Note that each image charge in actuality corresponds to a series of charges in the x direction with the same y coordinate.

the self-interaction term in the above formalism is straight-forward and is done by putting $y_1 = y_2$ and hence $Y = 2y_2$, $\Delta y = 0$. Taking care that a charge cannot have self-interaction with itself we finally arrive at resultant force due to vortex-vortex interactions as

$$F_{vv} = 2\pi E_J \frac{\pi}{W} \left[\sum_{m=0}^{\infty} \operatorname{cosech} \frac{\pi}{W} (2mL + \Delta y) - \operatorname{cosech} \frac{\pi}{W} ([2m+1]L + Y) \right. \\ \left. + \operatorname{cosech} \frac{\pi}{W} ([2m+1]L - Y) - (1 - \delta_{m0}) \operatorname{cosech} \frac{\pi}{W} (2mL - \Delta y) \right. \\ \left. - \operatorname{cosech} \frac{\pi}{W} ([2m+1]L + 2y_2) + \operatorname{cosech} \frac{\pi}{W} ([2m+1]L - 2y_2) \right] \quad (5.3)$$

Knowing the force due to such a configuration one can deduce the “current-equivalent” by using the relationship $F = (I\phi_0)/a$ where a is the dimension of the plaquette. For the general case of two vortices present in the CC at distances y'_i and y'_j one can write this force in a more compact notation as

$$F_{ij}(y'_i, y'_j) = \frac{\pi}{W} \operatorname{cosech}(y'_{ij}) + \frac{\pi}{W} \sum_{j=(-1,1)} j \sum_{k=1}^{\infty} \left\{ \operatorname{cosech}(2kr + jy'_{ij}) \right. \\ \left. + \operatorname{cosech}[(2k-1)r - jY'_{ij}] + \operatorname{cosech}[(2k-1)r - 2jy'_i] \right\} \quad (5.4)$$

where $r = \pi L/W$, $y'_i = \pi y_i/W$, $Y'_{ij} = y'_i + y'_j$, and F_{ij} is the force in units of $2\pi E_J/a$. For either vortex, i_t now depends upon the direction of movement and is larger for moving the vortices closer.

For multiple vortices present in the CC, the net force \vec{F}_i on the i^{th} vortex due to all other vortices is given by $\vec{F}_i = \sum_{j \neq i} \vec{F}_{ij}$. Hence, i_t is given by

$$\alpha i_t = F_i + i_p \quad (5.5)$$

Here, F_i is taken to be negative (positive) when i_t moves the vortex in a direction parallel (antiparallel) to that of \vec{F}_i . A plot of i_t against F_i is shown in Fig. 5.5 for a variable number of pinned vortices and array sizes. For the two-vortex case the force F_i is varied by changing y_{ij} . This can be done by applying the local current drive i_d to either vortex until the desired y_{ij} is achieved. For the multiple vortex case, a range of F_i values is obtained by simply measuring i_t for each vortex in the CC. The fit to

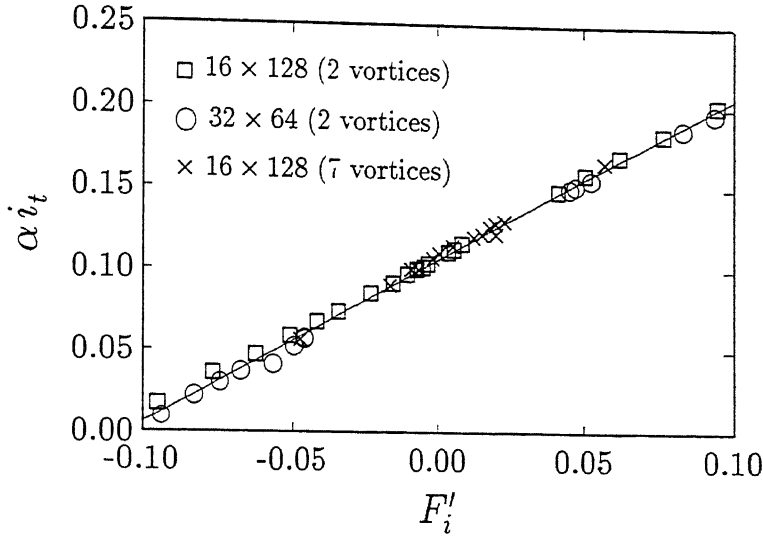


Figure 5.5: The threshold current required to depin a vortex plotted as a function of the force due to VVI on the vortex. The solid line is a linear least square fit to all the measured points using Eq. (5.5) with $i_p = 0.106$.

Eq. (5.5) is excellent and yields an $i_p = 0.106$, in agreement with the value for a single vortex. We conclude that pairwise interactions taking into account images of vortices across the edges of the array are adequate to describe all the VVI relevant here.

5.4 Equation Of Motion Of Vortex

We can now analyze the motion of the vortex-street in the CC. The vortex farthest from the defect in array B invariably lies in a region free from fields due to the i_{ext} applied in the accelerator region. The equation of motion for a vortex moving under an i_{ext} in a square array[137], modified to include the VVI, can be written as

$$m \frac{d^2 y}{dt^2} + \eta \frac{dy}{dt} + [i_p \sin(2\pi y) - i_{ext} - i_{vv}] = 0 \quad (5.6)$$

where $m = \pi\beta_c$ and $\eta = \pi$ dimensionless vortex-mass and viscosity, respectively.² The coordinate of the moving vortex is y and time is scaled in ω_c^{-1} . The current equivalent, i_{vv} , of the force on the vortex due to the other vortices, located at positions y_j in the CC, is given by $i_{vv} = \sum_j F(y, y_j)$. It should be noted that a single massless vortex, i.e. without the VVI and $m = 0$, in a zero external field ($i_{ext} = 0$), Eq.(5.6) yields $\dot{y} = 0$, implying no motion.

In Fig. 5.6 we show the measured position of the vortex in the CC as a function of time in array B for $T = 0$ and $\beta_c = 0, 10$ and 100 . The vortex is pushed by the 12 to 13 vortices behind it (one gets created at the tip of the defect before the vortex under study leaves the array). Also shown are the results of integrating Eq. (5.6) with and without the mass term, $\pi\beta_c$, for $i_{ext} = 0$ and $i_p = 0.106$. We note that $m = 0$ gives an excellent fit to the $\beta_c = 0$ and 10 data. For $\beta_c = 100$, the $m = 0$ curve is much closer to the experimental points than the one for $m = \pi\beta_c$. The data and the $m = 0$ fit for $\beta_c = 100$ can be made to agree with an enhancement in viscosity by a factor ~ 3 [152, 153]. We conclude that (i) the VVI are sufficient to explain the motion of vortices in the field-free detector region and (ii) the effective vortex-mass is insignificant for the studied range of β_c . Our results thus confirm the findings of Hagenaars *et al.*[137] that vortices have a negligible mass for $\beta_c \leq 35$.

A few additional observations are in order. Firstly, while a vortex is moving through the field-free region, i_{vv} stays just above the threshold i_p , as can be deduced from the step-like structure in Fig. 5.6. Secondly, the separation between vortices in the CC is quite *non-uniform*, e.g., it varies from 4 to 19 lattice spacings in array B as one moves from the defect tip to the edge of the array. It is worth pointing out that in a triangular lattice, where the pinning potential is ~ 5 times smaller than in a square array, vortices would flow even if they were approximately 50 lattice spacings apart

²Hagenaars *et al.*[137] have found that η is quite nonlinear and can be fitted well by the function $\eta = A/[1 + B\dot{y}]$ where A and B are constants weakly dependent upon β_c . This fit is, however, over a very large range of drive current whereas our drive current equivalent of the vortex-vortex interaction is very close to i_p . The parameters A and B are dependent upon the range of drive current used in fits. It is not clear how well the above form of viscosity fits to the very narrow range of drive current applicable to our studies. Hence, we use $\eta = \pi$.

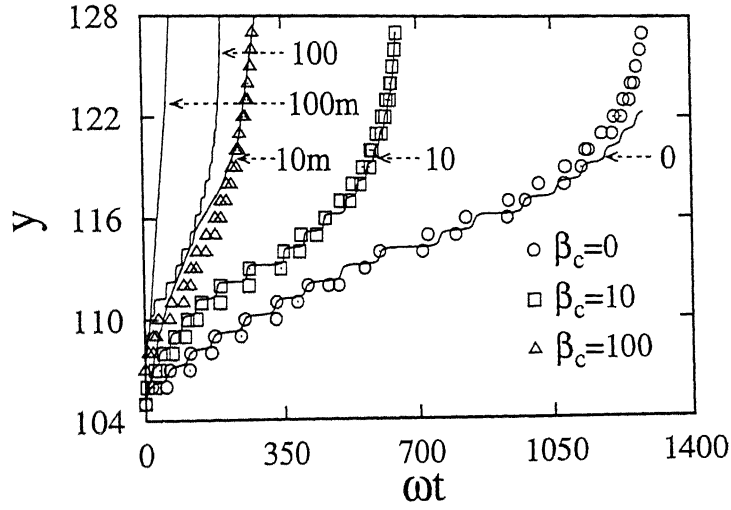


Figure 5.6: A plot of the position of vortex versus time. The origin of time is arbitrary. The frequency $\omega = \omega_c$ for $\beta_c = 0$ and $\omega = \omega_p$ for $\beta_c > 0$. The solid lines are fits obtained from integrating the equation of motion given by Eq. (5.6) with $i_{ext} = 0$ and $i_p = 0.106$ with and without the mass term. The β_c values are marked next to each of the fitted curves and the suffix m denotes inclusion of the mass term.

with $F_{ij} \propto 1/y_{ij}$. This is consistent with the estimate of ZFOM that there is at most one vortex at a given time in the channel region which is 20 lattice spacings long. In any case, as we have shown the vortices in the detector region pile up until the vortices are close enough to overcome the pinning potential. Since the VVI is a mutual force, there may arise a confusion as to how such a term can lead to a overall drift velocity in a particular direction. This seemingly paradoxical viewpoint can be brought in agreement by noting that the defect (which acts like a gun shooting out vortices) is constantly pushing in new vortices causing a net force in a particular direction. We have noted that if the current is stopped the vortex street expands due to the mutual repulsion between vortices.

For the sake of completeness, we have also simulated H-shaped arrays with vortices produced by an external magnetic field and used bus bars as in the experiments of ZFOM. We find the same results qualitatively. Good quality numerical data would, however, require prohibitive amounts of computer time ³. This is unwarranted as all the essential features of the experiments can be interpreted in the context of the experimentally realizable geometry we have used.

5.5 Discussion and Conclusion

In a capacitive triangular array, the effect of oscillations of a vortex inside a single plaquette is seen to be small: assuming a typical distance of 20 lattice spacings between two vortices, the maximum amount of tilt from the line of alignment is $\tan^{-1}(1/20)$. The busbars also help in aligning the vortices which as a result do not “fan” out. Furthermore, since there is an order of magnitude difference between temperature at which vortices diffuse in square arrays as compared to that in triangular lattices, experiments probing such effects in square arrays, must be carried out at a much lower temperature.

³The present simulations were done on a Hewlett-Packard series 9000 model 735 workstation.

To conclude, we have shown that VVI *can* overcome the vortex-pinning potential in JJAs and cause the vortices to move through a field-free region. The experimental observations of ZFOM can thus be understood in terms of VVI alone without recourse to ballistic motion of vortices. Our findings are consistent with the numerical simulations which have failed to observe ballistic motion for a single vortex. More experiments, preferably with a single vortex, are needed to confirm if ballistic motion of vortices indeed exists for some other range of parameters. Further theoretical insights as well as new experiments are also required to explain the absence of a vortex-mass for the range of β_c studied and better understand the dynamics of vortices in JJA.

Chapter 6

Results and Discussions

We now summarize and review our results and discuss their ramifications.

6.1 Results

In listing these we proceed chapter-wise.

Chap. 2 deals with fast simulational algorithms for square JJAs described using the RSJ model. We have shown that the complexity of the algorithms can be reduced from $\mathcal{O}(N^2)$ to $\mathcal{O}(N \ln N)$ at each integration time step for a number of experimentally studied cases. We have done this by noting that there exists an analogy between our differential equations and those of electrostatics, that a knowledge of the corresponding eigenvectors and eigenvalues of the underlying differential operators when subject to the correct boundary conditions determines the Green's function (G) and that gauge fixing removes the zero mode invariably present in G . For finite arrays we have determined the solutions by using a combination of the degenerate eigen vectors which possesses the symmetry of the underlying lattice. In all cases we have specifically identified the fast transform to be used to integrate the equations of motion.

- The Periodic Square Lattice: In this case the eigen vectors have been shown to be $\sim \exp(i\vec{k} \cdot \vec{r})$ with $k_i = 2n_i\pi/L$, $i = x, y$ $n_i = 0, 1 \dots L_i - 1$ while the eigenvalues

are $4 - 2 \cos k_x - 2 \cos k_y$. A 2D Fourier transform has been shown to provide a fast algorithm.

- A Finite Square Lattice : The extra Neumann-like boundary conditions arising from the finiteness of the array lead us to a solution of the form $\sim \cos k_x x \cos k_y y$, $k_i = n_i \pi / L_i$, $i = x, y$, $n_i = 0, 1 \dots L_i - 1$ for (x, y) located at the dual lattice sites. The eigenvalues remain the same as above. For L_x and L_y of the form 2^p , a 2D Cosine Transform, provides a faster method.
- A Finite Square Lattice with Single Bus Bar: By observing that the vanishing of wavefunction at the bus bar automatically removes the zero eigenvalue, we have been shown that $\Psi(x, y) \sim \sin k_x x \cos k_y y$ with $k_x = (n_x \pi) / (L_x + 1/2)$, $n_x = 0, 1 \dots L_x - 1$ and k_y as above. These eigenfunctions, however, make the use of fast algorithms of the form described above impossible. Consequently, we have introduced a variant of the above method to make the process faster. This uses cosine transforms in one direction (y) and cyclically reduces the non-diagonal G matrix in the k space to a tridiagonal form before solving it in the other. The essence of the procedure is described in Fig. 2.5.
- A Finite Square Lattice with Double Bus Bars: In this case too the busbars in the x -direction modify the eigen functions to $\sim \sin k_x x \cos k_y y$ with $k_i = n_i \pi / L_i$, $x = 0, 1, \dots L_x - 1$, $y = 1/2, 3/2, \dots L_y - 1/2$ while the eigenvalues remain unchanged. It then follows that a fast algorithm is possible if $L_x + 1 = 2^p$ and $L_y = 2^q$.

In the case of missing bonds, the above procedure is rendered inapplicable, since these introduce internal boundaries. An alternative route, used by us, relies on isolating the effects of bond removal into a separate matrix h and proceeding perturbatively. By adapting a procedure commonly used for the case of disordered systems, we have shown that the resulting series (see Eq.(2.49)) can be summed exactly leads to a algorithm with complexity $\mathcal{O}(N \ln N + N)$. The extension of the above procedure to the case of n missing bonds in the form of a linear defect, has been shown to yield a process with complexity $\mathcal{O}(N \ln N + nN)$.

Chap. 3 extends the above analysis to the case of triangular arrays. We have used the Dirac bra-ket notation to describe the JJA and in the process made the mathematical analysis much more elegant and transparent. It has been observed that the very nature of the triangular lattice makes the corresponding eigenfunctions non-separable in the spatial directions. We have noted that the eigen values of the matrix G_0^{-1} possess the 12-fold symmetry of the hexagonal group. For periodic triangular lattices, we have had to additionally incorporate the concept of different kinds of periodicity to specify the connectivity of the lattice points at the boundaries. We find that there exist two forms of periodicity viz., rectangular and hexagonal. We have evolved fast algorithms for each, in addition to one for a finite lattice as discussed below:

- Rectangularly Periodic Triangular Lattice: The results for this case have yielded a solution is similar to that for a periodic square lattice with the exception of the eigen values which are now $6 - \cos k_1 - \cos k_2 - \cos(k_1 - k_2)$; $k_i = 2n_i\pi/L, i = 0, 1$; $n_i = 0, 1, \dots, L_i - 1$.
- Hexagonally Periodic Triangular Lattice: Viewing the josephson lattice as a subset of a 2D-plane on which data is finitely sampled, we have shown that for such a lattice the eigenfunctions are $\sim \exp -i \left[\frac{\pi}{3L}(2x_1 - x_2)(2n_1 - n_2) + \frac{\pi}{L}x_2n_2 \right]$ and possess the 12-fold symmetric eigen value $6 - 2 \cos(2n_1 - n_2)\frac{2\pi}{3L} - 2 \cos(2n_2 - n_1)\frac{2\pi}{3L} - 2 \cos(n_1 + n_2)\frac{2\pi}{3L}$ with $0 \leq n_1 < 3L, 0 \leq n_2 < L$. The properties (see Sec. 3.3.2) of the wavefunction have been shown to yield a fast algorithm if $L = 2^p$.
- Finite Triangular Lattice: In this case we have shown that that the wavefunctions do not completely diagonalise the matrix G_0^{-1} . However, after certain manipulations, G_0^{-1} is seen to reduce to a tridiagonal form which can then be solved with increased efficiency.

Chap. 4 deals with our work on bond diluted and disordered defects. The results are as below:

- For the case of bond disorder, with grading $g < g_m = 0.2$, we find vortices pinned inside the linear defect. The pinned vortices are seen to increase the stability of the system against breakdown.
- Our findings reveal that the barrier height for vortex motion, and hence the depinning current, is highly anisotropic and can be greater than i_p^∞ for *rectangular* arrays. As a result, we observe that vortices are pinned by a long narrow lattice with bond-diluted linear defects of size much less than predicted earlier. These pinned vortices are seen to raise the i_c of the system (Fig. 4.5). We also show that there exists a scaling behaviour of $\Delta i_c / i_c^\infty$ with N_x / n for fixed N_y / n (Fig. 4.4). Moreover, for small N_x , vortices are seen to flow in the direction of the current due to an increased gradient of current flow near the tip of the defect,
- The energy of the system in the steady-state regime has been conveniently divided into various sectors with each sector being characterised by the number of pinned vortices present in the array. The energy decreases continuously within each sector and registers a discontinuous downward kink while crossing from one sector to a higher one. Hysteresis in the E vs i_{ext} plane is observed. This occurs because the pinned vortices do not escape from the array, even when the external current is reduced to zero.
- The periodic regime of the array reveals the presence of waves that carry the vortices. The wavelength of the wave is seen to increase as one moves towards the edge of the array. A snapshot of the phases also reveals a “wake” that moves ahead of the vortex and provides energy to propel it forward.
- An analysis of other defects patterns affirms the analogy between current flows in JJAs and hydrodynamic flows. Since the curvature of flow lines decides the point of breakdown, effective streamlining of a defect is seen to increase i_c .

We have investigated in Chap. 5 the flow of vortices predicted to occur ballistically in underdamped JJAs at finite temperature. Our findings are summarised below.

- We have shown that a linear defect provides a suitable geometry to experimentally and numerically study ballistic vortex motion since it produces a naturally collimated beam of vortices.
- It is observed that although a single vortex does not move ballistically, a vortex street *can* move through a field-depleted zone even in an *overdamped* array.
- At finite temperatures we find that the vortices diffuse so that only a fraction of those produced by the defect reach the detector. The discrepancy, between our simulations and experiments in the literature, in the temperature at which such diffusion becomes prominent, is argued to be due to a difference between the pinning potentials of triangular and square arrays.
- We have found that the current required to depin a vortex in the presence of other vortices is $\sim 0.1i_0$ as found for the infinite array limit. To arrive at this value, we take into account the complete vortex-vortex interactions inclusive of the effects of the array of image charges present across the edges of the lattice (Eq.(5.4)).
- We determine the displacement of a free vortex as a function of time by including the current equivalent of the VVI in the vortex equation of motion (Eq.(5.6)). The agreement between the numerical and observed data is startling (Fig. 5.6). Our curve further reveals that for $\beta_c \lesssim 30$ the mass of the vortex is zero.

6.2 Discussion and Scope For Further Study

We have shown that algorithms for simulating a number of experimental JJAs e.g. those with bus-bars and/or defects as also those subject to magnetic fields, noise, and/or current drives, all involve Green's functions specific to the underlying lattice in question. Furthermore, the Green's function of interest can straight-forwardly be constructed once the eigen-basis of the corresponding connectivity matrix or discrete

Laplacian has been determined. We have provided a much more transparent rederivation of the Eikmans–Himbergen algorithm using this method. The extensions of this algorithms to the case of 3D arrays is easy since the corresponding eigen-vectors are specified to be either $\exp(i\vec{k} \cdot \vec{r})$ or $\cos(k_x x)$ depending on whether the boundaries are periodic or free boundaries respectively. The eigen-values are now changed to $6 - 2\cos k_x - 2\cos k_y - 2\cos k_z$. In this case, one has to obviously use 3-D transforms.

We have also provided a general method for adding and removing bonds from a configuration whose Green's function is known. This can be used to create a variety of defects whose properties can then be studied. In this thesis we have only explored the possibility of bond-removal. It would be interesting to determine the effect of bond-additions especially since these would change the pinning potential for vortices. Random defect configurations which can also be studied by this method, represent yet other systems of interest.

It is also worth noting that many of the expressions we have derived, e.g. those for the Green's functions, can be written in terms of continuous functions, which are, of course, to be evaluated or sampled only at points belonging to the array. Now if we turn this observation around and think of the discrete lattice as being *produced* by the sampling of a continuous 2-D waveform, we make contact with a long-standing problem in electrical engineering, viz. that of the digitisation and subsequent recovery of band-width limited analog wave-forms. We can thus make a useful correspondence between the algorithms presented here and those used in digital signal processing of data.

We have used this analogy, in part, to extend the scope of our algorithms to triangular arrays. A case in point is that of the hexagonally periodic/finite triangular lattice which in either cases admits eigenvectors akin to those derived arrived by Merserau[133]. The finite case is rather more difficult for the triangular lattice than it is for the square one. This is because the creation of a boundary in the former, requires the removal of two bonds placed obliquely with respect to each other, rather than one. This case therefore requires a new approach and this has been developed in this thesis.

In particular we have broken up the inverse laplacian G_0^{-1} into a periodic (P) and a boundary (B) matrix and have shown that for a specific choice of the basis both B and $P - B = G_0^{-1}$ take on forms which are amenable to diagonalisation in linear order. This has allowed us to present a computationally fast algorithm for the finite case.

It is also been pointed out that for a hexagonally periodic lattice, equivalent points in different tiles (see Ref.[133]) can be exchanged to create a new fundamental period. As a result these periods come in several shapes of which Fig.(3.1) is but one example. The corresponding eigenvalues and eigenfunctions of G_0^{-1} , however, remain unaltered and the $\mathcal{O}(N \ln N)$ algorithm continues to be equally applicable to each of them. These shapes can serve as starting points for creating several different finite lattices. The various types of boundaries which result are especially significant in view of the interesting question: For which class of boundaries does the matrix B commute with P ? Indeed if there are cases for which $[P, B] = 0$, they will automatically lead to $\mathcal{O}(N \ln N)$ algorithms.

The case of the triangular lattice opens up a set of questions which can form the foci of future investigations. For example, it would be interesting to determine the differences in the ground state of a hexagonally periodic and a rectangularly periodic triangular array in the presence of a magnetic field. These differences, if any, would reflect itself in a change of T_{BKT} . Furthermore, it would be useful to find if accidental degeneracy discovered in the case of rectangularly periodic arrays[139] with $f = 1/3$ and $f = 1/4$ occurs in the hexagonally periodic lattice too. Further investigations on the presence of various classes of Shapiro steps[141], the role of positionally disordered defects in dictating the dynamics of arrays[74] and more importantly the detection of ballistic motion in arrays of larger sizes can be attempted.

For the case of defects, several directions for further research are possible. Firstly, an understanding of the steady-state regime from a fixed point analysis of the evolution equations of the system is desirable. This can be achieved relatively easily for small arrays but becomes formidable as the system size increases. For an $N_x = 4$ array, a knowledge of the values of the external current and the phase at $(-1/2, N_y + 1/2)$

(Fig. 4.1) provides a complete solution via the application of current conservation at each node. Hence i_{ext} is a function of only one variable. A plot of i_{ext} versus the concerned variable provides solutions which consist of purely superconducting flow. A careful study, further, reveals that unstable solutions are also present. The breakdown of steady-state flow (i_c) is characterised by a marginally stable solution. The challenge is to generalize this procedure to larger arrays. In the case of pinned vortices, the position of the vortex constitutes a further input into a complete solution. Secondly, it is of interest to characterise the spin waves seen in the periodic regime, in terms of their dispersion relation. The subtlety lies in the fact that there exists a “frozen-in” wave in the steady because of which $\vec{k} \neq 0$ as $\omega \rightarrow 0$. A similar deviation from conventional spin wave behaviour exists in the presence of pinned vortices. Thirdly, an in depth study of the symmetry-breaking of the solutions $\theta(x, y) = -\theta(-x, y)$ in the chaotic regime is in order. In fact, we feel that the breaking of this symmetry, is a much better and faster signal for detecting chaos in JJAs than the conventional power spectrum method. Phenomena like bunching and debunching of several vortices in the column-switched regime also merit deeper study.

The idea of a “vortex-street” moving ‘ballistically’ through a field depleted zone has been introduced in Chap. 5. It has been shown by us and other authors independently that the mass of a vortex is negligibly small in contradiction to theoretical calculations. It would be interesting to see whether the interactions with the image charges due to the finiteness of the array, actually renormalise the inertial mass of vortices to zero. Since the exact position of the vortex inside a plaquette is unknown, one has to follow a boolean kind of logic whereby each vortex is either midway between the plaquette or absent. This is important if one tries to find the vortex motion of the second last vortex (instead of the last). Here any error in the position of the vortex is magnified by the VVI and makes the comparison between theoretical and numerical results much more difficult. It would hence be of interest if one can determine the position of a vortex inside a plaquette accurately.

Bibliography

- [1] B. D. Josephson, Phys. Lett. **1**, 251 (1962).
- [2] G. H. Dolan and J. H. Dunsmuir, Physica B **8**, 152 (1988).
- [3] H. S. J. van der Zant, F. C. Fritschy, T. P. Orlando and J. E. Mooij, Europhys. Lett. **18**, 343 (1992).
- [4] R. Theron, J. B. Sigmond, Ch. Lemann, H. Beck, P. Martinoli and P. Minnhagen, Phys. Rev. Lett. **71**, 1246 (1993).
- [5] J. M. Gordon, A. M. Goldman, J. Maps, D. Costello, R. Tiberio and B. Whitehead, Phys. Rev. Lett. **57**, 368 (1986); J. M. Gordon and A. M. Goldman, Phys. Rev. B. **35**, 4909 (1987); A. Behoorz, M. Burns, H. Deckman, D. Levine, B. Whitehead and P. M. Chaikin, Phys. Rev. Lett. **35**, 8396 (1987); F. Nori, Q. Niu, E. Fradkin and S. C. Chang, Phys. Rev. B. **36**, 8338 (1987); K. Springer and D. van Harlingen, Phys. Rev. B. **36**, 7273 (1987);.
- [6] H. Eikmans, Ph.D Thesis, University of Utrecht, Holland (1992).
- [7] M. Tinkham, *Introduction to Superconductivity* (McGraw-Hill, New York, 1975).
- [8] P. G. de Gennes, *Superconductivity of metals and alloys* (W. A. Benjamin, New York, 1966).
- [9] K. K. Likharev, *Dynamics of Josephson junctions and circuits* (Gordon and Breach, New York, 1986).

- [10] N. D. Mermin and H. Wagner, Phys. Rev. Lett. **17**, 1133 (1966).
- [11] P. C. Hohenberg, Phys. Rev. **158**, 383 (1967); J. M. Kosterlitz, J. Phys. C **7**, 1046 (1974).
- [12] T. Rice, Phys. Rev. **140**, A1889 (1965).
- [13] V. L. Berezinskii, Zh. Eksp. Teor. Fiz. **61**, 1144 (1971) [Sov. Phys. JETP **34**, 610 (1972)].
- [14] J. M. Kosterlitz and D. J. Thouless, J. Phys. C **6**, 1181 (1973).
- [15] J. M. Kosterlitz, J. Phys. C **7**, 1046 (1974).
- [16] C. J. Lobb, Physica **126** B, 319 (1984) and references cited therein.
- [17] P. Minnhagen, Rev. Mod. Phys. **59**, 1001 (1987).
- [18] B. Nienhuis, in *Phase Transitions and Critical Phenomena*, edited by C. Domb and J. L. Lebowitz, Volume 11, p. 1 (1987).
- [19] J. V. José, L. P. Kadanoff, S. Kirkpatrick, and D. R. Nelson, Phys. Rev. B **16**, 1217 (1977).
- [20] R. Savit, Rev. Mod. Phys. **52**, 453 (1980), Phys. Rev. B **17**, 1340 (1978).
- [21] J. Kogut, Rev. Mod. Phys. **51**, 659 (1979).
- [22] D. Sanchez and J. Berchier, J. Low Temp. Phys. **43**, 56 (1981).
- [23] J. Resnick, J. Garland, J. Boyd, S. Shoemaker and R. Newrock, Phys. Rev. Lett. **47**, 1542 (1981).
- [24] R. Voss and R. Webb, Phys. Rev. B **25**, 3446 (1982).
- [25] D. Kimhi, F. Leyvraz and D. Ariosia, Phys. Rev. B **29**, 1487 (1984).

- [26] B. van Wees, H. S. J. van der Zant and J. E. Mooij, Phys. Rev. B **35**, 7291 (1987).
- [27] D. Abraham, C. Lobb, M. Tinkham and T. Klapwijk, Phys. Rev. B **26**, 5268 (1982).
- [28] J. Carini, Phys. Rev. B **38**, 63 (1988).
- [29] R. Brown and J. Garland, Phys. Rev. B **33**, 7827 (1986).
- [30] K. K. Mon and S. Teitel, Phys. Rev. Lett. **62**, 673 (1989).
- [31] J. Mooij in *Advances in Superconductivity*, ed. B. Deaver and J. Runvalds, NATO ASI **100** (Plenum, N.Y. 1982); J. Mooij in *Percolation, Localization and Superconductivity*, ed. A. Goldman and S. Wolf, NATO ASI **109** (Plenum, N.Y. 1984).
- [32] P. Martinoli, Ph. Lerch, Ch. Leemann, and H. Beck, Jpn. J. Appl. Phys. **26**, Suppl 26-3, 1999 (1987); P. Martinoli, Helv. Phys. Acta **80**, 128 (1987); P. Martinoli, Physica B **152**, 146 (1988); Ch. Leemann, Ph. Lerch, G. A. Racine and P. Martinoli, Phys. Rev. Lett. **56**, 1291 (1986).
- [33] S. R. Shenoy, J. Phys. C **18**, 5163 (1985); Errata **20**, 2479 (1987).
- [34] H. S. J. van der Zant, H. A. Rijken, and J. E. Mooij, J. Low Temp. Phys. **82**, 67 (1991).
- [35] J. Villian, J. Phys. C **10**, 1717 (1977).
- [36] G. Toulouse, Commun. Phys. **2**, 1151 (1977).
- [37] S. Teitel and C. Jayaprakash, Phys. Rev. Lett. **51**, 1999 (1983).
- [38] T. C. Halsey, Phys. Rev. B **31**, 5728 (1985).
- [39] S. Teitel, Physica B **152**, 30 (1988).
- [40] T. C. Halsey, Phys. Rev. Lett. **55**, 1018 (1985); Phys. Rev. B **31**, 5728 (1985).

- [41] M. Tinkham, D. W. Abraham and C. J. Lobb, Phys. Rev. B **28**, 6578 (1983).
- [42] B. Pannetier, J. Chaussy, R. Rammal and J. C. Villegier, Phys. Rev. Lett. **53**, 1845 (1984).
- [43] S. Teitel and C. Jayaprakash, Phys. Rev. B **27**, 598 (1985).
- [44] T. C. Halsey, J. Phys. C **18**, 2437 (1985).
- [45] M. Yosefin and E. Domany, Phys. Rev. B **32**, 1778 (1985).
- [46] M. Y. Choi and D. Stroud, Phys. Rev. B **32**, 5773 (1985).
- [47] E. Granato, J. M. Kosterlitz and J. Poulter, Phys. Rev. B **33**, 4767 (1986).
- [48] Ch. Leemann, Ph. Lerch, G. A. Racine and P. Martinoli, Phys. Rev. Lett. **56**, 1291 (1986).
- [49] K. Efetov, Sov. Phys. JETP, **51**, 1015 (1980).
- [50] P. Anderson in *The Many-body Problem*, Vol. II, ed. E. Caianello, Academic, NY (1969), B. Abeles, Phys. Rev. B **15**, 2828 (1977).
- [51] J. José, Phys. Rev. B **29**, 2836 (1984).
- [52] L. Jacobs, J. V. José, M. A. Novotny, and A. M. Goldman, Europhys. Lett. **3**, 1295 (1987), L. Jacobs and J. José, Physica B **152**, 148 (1988).
- [53] U. Eckern and A. Schmid, Phys. Rev. B **39**, 6441 (1989).
- [54] U. Eckern in *Application of Statistical and Field Theory Methods to Condensed Matter* ed. D. Baeriswyl, A. R. Bishop and J. Carmelo, NATO ASI Series **218**, 311 (Plenum, N.Y., 1990).
- [55] S. E. Korshunov, Physica B **152**, 261 (1988).
- [56] P. A. Bobbert, Phys. Rev. B **45**, 7540 (1992).

- [57] U. Geigenmuller, C. J. Lobb, and C. B. Whan, *Phys. Rev. B* **47**, 348 (1993).
- [58] Wenbin Yu, K. H. Lee and D. Stroud, *Phys. Rev. B* **47**, 5706 (1993).
- [59] Wenbin Yu and D. Stroud, *Phys. Rev. B* **49**, 6174 (1994).
- [60] R. Fazio, A. van Otterlo, and G. Schon, *Europhys. Lett.* **25**, 453 (1994).
- [61] C. J. Lobb, David W. Abraham and M. Tinkham, *Phys. Rev. B* **27**, 150 (1983).
- [62] V. Ambegaokar and B. I. Halperin, *Phys. Rev. Lett.* **22**, 1364 (1969); *Errata* **23** 274 (1969).
- [63] W. C. Stewart, *Appl. Phys. Lett.* **12**, 277 (1968).
- [64] D. E. McCumber, *J. Appl. Phys.* **39**, 3113 (1968).
- [65] M. G. Forrester, H. J. Lee, M. Tinkham, and C. J. Lobb, *Phys. Rev. B* **37**, 5966 (1988).
- [66] B. Berge, H. T. Diep, A. Ghazali and P. Lallemand, *Phys. Rev. B* **34**, 3177 (1986).
- [67] H. Eikmans, J. E. van Himbergen, H. J. F. Knops and J. M. Thijssen, *Phys. Rev. B* **39**, 11759 (1989).
- [68] J. S. Chung, K. H. Lee, and D. Stroud, *Phys. Rev. B* **40**, 6570 (1989).
- [69] Y. H. Li and S. Teitel, *Phys. Rev. Lett.* **67**, 2894 (1991).
- [70] W. Y. Shih, C. Ebner, and D. Stroud, *Phys. Rev. B* **30**, 134 (1984).
- [71] M. G. Forrester, S. P. Benz, and C. J. Lobb, *Phys. Rev. B* **41**, 8749 (1990).
- [72] S. P. Benz, M. G. Forrester, M. Tinkham and C. J. Lobb, *Phys. Rev. B* **38**, 2869 (1988).
- [73] E. Granato and J. M. Kosterlitz, *Phys. Rev. B* **33**, 6533 (1986).

- [74] D. Dominguez, J. V. José, A. Karma and C. Weicko, Phys. Rev. Lett. **67**, 2367 (1991).
- [75] D. C. Harris, S. T. Herbert, D. C. Stroud and J. C. Garland, Phys. Rev. Lett. **67**, 3606 (1991); Physica B **165** & **166**, 1643 (1990).
- [76] W. Xia and P. L. Leath, Phys. Rev. Lett. **63**, 1428 (1991).
- [77] P. L. Leath and W. Xia, Phys. Rev. B **44**, 9619 (1991).
- [78] R. Mehrotra and S. R. Shenoy, Europhys. Lett. **9**, 11 (1989).
- [79] R. Mehrotra and S. R. Shenoy, Phys. Rev. B **46**, 1088 (1992).
- [80] Ravi Bhagavatula, C. Ebner and C. Jayaprakash, Phys. Rev. B, **45**, 4774 (1992).
- [81] S. Shapiro, Phys. Rev. Lett. **11**, 80 (1963).
- [82] T. D. Clark, Phys. Rev. B **8**, 137 (1987).
- [83] S. P. Benz, M. S. Rzchowski, M. Tinkham and C. J. Lobb, Phys. Rev. Lett. **64**, 693 (1990); and Physica B **165** & **166**, 1645 (1990).
- [84] K. H. Lee, D. Stroud, and J. S. Chung, Phys. Rev. Lett. **64**, 962 (1990).
- [85] Proceedings of the NATO Advanced Research Workshop on *Coherence in Superconducting Networks*, Delft, The Netherlands, December 1987, edited by J. E. Mooij and G. B. J. Schon, Physica B **152**, 1-302 (1988).
- [86] Recent reviews in Macroscopic Quantum Phenomena and Coherence in Superconducting Networks, Frascati, Italy, March 1995, edited by C. Giovannella and M. Tinkham.
- [87] Recent reviews in Proceedings of Mini Workshop On Josephson Junction Arrays, Physica C (to be published).
- [88] S. E. Korshunov, J. Stat. Phys. **43**, 17 (1986).

- [89] S. E. Korshunov and G. V. Uimin, *J. Stat. Phys.* **43**, 1 (1986).
- [90] D. H. Lee, J. D. Joannopoulos, J. W. Negele and D. P. Landau, *Phys. Rev. B* **33**, 450 (1986).
- [91] J. M. Thijssen, *Phys. Rev. B* **40**, 5211 (1989).
- [92] J. M. Thijssen and H. J. F. Knops, *Phys. Rev. B* **42**, 2438 (1990).
- [93] G. S. Grest, *Phys. Rev. B* **39**, 9267 (1989).
- [94] M. Y. Choi and S. Doniach, *Phys. Rev. B* **31**, 4516 (1985).
- [95] E. Granato and J. M. Kosterlitz, *J. Phys. C* **19**, L59 (1986); *J. Appl. Phys.* **64**, 5636 (1988).
- [96] E. Granato, J. M. Kosterlitz, J. Lee, and M. P. Nightingale, *Phys. Rev. Lett.* **66**, 1090 (1991).
- [97] J. Lee, J. M. Kosterlitz and E. Granato, *Phys. Rev. B* **43**, 11531 (1991).
- [98] E. Granato, *J. Phys. C* **20**, L215 (1987).
- [99] J. E. van Himbergen, *Phys. Rev. B* **33**, 7857 (1986); *Phys. Rev. B* **34**, 6567 (1986).
- [100] J. E. van Himbergen, *Physica B* **152**, 46 (1988).
- [101] Y. H. Li and S. Teitel, *Phys. Rev. Lett.* **65**, 2595 (1990).
- [102] H. Eikmans and J. E. van Himbergen, *Phys. Rev. B* **41**, 8927 (1990); H. Eikmans, J. E. van Himbergen, H. S. J. van der Zant, K. de Boer and J. E. Mooij, *Physica B* **165 & 166**, 1569 (1990).
- [103] A. L. Scheinine, *Phys. Rev. B* **39**, 9368 (1989).
- [104] M. B. Cohn, M. S. Rzchowski, S.P. Benz and C. J. Lobb, *Phys. Rev. B* **43**, 12823 (1991).

- [105] F. Falo, A. R. Bishop and P. S. Lomdahl, Phys. Rev. B **41**, 10983 (1990).
- [106] M. S. Rzchowski, S. P. Benz, M. Tinkham and C. J. Lobb, Phys. Rev. B **42**, 2041 (1990).
- [107] D. Dominguez and H. Cerdiera, Phys. Rev. Lett. **71**, 3359 (1993); D. Dominguez and H. Cerdiera, Phys. Lett. A. **200**, 43 (1995).
- [108] D. Dominguez and J. V. José, Phys. Rev. B **48**, 13717 (1993).
- [109] D. Dominguez, Phys. Rev. Lett. **72**, 3096 (1994).
- [110] D. Dominguez and J. V. José, Int. J. Mod. Phys. B **8**, 3749 (1994).
- [111] K. Y. Tsang, S. H. Strogatz, and K. Wiesenfeld, Phys. Rev. Lett. **66**, 1094 (1991).
- [112] P. Hadley, M. R. Beasley, and K. Wiesenfeld, Phys. Rev. B **38**, 8712 (1988).
- [113] J. E. Lukens, in *Superconducting Devices*, edited by T. Rugiero and D. Rudman (Academic, New York, 1990).
- [114] For a recent review see D. V. Averin and K. K. Likharev, in *Mesoscopic Phenomena in Solids*, edited by B. L. Altshuler, P. A. Lee, and E. A. Webb (Elsevier, Amsterdam, 1991) p. 167.
- [115] L. L. Sohn, M. S. Rzchowski, J. U. Free, S. P. Benz, M. Tinkham, and C. J. Lobb, Phys. Rev. B **44**, 925 (1991).
- [116] P. A. Bobbert, R. Fazio, G. Schon, and G. T. Zimanyi, Phys. Rev. B **41**, 4009 (1990).
- [117] R. Fazio and G. Schon, Phys. Rev. B **43**, 5307 (1991).
- [118] H. S. J. van der Zant, F. C. Fritschy, W. J. Elion, L. J. Geerligs, and J. E. Mooij, Phys. Rev. Lett. **69**, 2971 (1992).

- [119] W. J. Elion, J. J. Wachters, L. L. Sohn and J. E. Mooij, Phys. Rev. Lett. **71**, 2311 (1993).
- [120] B. J. van Wees, Phys. Rev. Lett. **65**, 255 (1990).
- [121] Sujay Datta, Shantilal Das, Deshdeep Sahdev Ravi Mehrotra and Subodh R. Shenoy, submitted to Phys. Rev. B.
- [122] H. Eikmans and J. E. van Himbergen, Phys. Rev. B **41**, 8927 (1990).
- [123] Sujay Datta and Deshdeep Sahdev, submitted to Phys. Rev. B.
- [124] Sujay Datta, Shantilal Das, Ravi Mehrotra and Deshdeep Sahdev, (in communication).
- [125] Sujay Datta, Shantilal Das, Ravi Mehrotra and Deshdeep Sahdev, submitted to Phys. Rev. B.
- [126] Ravi Mehrotra, Sujay Datta and Deshdeep Sahdev. (in communication.).
- [127] K. R. Rao and P. Yip, *Discrete Cosine Transforms, Algorithms, Advantages, Applications* (Academic Press, Inc., 1990).
- [128] W. H. Press, S. A. Teukolsky, W. T. Vetterling and B. P. Flannery, *Numerical Recipes* (Cambridge University Press, Cambridge, 1986).
- [129] R. A. Sweet, SIAM J. Numer. Anal. **14**, 706 (1977).
- [130] P. M. Duxbury, P. D. Beale and P. L. Leath, Phys. Rev. Lett. **57**, 1052 (1986).
- [131] P. M. Duxbury, P. L. Leath, and P. D. Beale, Phys. Rev. B **36**, 367 (1987).
- [132] John C. Inkson, *Many-Body Theory of Solids* (Plenum, NY, 1984, Chap. 2.).
- [133] R. M. Merserau, Proc. of the IEEE **67**, 930, 1979.

- [134] I. S. Gradshteyn and I. M. Ryzhik, *Table of Integrals, Series and Products* (Academic Press, Inc., 1965).
- [135] A. Larkin, Y. Ovchinnikov and A. Schmid, *Physica B* **152**, 266 (1988).
- [136] U. Eckern and E. B. Sonin, *Phys. Rev. B* **47**, 505 (1993).
- [137] T. J. Hagenaars, P. H. E. Tiesinga, J. E. van Himbergen and Jorge V. José, *Phys. Rev. B* **50**, 1143 (1994).
- [138] R. Theron, S. E. Korshunov, J. B. Sigmond, Ch. Lemann and P. Martinoli, *Phys. Rev. Lett.* **71**, 1246 (1993).
- [139] S. E. Korshunov, A. Vallat and H. Beck, *Phys. Rev. B* **51**, 3071 (1995).
- [140] W. Y. Shih and D. Stroud, *Phys. Rev. B* **30**, 6774 (1984).
- [141] L. L. Sohn, M. S. Rzchowski, J. U. Free, M. Tinkham and C. J. Lobb, *Phys. Rev. B*, **45**, 3003 (1991).
- [142] P. N. Strenske and S. Doniach, *J. Appl. Phys.* **57**, 867 (1985).
- [143] Shantilal Das, Sujay Datta, Mitrajit Dutta, Shilpa Jain, and Deshdeep Sahdev, *Physica D* **91** 278 (1996); Shantilal Das, Sujay Datta, M. K. Verma, Deshdeep Sahdev and Ravi Mehrotra, *Physica D* **91** 292 (1996) .
- [144] P. A. M. Dirac, *The Principles Of Quantum Mechanics* (Oxford University Press 1958).
- [145] J. J. Sakurai, *Modern Quantum Mechanics* (The Benjamin/Cummings Publishing Company Inc. 1985).
- [146] D. Dudgeon and R. M. Merserau, *Multidimensional Digital Signal Processing*. (Prentice Hall, 1984).

- [147] R. C. Budhani, M. Shenaga and S. H. Liou, Phys. Rev. Lett. **69**, 3816 (1992);
R. C. Budhani, S. H. Liou and Z. X. Cai, Phys. Rev. Lett. **71**, 621 (1993).
- [148] M. S. Rzchowski, S. P. Benz, M. Tinkham and C. J. Lobb, Phys. Rev. **42**, 2041 (1990).
- [149] I. Dhingra, V. N. Moorthy and B. K. Das, Supercond. Sci. Technol. **8**, 252 (1995).
- [150] T. P. Orlando, J. E. Mooij and H. S. J. van der Zant, Phys. Rev. B **43**, 10218 (1991).
- [151] E. Simanek, Sol St. Comm. **48**, 1023 (1983).
- [152] H. S. J. van der Zant, F. C. Fritschy, T. P. Orlando and J. E. Mooij, Phys. Rev. Lett. **66**, 2531 (1991).
- [153] H. S. J. van der Zant, F. C. Fritschy, T. P. Orlando and J. E. Mooij, Phys. Rev. B **47**, 295 (1993).